Downloaded from orbit.dtu.dk on: Dec 16, 2017

Technical University of Denmark

DTU

Semiconductor Mode-Locked Lasers for Optical Communication Systems

Yvind, Kresten; Hvam, Jørn Marcher

Publication date:
2003

Document Version
Publisher's PDF, also known as Version of record

Link back to DTU Orbit

Citation (APA):
Yvind, K., & Hvam, J. M. (2003). Semiconductor Mode-Locked Lasers for Optical Communication Systems.

DTU Library
Technical Information Center of Denmark

General rights
Copyright and moral rights for the publications made accessible in the public portal are retained by the authors and/or other copyright owners and it is a condition of accessing publications that users recognise and abide by the legal requirements associated with these rights.

- Users may download and print one copy of any publication from the public portal for the purpose of private study or research.
- You may not further distribute the material or use it for any profit-making activity or commercial gain
- You may freely distribute the URL identifying the publication in the public portal

If you believe that this document breaches copyright please contact us providing details, and we will remove access to the work immediately and investigate your claim.

Ph.D. Thesis

Semiconductor Mode-Locked Lasers for Optical Communication Systems

Kresten Yvind
Center for Communication, Optics and Materials.
Technical University of Denmark
DK-2800 Lyngby, Denmark

Acknowledgements

Many people have contributed to the work presented in this thesis. First I would like to thank Professor Jørn M. Hvam, Associate Professor Dan Birkedal and Ph.D. Jesper Hanberg (GiGA-Intel) for being supervisors on the work.

A special thanks go to Jesper Hanberg for teaching me the technology of indium phosphide and sharing his many years of experience in the field. - And for making everything a little more fun.

I am especially grateful to Professor Jesper Mørk who, even though he was not a formal supervisor, was probably the one who did most of the advising. He always found time to cheer me up when I had successfully assassinated the last good laser. Also, access to his international network of collaborators has been very important.

Post doc. Peter M. W. Skovgaard, did much of the process development in the tough start of the SCOOP project where nothing worked and his effort during this period should be recognized.

I could thank very many people at the dynamic environments at COM and GiGA, who have given inspiration or practical assistance to the work, but given my bad memory I would surely miss some, so I will not try to mention all.

However, especially technical discussions with Tommy W. Berg, Svend Bischoff, Lotte J. Christiansen, Thorkild Franck (GiGA), Karsten Hoppe (GiGA), Sune Højfeldt, Martin Løbel (GiGA), Josep Mulet, Leif Oxenløwe, Henrik N. Poulsen Bjarne Tromborg and the remaining SCOOP and opto-electronics members have been rewarding and contributed significantly to this thesis.

Also, Casper Angelo, Lotte J. Christiansen, Thomas Jørgensen, David Larsson and Frank Persson did some of the practical work and their assistance has been much appreciated. The users of the systems and network laboratory at COM are thanked for tolerating my frequent and sometimes extensive equipment loans, and the administrative personnel are thanked for solving all the non-technical problems.

I would very much like to thank GiGA,- an Intel company for giving access to processing facilities and sharing of process recipes. Also, GiGA should be accredited for funding the consumables used for the work and for

doing most of the equipment maintenance and repairs.

A crucial step forward in the work was my visit (COST267 Short term mission) to the group of Prof. H.G. Weber at the Heinrich Hertz Institute in Berlin. I would like to thank Marcel Kroh, Reinhold Ludwig, Lothar Küller and Edgar Pawlowski for sharing their extensive knowledge of external cavity lasers and optical coatings. Marcel Kroh is also acknowledged for many subsequent enlightening discussions.

Professor Gadi Eisenstein and his coworkers at Technion, Haifa are thanked for helpful discussions on jitter, coatings and mode-locked lasers.

Professor Hans Melchior from ETH Zurich is acknowledged for giving access to their extensive processing knowledge at the very beginning of the SCOOP project.

Sune Højfeldt is acknowledged for proof-reading most of the thesis and for helpful comments.

This work has been supported in part by the National Technical Research Council programme SCOOP, and the COST267 action.

July 2003,

Kresten Yvind

An electronic (color) version of this thesis is available at:
http://www.Yvind.dk/kresten/Yvind_PhD_dp.pdf

Abstract

This thesis deals with the design and fabrication of semiconductor mode-locked lasers for use in optical communication systems. The properties of pulse sources and characterization methods are described as well as requirements for application in communication systems. Especially, the importance of, and ways to reduce high-frequency jitter is discussed.

The main result of the thesis is a new design of the epitaxial structure that both enables simplified fabrication and improves the properties of monolithic lasers. 40 GHz monolithic lasers with record low jitter and high power is presented as well as the first 10 GHz all-active monolithic laser with both short pulses and low jitter.

Results from external cavity mode-locked lasers are also reported along with an investigation of the influence of the operating conditions on the performance of the device. Antireflection coatings are a critical limiting factor for external cavity devices and a chapter is devoted to calculations on coating design.

The fabrication process for the lasers is outlined and solutions to the challenges encountered in realizing the proposed structures are reported.

Resumé

Denne afhandling omhandler design og fremstilling af halvlederbaserede kortpulslasere til brug i optiske kommunikationssystemer. Egenskaber for pulskilder, samt de tilhørende karakteriseringsmetoder, er beskrevet og relateret til de krav, der stilles for anvendelse i kommunikationssystemer. Specielt er vigtigheden af jitter på en kort tidsskala fremhævet, og måder til at nedbringe denne er anvist.

Det vigtigste resultat af afhandlingen er et nyt design af den epitaksielle lagstruktur, der både tillader en simplificeret fremstillingsmetode og samtidig forbedrer egenskaberne af monolitiske lasere. Målinger på 40 GHz monolitiske lasere med rekordlav jitter og høj udgangseffekt præsenteres sammen med de første 10 GHz monolitiske lasere med kun aktive sektioner, der udsender korte pulser med lav jitter.

Også resultater fra en ekstern kavitets kortpulslaser præsenteres, og afhængigheden af operationsbetingelserne undersøges. Beregninger på design af antirefleksbehandlinger, der er en begrænsende faktor for ydelsen fra ekstern kavitets lasere, er ligeledes medtaget.

Endelig er fabrikationsprocessen skitseret sammen med løsninger på nogle de udfordringer, der opstod i realiseringen af de designede strukturer.

Contents

1 Introduction **1**
- 1.1 Optical communication . . . 1
- 1.2 Applications . . . 3
- 1.3 Optical Time Domain Multiplexing . . . 4
- 1.4 Other pulse sources . . . 8
- 1.5 SCOOP . . . 9
- 1.6 Structure of thesis . . . 10

2 Characteristics of mode-locked lasers **13**
- 2.1 Repetition rate . . . 13
- 2.2 Pulse shape, width and background . . . 15
- 2.3 Wavelength and spectral width . . . 18
- 2.4 Pulse jitter . . . 19
  - 2.4.1 Mathematical description . . . 20
  - 2.4.2 Jitter measurement . . . 23
- 2.5 Power . . . 27
- 2.6 Driving circuitry . . . 27
- 2.7 Stability and reliability . . . 28
- 2.8 Price . . . 28
- 2.9 Discussion . . . 29

3 Mode-locked lasers: Theory and design **31**
- 3.1 Passive mode-locking dynamics . . . 32
- 3.2 Pulse shape . . . 33
- 3.3 Design of active material . . . 36
  - 3.3.1 Gain modulated MLL . . . 37
  - 3.3.2 Absorption modulated MLL . . . 42
- 3.4 Ideal monolithic structure . . . 48
  - 3.4.1 Gain section . . . 50
  - 3.4.2 Absorber section . . . 51

3.4.3 Waveguide 53
3.5 Alternative materials 54
3.6 Summary 55

4 Device fabrication 57
4.1 Wafer growth and processing 57
4.1.1 Growth 57
4.1.2 Processing 62
4.2 Static characterization 66
4.3 RF mounting 68
4.4 Dielectric coatings 70
4.4.1 Practical implementation 72

5 Optical thin film coatings 73
5.1 Anti-Reflection coatings 73
5.1.1 Calculating the mode field 74
5.2 AR coating theoretical examples 75
5.2.1 Normal facet 76
5.2.2 Angled facet 78
5.2.3 Process tolerances 81
5.3 High-Reflection coatings 84
5.3.1 Dielectric coatings 84
5.3.2 Metal coating 84
5.4 Summary 85

6 External cavity mode-locked laser results 87
6.1 Experimental setup 87
6.1.1 Chip length and AR coating 88
6.2 Driving conditions 91
6.2.1 Absorber voltage dependence 91
6.2.2 Gain current dependence 92
6.2.3 Wavelength tuning 93
6.3 10 QW angled 94
6.4 Summary 94

7 Monolithic mode-locked laser results 97
7.1 Results on 40 GHz lasers 98
7.1.1 Hybrid mode-locking 99
7.1.2 Low-noise synthesizer 102
7.2 Results on 10 GHz lasers 105
7.2.1 Hybrid mode-locking 105

7.3 Discussion 109

8 Conclusion and outlook **111**
8.1 Conclusion 111
8.2 Outlook 112
8.2.1 Monolithic lasers 112
8.2.2 External cavity lasers 113
8.2.3 Coatings 113

Bibliography **115**

List of publications **142**

A FSRM theory **147**
A.1 Free space radiation mode theory 147
A.1.1 FSRM derivation 147
A.1.2 Numerical implementation 151

B Modal reflection measurement **153**
B.1 Coating evaluation 153
B.1.1 Coupling coefficients 156
B.2 Measurement example 156

C Material parameters **159**
C.1 Band structure 159
C.1.1 Band lineup 160
C.1.2 Density of states 160
C.2 Refractive index 163

D Abbreviations **165**

Chapter 1

Introduction

1.1 Optical communication

The optical communication industry has experienced a turbulent time with tremendous growth rates during the end of the 1990s and an equally "impressive" fall during the beginning of the 21st century, and is currently suffering from over-capacity and lacking revenues.

Looking beyond the industry aspect, the growth in internet traffic has not seen this crisis and has kept rising. Consumers in Denmark now purchase 2 Mbit/s internet connections, a transmission capacity used only by companies just a few years ago, and there is no indication that the bandwidth requirement will stop there. Behind the web browsers, is the technology which make it all possible and this thesis deals with a component that might become very important in future high-speed all-optical communication networks.

This thesis deals with semiconductor mode-locked lasers for optical communication systems. While a "standard" laser emits a continuous wave (CW) beam, a mode-locked laser instead produces a train of short optical pulses originating from one or more pulses circulating inside the laser cavity. Two types of pulse-generating lasers are explored in this thesis: An external-cavity laser and a single chip (monolithic) laser.

The external cavity mode-locked laser (ECMLL) is shown schematically in Fig. 1.1. The output from a short laser chip is coupled to an external cavity using a lens with a high numerical aperture, and a grating or a mirror is used to provide feedback. The facet facing the cavity must have a very low reflection coefficient to avoid multiple "trailing" pulses being formed. Making a good antireflection (AR) coating is one of the biggest challenges with this type of laser. The advantages of the ECMLL are that

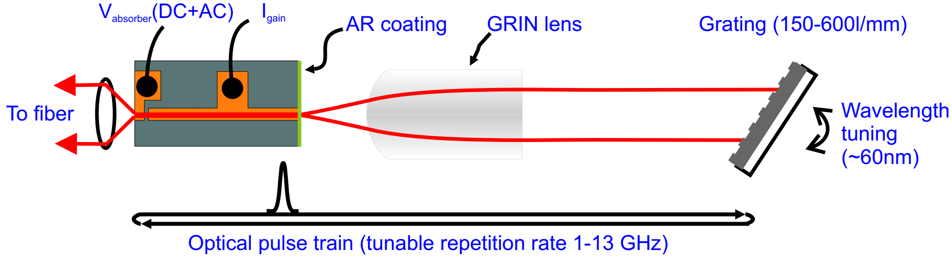

Figure 1.1: Schematic of external cavity mode-locked laser

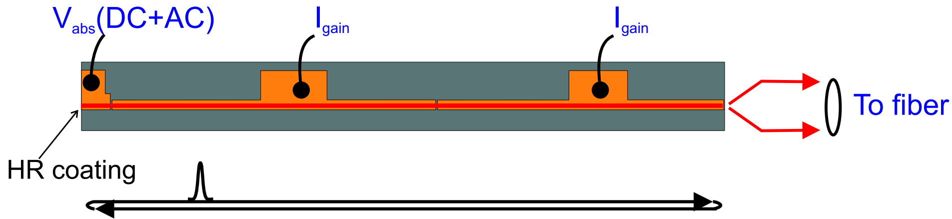

Figure 1.2: Schematic of monolithic mode-locked laser

it is very versatile in that both the repetition rate and the wavelength can be easily tuned using the external elements. The maximum repetition rate is typically a little over 10 GHz due to the size of the bulk optics used. The lower repetition rate can be less than 1 GHz, but if external modulation of part of the laser is used to synchronize the pulse train, much less will not be feasible. For very low repetition rates the modulation becomes much broader than the pulse, and it will lead to poor synchronization.

The monolithic mode-locked laser (MMLL) is a single-chip device, as shown in Fig. 1.2, and is therefore very rugged. But it is more difficult to change the wavelength and repetition rate of the emission. The repetition rate of monolithic lasers is most often quite high ($\geq$40 GHz) since longer active sections "normally" give pulses of poor quality. Lower rates, for instance 10 GHz, are often desirable since the electronic equipment at these rates is cheaper, and they have been achieved by incorporating passive sections in the devices. One of the main results of this thesis is a new design of the active materials in monolithic devices, which makes it possible to avoid the passive section, while still improving the performance for long lasers.

All the devices fabricated have the same epitaxial structure for both gain and absorber section and employ a forward biased gain section and a reverse biased saturable absorber section

1.2 Applications

Communication systems that use pulses are referred to as *return to zero (RZ)* systems, while the alternative is *non-return to zero* (NRZ), where the signal does not go to zero between two consecutive ”ones”. This reduces the bandwidth requirements to the driver electronics, which is why NRZ currently is the most popular modulation format. If the NRZ modulation is applied to a pulse train instead of a continuous wave (CW) beam the requirement to the electronics is unchanged, but an RZ signal is produced.

The RZ modulation format is more tolerant to dispersion and nonlinearities in fibers and is therefore advantageous for high-speed and long-range systems [1].

A short pulse has a wider spectrum and will therefore broaden faster than longer pulses. This can be used in dispersion managed wavelength division multiplexed (WDM) systems, since the peak power will be low and power variations small for almost the whole transmission span. This means that crosstalk between wavelength channels are minimized, and the dispersion compensation can be done neglecting fibre nonlinearities [2]. The drawback is of course a reduced spectral efficiency.

The output from a mode-locked laser (MLL) can also be used as a multi-wavelength source in a WDM system by filtering and modulating the individual modes from the device. Because of the mode-locking process, the mode-partition noise that normally is large in multi-mode lasers, is suppressed [3].

Another application of short optical pulses is the so-called *chirped pulse WDM*, which can be used in the access network to provide low cost routing through WDM demultiplexing. Here, a pulse train with a low repetition rate (the rate to each subscriber) is dispersed such that the different wavelengths are displaced in time, and a high-speed modulator is used to modulate the different wavelength channels [4].

Optical analog-to-digital conversion is another application of short optical pulses that is currently being researched. Short pulses perform the sampling of an optical signal in a non-linear medium [5]. Another type of sampling that requires short pulses is pump-probe measurements where a medium’s response to a optical excitation is probed by another pulse.

Optical signal processing at 10 GHz, 40 GHz and beyond, has been the main driver for our work on mode-locked lasers. At speeds beyond the bandwidth of the electronics, these systems are realized through Optical Time Division Multiplexing (OTDM).

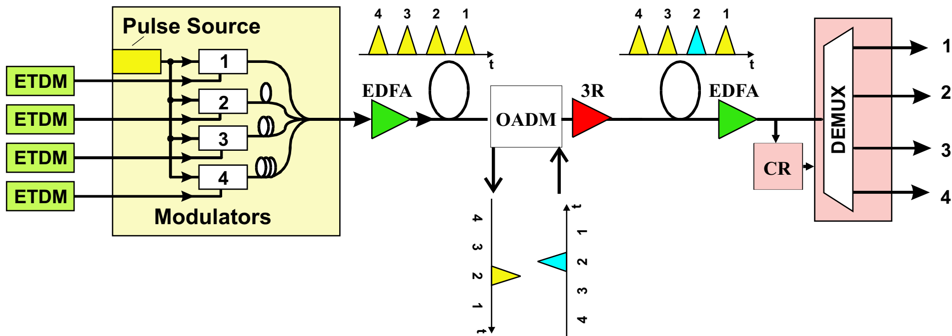

Figure 1.3: Schematic of OTDM transmission system. ETDM: Electrical time-domain multiplexed signal. OADM: Optical add/drop multiplexer. CR: Clock recovery. EDFA: Erbium doped fiber amplifier. 3R: Regenerator performing reamplification, reshaping and retiming. (taken in part from IST optimist 2001 CD-rom)

1.3 Optical Time Domain Multiplexing

As Optical Time Domain Multiplexed (OTDM) systems is important for the work performed, I will give an overview of the functionalities needed for OTDM [6] and other high-speed RZ systems.

A schematic of an ODTM system with a transmitter, a transmission span incorporating add/drop nodes, 3R regenerator and a demultiplexer using clock-recovery is shown in Fig. 1.3. In all of the functionalities mentioned a mode-locked lasers is or can be a vital component, as will be explained in the following.

In the transmitter, a pulse source at repetition rate X GHz is split into N branches that are delayed and modulated before being combined again to form a $N \times X$ Gbit/s signal [7]. The key requirement for the pulse source is sufficiently short pulses (short duty cycle), so they can be interleaved with little overlap. For demonstrator purposes it is customary to simply modulate the baserate pulse train with a single pseudorandom bit sequence (PRBS) and use fiber delay lines to make a high-rate pseudorandom signal. Integrated passive delay lines have been fabricated [8], but in order to keep a pseudorandom signal, the delays have to be certain fractions of PRBS sequence length [9], which can be difficult to accommodate in a planar lightwave circuit. However, a monolithic multiplexer with a splitter, modulators and a combiner has been demonstrated in InP [10], and future versions could include the mode-locked laser, phase adjustment sections, a booster amplifier and perhaps even the power stage of the driving electronics.

Transmitting a high-speed signal is in itself very challenging. Dispersion compensation is required, and for the most demanding applications

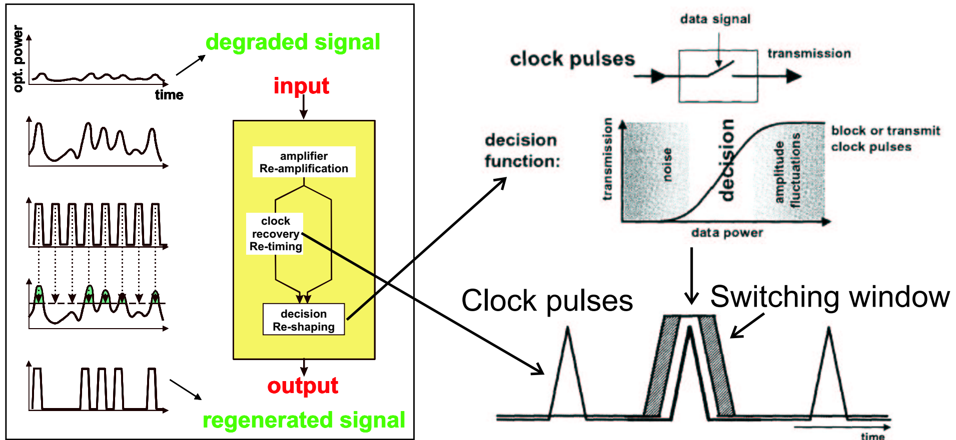

Figure 1.4: Schematic of 3R regenerator. (taken in part from IST optimist 2001 CD-rom, and B. Sartorius' Tutorial at ECOC 2001.)

even adaptive (active) dispersion compensation to correct for temperature variations in the links has to be used. In systems that use bitrates of 160 Gbit/s or higher, also dispersion originating from different propagation velocities of the two polarization modes in the fibers must be corrected for by adaptive schemes.

While multiplexing the signal is quite easy, demultiplexing it is more challenging because both clock and data have to be recovered. One functionality that might be desired is optical add/drop multiplexing, where a single channel can be switched out optically and another added (see Fig. 1.3). This has been accomplished for instance using an optically controlled Mach-Zehnder interferometer [11, 12]. Simultaneous demultiplexing of all channels should be performed at the end nodes. For instance demultiplexing from 160 Gbit/s to eight 20 Gbit/s channels have been performed using four-wave mixing in eight semiconductor optical amplifiers (SOA), hybrid-integrated on a planar light-wave circuit with distribution of signal and control pulses, thereby keeping a tight control of the timing between them [13]. Another way of simultaneously demultiplexing all channels is to wavelength convert the OTDM signal with a dispersed pulse at baserate, thereby making an OTDM-to-WDM conversion [14].

Electroabsorption modulators (EAM) are also frequently used to demultiplex single channels through strong modulation at the baserate, thereby forming a short "switching window". To multiplex all channels the signal has to be split and several EAMs used. The performance of this scheme can be improved using additional cross-gain modulation in an SOA [15].

One of the big problems is routing the traffic. Currently this is done by converting the optical signal at each node to electronic format (o/e conversion) and then use electronic logic to do the routing. Another transmitter (e/o conversion) is used to send the information along the correct path. With many high-rate data-streams this requires a lot of e/o and o/e conversions, which is very cumbersome, and one would like to be able to route the data without converting to electronic format. If the routing is done optically, the signals will be degraded due to losses in the switch fabrics, and regeneration of the signal is needed. Ideally, the signal should be reamplified, reshaped and retimed (3R), and a way of doing this is shown in Fig. 1.4. The "noisy" data signal is transferred, using a gate triggered by the data signal, to a perfect clock that has been derived from the data signal. The clock signal frequency should be at the aggregate rate and could be derived by injection locking a MLL. The gate should have a "switching window" wide enough that timing and amplitude jitter are not transferred from the data signal to the clock signal. Wavelength conversion is also easily performed in this scheme by using a wavelength tunable MLL. For the gates there are many possibilities, for instance an SOA/EA combination, which can be monolithically integrated on InP, have shown a recovery time of 8 ps for -2 V using 1.2 pJ pump pulses [16].

Simpler regenerators performing only reshaping and reamplification (2R) can be made with SOA/EA combinations [17] or interferometric structures, and the requirement to them is a transfer curve which is nonlinear [18–20]. These regenerators could find application in switch fabrics, where they can provide amplification while suppressing accumulated intensity noise. Apart from their simplicity these regenerators also have the advantage that they are close to wavelength transparent in manipulating the original signal. The drawback compared to an amplifier is that each wavelength channel must have its own regenerator, because the regeneration effect depends on the optical power, and crosstalk between WDM channels will reduce the reshaping. Thus, they should be built into WDM routing devices where the wavelengths are demultiplexed by arrayed waveguide gratings [21] or other dispersive structures. Besides regeneration, amplitude-to-timing jitter conversion takes place in a 2R regenerator, and a tradeoff has to be made between the two [18]. However, with many add/drop nodes in the network, a 3R regenerator that corrects acquired jitter, and ensures that all channels have the same wavelength and polarization, will most likely be required.

Clock recovery (CR) can be done in several ways. For low-repetition-rate systems the signal can be detected by a photodiode and the clock re-

covered using an electrical phase locked loop (PLL). This has been demonstrated at 100 Gbit/s [22]. At higher bit-rates the high-frequency electrical mixer can be replaced by an electro-optic mixer, for instance an EAM [23].

A simple way of recovering the clock is to inject the data into a passively mode-locked laser operating at the line rate of the pulse train, which then locks to the signal [24]. This could be used for a 3R regenerator. For demultiplexing a pre-scaled clock (i.e. at a certain fraction of the aggregate clock) should be derived. This has been done by injecting the multiplexed bit stream into a mode-locked laser working at the base rate, for instance 40 Gbit/s→10 GHz conversion [12, 25] and also at higher rates [26].

A problem encountered when simply injecting a high bitrate signal into a mode-locked laser with the desired base rate frequency is phase slips, i.e. shifts of channels when many zeros in the channel used for locking are encountered. This can be avoided by using a two-stage clock recovery, where first the line rate is extracted and then used as input to the base rate CR MLL [27]. If the recovered line rate clock is modulated with the output of the base rate MLL, the stability can be further enhanced and the locking range increased [28].

Injection locked selfpulsating distributed feedback (DFB) lasers have also been used for clock-recovery with a very large locking range [29]. The output of these lasers are nearly sinusoidal and they are therefore difficult to use for subsequent optical signal processing.

Fiber-based mode-locked lasers are generally not used for clock recovery setups due to their small locking range. Schemes using pulse sources that incorporate long lengths of fiber, for instance compression of pulses from gain-switched DFB lasers [30], or beat signals, (see Sec. 1.4), are not usable as the latency introduces instabilities in the locking.

Often pulses from mode-locked lasers are slightly chirped and they can be compressed in standard or dispersion compensating fiber. This is fine for some applications, but for optical signal processing where one would like the mode-locked laser to be monolithically integrated with other components, it is an advantage if the laser itself can produce pulses that are short and un-chirped.

Monitoring the optical signal is also required, and eye diagrams by means of optical sampling is a way to do this [12, 31]. A common approach is to run a mode-locked laser with a frequency displaced some tens of kHz from a recovered base rate clock and monitor the sampled signal at the difference frequency. A 2 ps resolution has been demonstrated in [32] using two ECMLLs. The pulse sources used are often of low repetition rate so that more than one bit period can be monitored, but for eyediagrams same-

frequency lasers can be used.

Finally, it should be noted that OTDM and WDM systems can be combined, and in [33] 19 WDM channels each carrying a 16×10 Gbit/s OTDM signal was demonstrated.

1.4 Other pulse sources

The ECMLL and MMLL investigated in this thesis are not the only options for short pulse generation. Diode-pumped solid state lasers (DPSS) have been developed recently that deliver excellent performance. As an example, actively mode-locked erbium doped fiber lasers have produced the pulses for the current 1.28 Tbit/s OTDM "records" [34, 35]. They use a long dispersion compensated cavity and harmonic mode-locking and are popular due to their short pulses and because they can be assembled from standard components (which can be characterized before assembly). However, they are difficult to stabilize due to the long fiber length and many pulses in the cavity. Another interesting laser built on erbium and ytterbium doped crystals is the optically pumped passive fundamental-mode-locked 10 GHz external cavity laser [36, 37]. The mode-locking mechanism is a semiconductor saturable absorber mirror, i.e. a Bragg mirror with one or more low-temperature grown quantum wells, to achieve fast absorption recovery through non-radiative traps. As this laser is not harmonically mode-locked, there are no problems with missing pulses or "supermode" noise. However, it must be synchronized through continuous mechanical adjustment of the cavity length [38].

Semiconductor vertical external cavity mode-locked lasers have also been demonstrated, both optically [39, 40] and electrically pumped [41], and very recently even sub-picosecond pulses have been obtained with an optically pumped device [42].

The above pulse sources are resonant in the sense that the laser output frequency is related to the round trip time in the laser cavity. For external cavity lasers this is not a big problem because the cavity length can be adjusted. Tuning from 1 GHz to 26 GHz has been shown [43]. By using harmonic mode-locking, 40 GHz pulse trains have been produced using an external cavity laser with a (tunable) fundamental rate around 10 GHz [44]. Monolithic lasers have a more limited tuning range because an induced change of refractive index, cavity length (for fiber lasers) or wavelength (using the cavity dispersion [45]) must be used. By using chirped gratings the tuning range can be extended, but the tuning is accompanied by a wavelength shift, which has to be compensated if frequency and wavelength

tuning are to be independent.

Contrary to the above, many non-resonant schemes exist. These include the selfpulsating DFB lasers [46, 47], compression of beat signal from two lasers [48], compression of pulses from gain-switched DFB lasers [30, 49] or modulation of a CW beam using integrated tandem EAMs [50], EA/DFB combinations [51] or standing-wave EAMs [52]. All these approaches have the advantage that it is relatively easy to change the repetition frequency and wavelength of the emitted pulse train. However, they are typically not very efficient and provide pulses of much poorer quality than do mode-locked lasers.

Comparing the different pulse sources, the solid state based lasers currently deliver the best performance (see also Sec. 3.5), followed by the semiconductor MLLs and finally the non-resonant devices. As the semiconductor MLL can be monolithic integrated it is very likely that if these lasers are ever to be in widespread use for telecommunication the semiconductor MMLL will be the winning option. Integrated tandem EAMs could be used initially, but the technology needed to integrated these with DFB lasers is as advanced as the technology needed to make a monolithic MLL, so one might as well use the superior MLL. Also, the fast and easy synchronization makes the lasers ideal for optical signal processing.

1.5 SCOOP

This Ph.D. project has been financed by the Technical University of Denmark (DTU) and has had a strong interaction with the Danish Technical Research Council funded research program *Semiconductor Components for Optical Signal Processing* (SCOOP). The program was initiated in 1998 with the purpose to start up a collaboration between the optical transmission systems and optoelectronics activities at DTU and the company GiGA (acquired by Intel Corporation in 2000). The idea is to combine the knowledge of theory, technology, components and systems to form a closed loop. Also, a technology transfer from GiGA to process facilities which was supposed to be set up at DTU was anticipated to ensure a continuous flow of candidates from the university to industry. The program is headed by Professor Jørn Hvam, with Professor Jesper Mørk and Jesper Hanberg of GiGA-Intel as daily technical organizers and advisors.

A large effort from all participants was directed at making a 40 Gbit/s electroabsorption modulator for use in a 40 Gbit/s transmitter. This was quite successful and within a year the technology and the understanding of the device were improved, such that the bandwidth of the fabricated EAMs

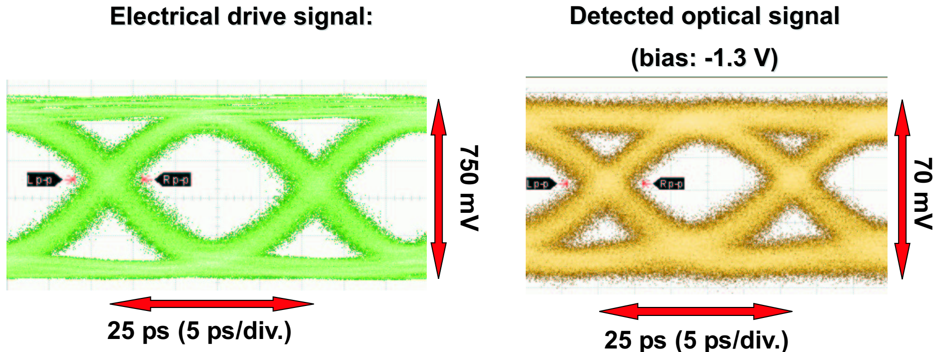

Figure 1.5: The 40 Gbit/s eye diagram to the right was obtained using a SCOOP EAM and the electrical drive signal to the left. (Curtesy GiGA, an Intel company)

was increased from 2 GHz to 35 GHz, which is sufficient for 40 Gbit/s NRZ transmission systems. An eyediagram of the output from a SCOOP EAM is shown in Fig. 1.5 (right) with the electrical signal driving the modulator shown on the left.

Other results using SCOOP components are "error free" wavelength conversion from one to eight wavelengths in a SCOOP EAM at 40 Gbit/s, clock-recovery at 160 Gbit/s using the EAM as electrooptic mixer [23], and 17 dBm saturation output power combined with 20 dB internal gain in a semiconductor optical amplifier.

My contribution to the different projects has been to the optical and electrical design of the semiconductor chips including establishing material parameters. Also, epitaxial growth including calibration and maintenance of the growth machine has been undertaken along with some semiconductor processing, although not much process development. Coating design, fabrication and evaluation have been major tasks, as have mounting and experiments with the mode-locked lasers.

1.6 Structure of thesis

In Chapter 2 the main characteristics of pulse sources are outlined. The requirements and measurement methods are presented. Chapter 3 presents a simple theory of mode-locking and more importantly outlines the correspondence between the design of the active layers of the lasers to the performance of the laser. In Chapter 4 the optimized designs are presented along with some fabrication details and static characterization. Chapter 5 is devoted to results on calculations for thin film coatings. Mode-locking

results for external cavity and monolithic lasers are presented in Chapters 6 and 7, and Chapter 8 concludes the work and provide suggestions for further efforts.

In addition, appendices have been included for the coating theory (Appendix A), coating evaluation (Appendix B) and material parameters (Appendix C).

Chapter 2

Characteristics of mode-locked lasers

In this chapter I shall look at the characteristics of the emitted pulse-train from the point of view of a potential user and mostly treat the mode-locked laser as a black box. The lasers fabricated as part of this project are aimed at the telecommunications sector. Thus, the requirements related to this application will be the prime concern, but the scope will be broadened when applicable. Knowledge of the requirements for the lasers will motivate the design discussions presented in the following chapter.

Seen from the point of view of a potential user, a number of the following characteristics might be important and need to be specified: 1. Repetition rate, 2. Pulse shape, width and background, 3. Wavelength and spectral width, 4. Pulse jitter, 5. Power, 6. Driving circuitry, 7. Stability and reliability, 8. Price.

These items will be elaborated on in the rest of the chapter. For some of the non-trivial measurements the measurements methods will also be discussed.

2.1 Repetition rate

The minimum repetition rate of a mode-locked laser is determined by the round-trip time in the cavity. If a linear cavity is used, such that the pulse travels back and forth between two mirrors, the round-trip time will be two times the cavity length (L) times the group refractive index of the materials (n_g) divided by the velocity of light (c), and the repetition rate will be the

Rep. rate	Period	Distance in air	... in InGaAsP ($n_g \approx 3.6$)
1 GHz	1 ns	30 cm	83 mm
10 GHz	100 ps	3 cm	8.3 mm
40 GHz	25 ps	7.5 mm	2.08 mm
160 GHz	6.25 ps	1.9 mm	0.52 mm
1 THz	1 ps	0.3 mm	0.083 mm

Table 2.1: Approximate correspondence between repetition rate and the spatial distance between pulses. The corresponding linear cavities should have the shown lengths divided by 2

reciprocal of that,

$$f_{rep} = \frac{c}{2n_g L} \tag{2.1}$$

A few examples of the correspondence between repetition rate and distance between pulses are shown in Table 2.1. If n pulses are circulating, the repetition rate is n times the fundamental repetition rate (harmonic mode-locking).

For telecom transmission, the repetition rate is fixed at certain frequencies set by industry standards for multiplexed data. As an example the SDH standard specifies frequencies of: 9.95328 GHz ±20 *ppm* or 39.813120 GHz ±20 *ppm*[53]. The laser should at least be able to reach one of these frequencies, but some tunability might be desired for instance for error correction codes. The overhead from forward error correction varies but a laser covering 39.813120 GHz to 42.656914 GHz would include most current standards [54]. This is a tough requirement for monolithic lasers, but a smaller tuning range will probably be acceptable as error correction codes are consistently improved.

The laser and the electronics providing data for the pulse train must be synchronized. For a transmitter this can be achieved by using an electrical clock to modulate the pulse train in the laser. Some lasers do not have an internal modulator but are tunable by means of a voltage (or current) signal, thereby forming an optical voltage-controlled oscillator (VCO). The control could be through cavity length adjustments using piezos [55] or refractive index control for semiconductor lasers [56–58], the latter with the advantage of a very fast response time (>100 MHz). These lasers can then be synchronized using an external phase locked loop to feedback this voltage [59]. If the laser is sufficiently stable, the electronics can be synchronized by sending part of the pulse-train to a photodiode and use the electrical output as a clock.

2.2 Pulse shape, width and background

The requirements to the pulse shape, width and background depend a lot on the application. For optical signal processing where the pulse is used to control an optical switch, a short pulse might be the only requirement with little emphasis on the shape and background. However, if the pulse-source is to be used for transmission purposes in OTDM systems, strict requirements are imposed on the pulse quality .

For Gaussian pulses with no background, calculations show that a power penalty[1] less than 1 dB can be achieved if the pulse full width at half maximum (FWHM) is less than half the available time-slot, i.e. 3.13 ps, 1.57 ps and 0.781 ps for 160 Gbit/s, 320 Gbit/s and 640 Gbit/s transmission systems [60]. The power penalty due to a finite background depends on the number of channels multiplexed. Thus, for the same extinction ratio 4×40 GHz performs better than 16 × 10 GHz. The pulse extinction ratio required for 1 dB penalty with pulse widths half the time-slot is 29, 35 and 37 dB for 160, 320 and 640 Gbit/s, respectively.

Hyperbolic secant pulses have more extended tails than gaussian pulses. The requirement to the maximum pulse-width is therefore more severe, while the background requirements should be expected to be the same.

Pulses in the picosecond range are difficult to measure using a conventional photodiode and sampling oscilloscope, as this would require a measurement bandwidth of several 100 GHz, which is not available today. Measuring pulse width is therefore almost exclusively done using nonlinear autocorrelation techniques. An autocorrelation measurement is fundamentally different from the direct measurement in that it involves the interaction of the pulse with a delayed replica of itself. The pulse is thus characterized indirectly as a function of this delay which can be controlled very accurately, for instance 0.1 ps resolution corresponds to a spatial accuracy of $\sim$15 μm. The extremely high resolution combined with low price make the autocorrelator the preferred tool for short-pulse characterization. That it does not require a trigger extends it's applicability to free-running systems. However, since it is based on a nonlinear process it requires high power and for the crystal-based version, it requires a linearly polarized beam. The high power is in practice achieved by amplification in an erbium doped fiber amplifier (EDFA) or SOA while the polarization is adjusted using a polarization controller or polarization maintaining fibers.

A schematic setup for autocorrelation measurements is shown in Fig. 2.1.

[1] The extra power needed at the receiver to achieve a given error probability (typically 10^{-9}) compared to the "optimum" situation

The pulse to be characterized is split in two parts and sent into arms, one of which has an adjustable delay (τ). The beams are combined using a lens which focuses on a properly angled second-harmonic generating (SHG) crystal, for instance $LiIO_3$, KTP or BBO. The autocorrelator shown is so-called background free since the individual beams do not contribute to the detector signal. This is because the second harmonic of each beam will have the same direction as the original beam and it will therefore be spatially filtered as shown in Fig. 2.1. Only the second harmonic having contribution from both beams will hit the detector determined by k-conservation (phase-matching) in the anisotropic crystal.

Most often the delay is introduced by placing a retro-reflector on a "shaker" (similar to a loudspeaker assembly), thus achieving scan frequencies of up to several tens of Hertz. Due to the angle between the beams and the thickness of the crystal any coherent (phase) contribution will be washed out and the recorded signal is therefore referred to as intensity autocorrelation (see Eq. (2.2)) in contrast to interferometric autocorrelation. As the detector (typically a photo-multiplier tube, PMT) records intensity, the measured background-free autocorrelation functional has the form [61]:

$$f_{zb}(\tau) = \frac{\int I(t)I(t-\tau)dt}{\int I(t)^2 dt} \tag{2.2}$$

In order to increase the sensitivity of the measurement, lock-in techniques or photon counting can be used. Also, low-pass filters are used before the crystal to remove residual EDFA pump etc. and a high-pass filter can be used between the crystal and detector to remove unconverted light as shown in the figure.

Instead of the SHG/PMT combination two-photon absorption (TPA) in a photodiode can be used. The signal will not be background free but the method has been shown to be very sensitive. Examples of this approach include a 1.3 μm laser diode [62], a silicon avalanche photodiode (APD) [63], and a Si APD combined with photon counting [64]. Sensitivity, which for autocorrelators is expressed as average power times peak power, as low as $1.5 \cdot 10^{-4}(\text{mW})^2$ has been demonstrated, but the dynamic range is quite low due to single photon absorption [62]. This is a general problem for the TPA based autocorrelators [65] and the maximum dynamic range is around 20dB for the Si based versions, which also have a poorer efficiency [66]. However, a high sensitivity of $1.7 \cdot 10^{-4}(\text{mW})^2$ combined with a high dynamic range have recently been demonstrated using TPA directly in a GaAs photon counting PMT [66]. Thus, this method can characterize very weak pulses, but is still not good for measuring pulse to background ratios, as it is not background free.

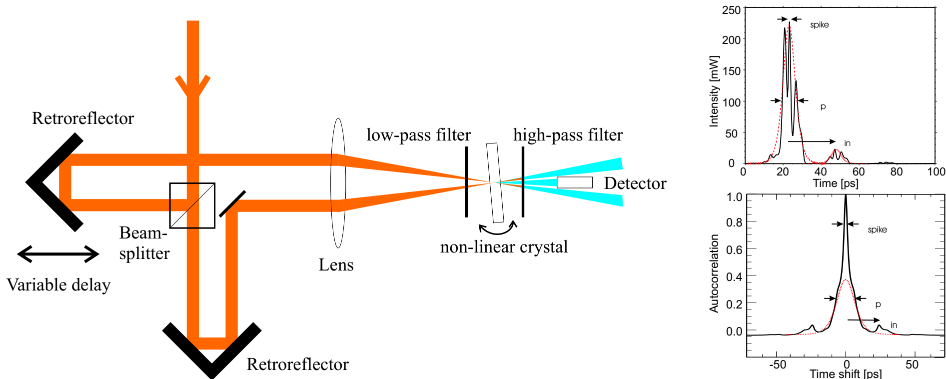

Figure 2.1: *Left*: Schematic of background free autocorrelation measurement based on second harmonic generation *Right* Top: Noisy pulse with trailing pulse. Bottom: Autocorrelation of the noisy pulse showing a coherence peak ([67])

Pulse shape	I(t)	$\Delta\tau$	$f_{zb}(\tau)$	$\Delta\tau/\Delta\tau_c$	$\Delta\tau\Delta\nu$
Gaussian	e^{-t^2}	1.665	$e^{-\tau^2/2}$	0.7071	0.4413
Hyperbolic secant	$\mathrm{sech}^2(t)$	1.763	$\frac{(\tau\coth(\tau)-1)}{\sinh^2(\tau)}$	0.6482	0.3148

Table 2.2: Important parameters for commonly used fitting functions. I(t): Intensity profile. $\Delta\tau$ FWHM: Full width at half maximum for I(t). $f_{zb}(\tau)$: Background free autocorrelations function. $\Delta\tau/\Delta\tau_c$: Ratio of pulse FWHM to autocorrelation FWHM ($\Delta\tau_c$). $\Delta\tau\Delta\nu$: Time bandwidth product ($\Delta\nu$ spectral width (in Hz)). From [61]

The commercial *APE Pulsecheck* crystal-based autocorrelator that was used for the measurements in the current work is specified to have a sensitivity of < 100 (mW)^2, but for reasonable clean traces (dynamic range of $\sim$20 dB after subtraction of noise) a practical sensitivity of 4000(mW)^2 is found.

The autocorrelation function, Eq. (2.2), is by definition a symmetrical function regardless of the symmetry properties of the original pulse. Shown in Table 2.2 is the autocorrelation functions f_{zb} for two of the functions commonly used to estimate the actual pulse-shape from the autocorrelation trace. Column 5 shows what factor the measured FWHM of the autocorrelation trace ($\Delta\tau_c$) should be multiplied by to obtain the actual pulse FWHM ($\Delta\tau$). In experimental literature the sech^2 and Gaussian are the most commonly used fitting functions even though modelling have predicted non-symmetric pulse-shapes [68].

Besides masking pulse asymmetries autocorrelation measurements show other peculiarities when the measured pulses are not "well-behaved". Semiconductor mode-locked lasers show complicated dynamics on timescales

below 1 ps and they can emit many closely spaced subpicosecond pulses within a broader envelope. Such "finite bursts of noise" will give rise to a so-called coherence peak on top of a pedestal, the width of which is related to the width of the envelope of the "noise", see Fig. 2.1 (right). For real noise the ratio between the peak and pedestal is 1:2 for background free autocorrelation [69] and the coherence peak should be neglected when fitting is used to estimate the total width of the emitted (noise) pulse. Also, poor AR coatings on external cavity mode-locked lasers can give rise to incomplete mode-locking, which creates a coherence peak.

Other pulse-shapes than the ones shown in Table 2.2 have been used in literature e.g. a *Lorentzian* and the "shortest" pulses reported have had this shape. The Lorenzian or *double exponential* autocorrelation shape is however most likely a signature of time-varying pulseshapes [70] or a coherence peak which is indistinguishable from the pulse similar to the example in Fig. 2.1. When the Lorentzian function fits well, my experience is that a sech^2 with a coherence peak with ratio 1:2 fits equally well and it provides a better interpretation of the usability of the actual pulse train.

2.3 Wavelength and spectral width

For telecom applications the wavelength range 1530–1565nm is the most commonly used due to the low loss in silica fiber and the possibility for amplification using EDFAs. Systems at 1.3 μm are also used for transmission spans where amplification is not needed and the low dispersion at 1.3 μm eliminate the need for dispersion compensation. Semiconductor based mode-locked lasers in the $\text{In}_{1-x}\text{Ga}_x\text{As}_y\text{P}_{1-y}/\text{InP}$ material system can be tailored to any wavelength in this range. A more serious requirement is that of wavelength tunability. Tunability is easily achieved in external cavity devices but is more difficult to achieve in monolithic devices where refractive index changes or band-gap temperature tuning must be used. Only a limited refractive index change is possible through current injection and for an optimized structure a maximum tuning range of 15 nm has been achieved [71], corresponding to a refractive index change in the integrated Bragg grating of $\Delta n \sim 0.03$. In order to have a larger tuning range a mechanism based on refractive index differences can be used, an example being the grating assisted directional coupler [72, 73], which also provides broad filtering bandwidth.

The spectral width of the emission is important for transmission purposes. A short pulse will have a minimum spectral width given by the Fourier relation between the optical spectrum and the temporal autocorre-

lation function [74]. A number of examples for the time-bandwidth product using FWHM values for different pulse shapes are shown in Table 2.2. The transform limit is achieved when the mean wavelength is unchanged during the pulse and it is then said to be unchirped. Quite often the time-bandwidth product is larger than the transform limit, meaning that the instantaneous emission wavelength changes across the pulse. If the optical frequency increases with time this is called up-chirp [75] or blue-chirp and the pulse can be compressed using standard single mode fiber (SMF), which has anomalous dispersion at 1.55 μm. Similarly, the term down-chirp or red-chirp is used when the frequency decreases with time and the pulse can then be compressed in dispersion compensating fiber (DCF), which has normal dispersion at 1.55 μm.

A simple measurement of the autocorrelation and the optical spectrum does not provide any information of the nature of the chirp. Different lengths of fiber can be inserted before the autocorrelator to give an idea of the magnitude and sign of the linear chirp, but this is a quite tedious measurement and it only gives information on the linear part of the chirp. More advanced methods can be used and one of the most successful is Frequency Resolved Optical Gating (FROG) [76, 77], in which the second harmonic signal from the autocorrelation measurement is spectrally resolved and a numerical algorithm is used to extract the pulse amplitude and phase information. A number of implementations exist and the method has been applied to for instance pulses from a 40 GHz MMLL [78] and a 160 GHz compressed beat signal [48].

The FROG technique requires a lot of power as it employs a non-linear process. A linear approach has been commercialized by APEX. Their technique is to measure both amplitude and phase of the optical spectrum through the use of an optical mixing technique and then perform a Fourier transformation. Since this method is linear it should be expected to be quite sensitive, but the measurement time is similar to an optimized commercial FROG (i.e. < 1 min), and it only works at certain repetition rates due the built-in electronics. For simple pulse characterization, FROG is therefore the better and cheaper solution, but for for data-modulated signals the APEX system could be useful.

2.4 Pulse jitter

Currently, one of the most important research topics on mode-locked lasers is the jitter of the emitted pulses, i.e. the deviation from a perfect train of identical pulses. Figure 2.2 shows a pulse-train and one can imagine some

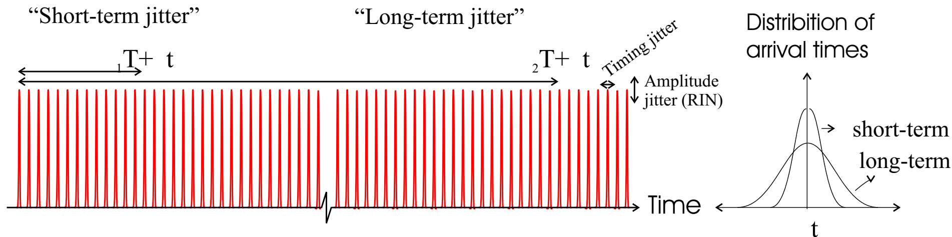

Figure 2.2: Schematic of noisy pulse train. The timing jitter, i.e. distribution of arrival times is shown in the graph to the right for two different timescales

variation in pulse amplitude and arrival times as also shown in a sampling oscilloscope trace in Fig. 2.3 (left). I shall limit the discussion to timing and amplitude jitter, but a more rigorous treatment would also include optical frequency (i.e. wavelength) and phase jitter [79, 80]. Frequency jitter will translate into timing jitter after long transmission spans, but dispersion compensation will counteract this effect. Phase jitter is related to the phase of the electrical field "inside" the pulse envelope and will probably only matter for metrology applications.

The amplitude jitter is the variation from the average pulse energy, while the timing jitter is the deviation from the arrival time expected for a pulse in a perfect pulse train. The jitter can, to some extent, be viewed as more important than e.g. the pulse-width, power etc. in that these quantities can be altered through "passive" schemes outside the laser cavity. As an example the pulse shape and width can be altered through the use of a non-linear loop mirror [81], although one of course would prefer to be able to use the output of the source directly.

It is possible to reduce the timing jitter of an emitted pulse-train by synchronous modulation of either amplitude or phase but this translates the timing jitter into amplitude or wavelength jitter[82]. Amplitude jitter can be reduced externally using a device with a nonlinear transfer function e.g. a non-linear optical loop mirror [83].

2.4.1 Mathematical description

In order to quantify the jitter we need to define it in a mathematical sense. The intensity of a perfect pulse train can be written as

$$F_0(t) = \sum_{\mu=-\infty}^{\infty} f(t + \mu T) \tag{2.3}$$

where T is the reciprocal of the repetition rate, μ is an integer and $f(t)$ is the pulse shape. If a small amount of noise is added to the pulse train the output can be written as

$$\mathrm{F}\left(\mathrm{t}\right)=\left(1+A(t)\right)F_{0}\left(t+J\left(t\right)\right) \tag{2.4}$$

where $A(t)$ is a random function that describes the deviation in pulse amplitude from the average amplitude and $J(t)$ is a random function that describes the deviation in arrival time from the repetition time T.

The root mean square (RMS) timing jitter (σ_J) can be written as:

$$\left(\sigma_J\right)^2=\left\langle J^2\right\rangle \tag{2.5}$$

while the RMS amplitude jitter (ΔE) (or relative intensity noise, RIN: $\frac{\Delta E}{E}$) is:

$$\left(\frac{\Delta E}{E}\right)^2=\left\langle A^2\right\rangle \tag{2.6}$$

The averages ($\langle\rangle$) in Eqs. (2.5) and (2.6) should in principle be taken over all times but in practice this is not feasible and, more important, this does not give the physically important value for communication purposes. The jitter will depend on the time span used for the measurement as shown in Fig. 2.3 (right) for the timing jitter. The relevant time span depends on the application. If the pulse source is used in a sampling system and is supposed to be a clock source that shows the sampled signal on an absolute timescale, then the long-term timing jitter is important on the timescale of the total trace persistence time. However, if the laser is to be used as a transmitter in a communication system where clock-recovery (CR) is performed in the receiver, then the jitter on a very long timescale will not matter as this will be trivially tracked by the clock-recovery circuit.

The power spectral density [84] of F, S_F to second order in $\mu\frac{2\pi}{T}\sigma_J$ is [59, 85]

$$S_F\left(\omega\right)\propto\left|\tilde{f}\left(\omega\right)\right|^2\sum_{\mu}\left(\begin{array}{l}\left(1-\left(\mu\frac{2\pi}{T}\right)^2\sigma_J^2\right)2\pi\delta\left(\omega-\mu\frac{2\pi}{T}\right)\\+\left(1-\left(\mu\frac{2\pi}{T}\right)^2\sigma_J^2\right)S_A\left(\omega-\mu\frac{2\pi}{T}\right)\\+\left(\mu\frac{2\pi}{T}\right)^2S_J\left(\omega-\mu\frac{2\pi}{T}\right)\end{array}\right) \tag{2.7}$$

where $\tilde{f}\left(\omega\right)$ is the Fourier transform of $f(t)$ and S_A (S_J) is the power spectral densities of A(t) (J(t)). The power spectrum is thus composed of delta-functions at the repetition rate and higher harmonics thereof, with an envelope function given by the fourier transform of the pulse, i.e. shorter

pulses produce more harmonics. Around each of there harmonics noise skirts from amplitude and timing jitter are present.

The RMS timing jitter can be obtained by integrating the power spectral density of J [59, 84]:

$$\sigma_{J,\infty} \equiv \sqrt{\langle J(t)^2 \rangle} = \sqrt{\frac{1}{\pi}\int_0^{\infty} S_J(\omega) d\omega} \tag{2.8}$$

In order to take the fact that we do not want to average J(t) over all times into account we define the jitter in a certain frequency range as:

$$\sigma_J = \sqrt{\frac{1}{\pi}\int_{\omega_{low}}^{\omega_{high}} S_J(\omega) d\omega} \tag{2.9}$$

The average of the rolling finite time averages in Eqns. (2.5) and (2.6) can be mapped into spectral filtering in the frequency domain by choosing ω_{low} and ω_{high} properly.

Following the discussion above, the integration should therefore be divided into different ranges relating to the performance of electrical clock recovery (CR) circuits. These frequency ranges have been standardized by the International Telecommunication Union in the G.8251 recommendation [53] and have been reproduced in Table 2.3. Starting with the ranges 1 and 2, they relate directly to the locking bandwidth of the CR circuit. At low frequencies (range 0) it is trivial for the CR to track the signal and the jitter in this region can therefore be neglected. The last region (range 3) is beyond the locking bandwidth of the CR and will therefore directly give rise to bit errors in the received signal. The actual requirements are not very strict, but if the signal is multiplexed to higher bit-rates, the requirements increase. In [86] a jitter requirement for Bit Error Rate (BER) 10^{-9} (10^{-12}) of less than $\frac{1}{12}$ ($\frac{1}{14.1}$) bit-period is quoted which translates into 0.52 (0.44) ps for 160 Gbit/s and 0.13 (0.11) ps for 640 Gbit/s. The jitter requirements quoted here are for the demultiplexing process, i.e. after the clock recovery and hence the jitter requirements are for the high-offset (short-term) range. For a data modulated signal, modulation sidebands on the carrier will exist, so even if it is possible to widen the locking range of the clock recovery, this will not be desirable, and the jitter in the signal must be low at high offsets.

If the pulse source is multiplexed to a higher bit-rate using passive multiplexing then the jitter from longer timescales corresponding to the difference in path lengths will be transferred to the pulse to pulse time scale. For a real multiplexer with a number of modulators and only fractional bit delays this will of course not be the case.

Line rate	Range 0	Range 1	Range 2	Range 3
10GHz	$< 20k$	20k–80M	4M–80M	80M–5G
40GHz	$< 20k$	20k–320M	16M–320M	320M–20G

Table 2.3: ITU-T jitter generation standard measuring filters[53]. All ranges in Hz

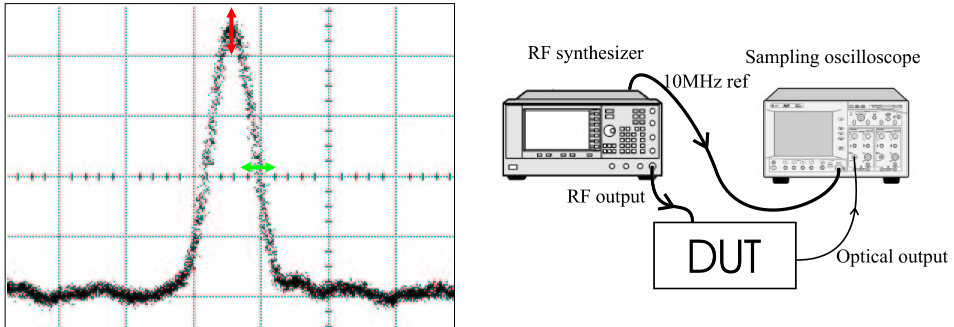

Figure 2.3: *Left*: Sampling oscilloscope trace of pulse train showing amplitude jitter (vertical) and timing jitter (horizontal). *Right*: Setup for jitter measurement using sampling oscilloscope

2.4.2 Jitter measurement

As mentioned above one would like to measure the jitter filtered in the ranges 1–3 of Table 2.3. There are a number of ways used to measure pulse jitter. In the following I will discuss the sampling oscilloscope, phase noise measurements and pulse cross-correlation measurements and outline the strengths and weaknesses of each.

Sampling oscilloscope

A simple way of measuring jitter is to use a sampling oscilloscope as shown on the trace in Fig. 2.3 (left) and simply make statistics on the acquired trace. Most high-speed oscilloscopes cannot trigger on the data stream itself and need a external trigger or (subharmonic) clock recovery. For each trigger event, the oscilloscope samples one point at a certain delay after the trigger and this delay is then swept through the displayed range to acquire the full trace. This triggering process has for most oscilloscopes a jitter in the picosecond range thus this will overshadow the jitter from the device under test. For pulse source characterization the trigger is normally provided by a 10 MHz reference from the electrical synthesizer driving the laser as shown in Fig. 2.3 (right). If the path-length of the trigger signal

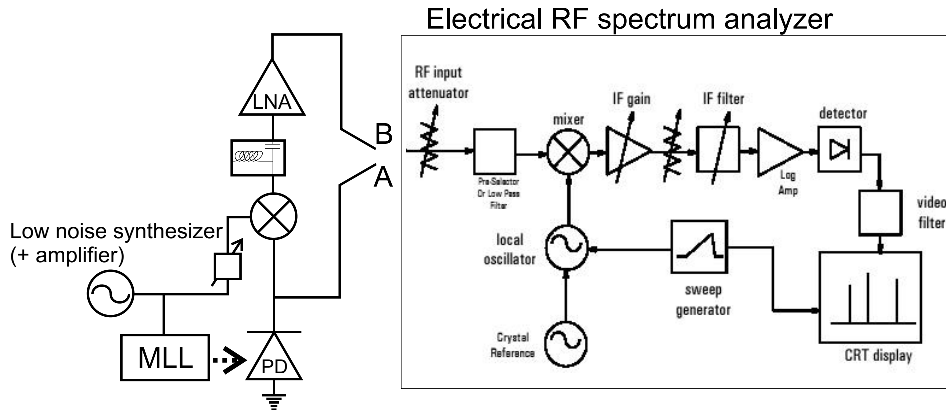

Figure 2.4: Setup for measuring phase noise using an RF spectrum analyzer. *A* path: Original method [59, 85]. *B* path: High dynamic range measurement [87–89]. PD: Photo-diode, $\Delta\tau$: Electrical time delay, LNA: Low noise amplifier

and the length of the path driving the laser is similar, this will constitute a relative measurement and the long-term jitter of the synthesizer will not show up in the measurement. This could be usable as a rough estimate due to the simplicity of the measurement if it wasn't for the high trigger jitter. Recently (2001) however, Agilent Technologies has released a *high-stability timebase* module which permits jitter as low as 200 fs to be measured on the oscilloscope, thereby making this a feasible solution.

Phase noise measurement

The most popular method of measuring jitter is in the frequency domain where the noise skirts on the repetition frequency of the pulse-source can be used to calculate the timing jitter. The method was first presented by D. von der Linde[85] and in it's original form uses an electrical RF spectrum analyzer (ESA) to directly measure the signal from a high-speed photodiode as shown in Fig. 2.4 (Path A).

Ideally we would like to measure S_F from Eq. (2.7) using the spectrum analyzer. A spectrum analyzer, however is calibrated to measure narrow-band signals and this introduces errors when broadband noise is the signal. A correction of +2 dB has to be added to the measured signal to account for conversion of Gaussian to Rayleigh-distributed noise due to the peak-responding voltmeter, logarithmic amplification and shape of the resolution bandwidth filter [90]. For the peaks corresponding to the harmonics and for spurious peaks, however, this correction, should not be applied.

From the corrected measurement we can now define the *Single-sideband*

phase noise spectral density $L(f)$ as the ratio of the measured phase noise in a 1 Hz integration bandwidth ($P_n(f)|_{1Hz}$) to the total carrier power P_c at an offset f from the carrier frequency:

$$L(f) = \frac{P_n(f)|_{1Hz}}{P_c} \tag{2.10}$$

When the measured noise signal has been corrected for the measurement errors, the noise in 1 Hz bandwidth is simply the measured noise-signal divided by the used resolution bandwidth. $L(f)$ is normally quoted in the units dBc (1Hz), where the "c" means relative to the carrier. It is independent of the measurement apparatus so it is a convenient parameter to use for comparison of different sources.

Assuming that the amplitude noise is low the jitter can be calculated from

$$\sigma_J = \frac{T}{2\pi}\sqrt{\int_{-f_{high}}^{-f_{low}} L_{lsb}(f)df + \int_{f_{low}}^{f_{high}} L_{usb}(f)df} \tag{2.11}$$

where the use of the average of the upper and lower sidebands (usb, lsb) reduces the sensitivity to the amplitude noise [87]. In the above, we have assumed that the fundamental harmonic is used for the evaluation, but as seen from the μ^2 pre-factor to S_J in Eq. (2.7) evaluating the phase noise at different harmonics can be used to separate amplitude and phase noise. From Eq. (2.11) we see that the jitter squared is proportional to the area under the phase noise curve. This also means that if we want to add jitter contributions from different integration ranges, these should be added as squares.

One significant problem encountered when trying the use the simple (path A in Fig. 2.4) method to evaluate jitter at high offsets from the carrier is that the noise floor of the spectrum analyzer is reached. The mixers in the spectrum analyzers can only tolerate a limited amount of power before the output saturates. As an example, the HP8565E 50 GHz spectrum analyzer used in Chap. 7 has a maximum mixer level of -10 dBm and the displayed noise floor (1 Hz) is -130 dBm– (-140 dBm) at 40 GHz, so the dynamic range is only 120– 130 dBc.

In order to increase the dynamic range one can use the setup shown as path B in Fig. 2.4 [88, 89]. By adjusting the time delay ($\Delta\tau$) such that the pulse train and the reference from the synthesizer is exactly out of phase (in quadrature) only timing jitter is measured. Furthermore, through the homodyne measurement the carrier is removed, so that one can amplify the remaining noise and send it into the spectrum analyzer with a sufficient power to overcome the noise figure of the ESA. A thorough review of this

method and improvements is presented in [87]. The "B" measurement implemented as shown here of course measures the jitter relative to the synthesizer, but for high offsets the jitter of the generator is very low and the jitter is intrinsic to the laser, so this is not a problem.

The amplitude jitter can be measured at baseband since timing jitter does not contribute here as seen from Eq. (2.7) with μ=0, but careful receiver design using low noise preamplifiers has to be used to ensure enough dynamic range to measure the RIN [87].

One big advantage of the phase noise measurements is that the frequency distribution of the noise is mapped out, so that it is possible to get a hint to what the noise source is, e.g. relaxation oscillations of the laser or RF pickup in the measurement.

Pulse cross correlations

A simple and almost direct method of measuring high frequency jitter is to measure the cross-correlation between two pulses with a time difference T_d and determine the broadening compared to the autocorrelation [91]. This could be done by making one of the arms in the autocorrelator (Fig. 2.1) much longer than the other.

The pulse to pulse timing variance between two pulse trains delayed by the time T_d is a weighted integral of the timing jitter spectral density[59]

$$\left\langle \left(J\left(t+T_d\right)-J\left(t\right)\right)^2\right\rangle = \frac{2}{\pi}\int_0^\infty S_J\left(\omega\right)\left(1-\cos\left(\omega T_d\right)\right)d\omega \tag{2.12}$$

Thus, in practice the frequency range over which the jitter is evaluated is approximately $\frac{1}{4T_d}$ to ∞[91] due to the (1-cos) term. If one wants to measure the jitter in the range 320MHz to ∞, the extra delay should be a little less than 1 m, which would be possible to do using free-space optics. Longer delays are possible using fiber delay lines, but then the dispersion introduced has to be taken into account through a third measurement of the autocorrelation of the dispersed pulse [80].

If the pulses and noise are Gaussian the pulse to pulse jitter is simply

$$\sigma_{pp} = \sqrt{\sigma_{xc}^2 - \sigma_{ac}^2} \tag{2.13}$$

where σ_{xx} are the variances of the cross-correlation (xc), autocorrelation (ac) and pulse to pulse jitter (pp). For general pulse shapes the deconvolution has to be done numerically. The jitter in Eq. (2.13) is the pulse to pulse jitter. To compare with the pulse to clock jitter, which is measured by the other methods, the relation $\sigma_{pc} = \sigma_{pp}/\sqrt{2}$ can be used when the

delay is large enough, such that the pulse to clock jitter of the two pulses are uncorrelated. For small jitter values the autocorrelation measurements has to be done very carefully as small errors multiply when the two widths are subtracted.

Another problem with the method is that the jitter measurement is insensitive to jitter at timescales of multiples of 1/T due to correlations in the measurement corresponding to the periodic cosine filtering in Eq. (2.12). The noise features at large offsets from the carrier are quite broad with the relaxation-oscillation peak being the most narrow important feature of typically >100 MHz width. For long delays corresponding to 10 MHz or less offset from the carrier, the features would be included but for free-space measurements, where the maximum delay is a few metres, the filtering might affect the accuracy of the measurement.

The cross correlation can also be done mixing the time scales of the pulses using a free-space Michelson [92] or fiber Mach-Zehnder [93] interferometer before an ordinary autocorrelator. This way only one measurement needs to be done but the more complicated trace might make it more error-prone.

In summary, the low-frequency jitter in the ranges 1&2 of Table 2.3 can be measured accurately using standard SSB measurements while the very high frequency jitter (range 3) should be measured either using the high-dynamic range phase noise measurement or using pulse cross-correlations.

2.5 Power

High output power (>10mW) and good efficiency is always desirable, for transmission systems to overcome losses in multiplexers, modulators etc., and for signal processing to deliver enough power for the nonlinear process utilized. The issue is not too critical as good amplifiers exist, so pulse-shape and jitter is more critical.

2.6 Driving circuitry

The driving circuitry should preferably be as simple as possible and semiconductor mode-locked lasers generally satisfy this with only some DC currents and voltages and RF synchronization of one section. This should be compared with the extensive control equipment needed for fiber lasers and external cavity DPSS. However, for monolithic lasers, tunable in both repetition rate and wavelength, the control might be quite complicated as all the controls will be interrelated. For widely tunable CW lasers, some success

has been achieved in characterizing the lasers beforehand and saving the settings in embedded control software allowing the user to control the laser with digital commands. The characterization time and stability of this approach has been under recent investigation and these issues could be even more difficult with mode-locked lasers due to the additional requirement of controllable repetition rate.

Tunable external-cavity devices could be designed with fairly simple control circuitry as the different properties can be tuned more independently.

2.7 Stability and reliability

Both CW DFB lasers, external-cavity tunable lasers and electroabsorption modulators have been qualified for use in optical lightwave systems. Thus, mode-locked semiconductor lasers should also be expected to pass such reliability tests. Monolithic semiconductor devices are known to be very stable and reliable when burn-in procedures have been undertaken, but they are quite temperature dependent and Peltier control will probably be necessary.

The requirement for wavelength stability will be a fraction ($\frac{1}{10}$) of the channel spacing and it will therefore be relaxed on an absolute scale compared to dense WDM, where very narrow channel spacing of e.g. 25 GHz has been used. For 160 Gbit/s systems a channel spacing of 400 GHz, equivalent to 3.2 nm, has been demonstrated [94]. In any case, feedback using an external wavelength locker can be used to ensure long-term stability. Also, a photodiode and TPA detector could be combined with the device to have closed-loop control of the device.

2.8 Price

- is always important.

Monolithic lasers will ultimately have the lowest price as they can be produced using semiconductor batch processing and packaging similar to DFB lasers. Currently however, external cavity lasers are the only ones to achieve wide tunability of repetition rate and wavelength with short transform limited pulses. Thus, they will have a relevance similar to the current market sharing between DFB and CW tunable external cavity devices.

Fiber lasers and DPSS lasers will not be able to compete on the price and will be used for ultra-high performance applications where price is of

less importance. Sampling systems might benefit from passively mode-locked fiber lasers where the low repetition rate and short and powerful pulses will be ideal.

A further advantage of the (monolithic) semiconductor lasers is the possibility of integration with modulator(s) [95], multiplexors, 3R regenerator, etc. As packaging constitutes most of the cost for the final component, this will be the ultimate advantage for semiconductor devices when the process yield is high enough to make it feasible. Optoelectronic integration is also possible[96], thereby placing the electrical power amplifier on the InP chip such that simple SiGe electronics can drive the laser ”directly”. Initially, however, co-packaging of discrete chips will be a cheaper solution.

2.9 Discussion

Few if any mode-locked lasers are currently employed in actual optical networks and cheap, versatile, compact and reliable devices will have to be developed further in order for this to happen. Semiconductor mode-locked lasers are the strongest contender to achieve the requirements discussed in this chapter.

Mode-locked and Q-switched lasers are currently used for industrial application, where they are used to deliver a large peak power. They are not semiconductor lasers but large YAG lasers or fiber based solutions. The repetition rates used are low to increase the pulse energy for a given average power and (monolithic) semiconductor lasers are thus less likely to replace the solid state solutions for these applications.

On the other hand, the emergence of affordable picosecond pulse-sources might bring some of the techniques currently only used in research laboratories, e.g. pump probe measurements, into more widespread use.

Chapter 3

Mode-locked lasers: Theory and design

In this chapter we will first outline the basic theory behind mode-locking and then discuss the design of the epitaxial material to obtain short, unchirped low-jitter pulses. It turns out that the properties of the gain medium is very important for the laser and a novel approach to it's design is described.

One distinguishes between two kinds of mode-locking, i.e. active and passive from the pulse-shaping mechanism. For active mode-locking a strong modulation is applied to a short length of the cavity and it is the time-varying (net) gain which locks the longitudinal modes together and forms the pulse. One the other hand a passive mode-locked laser can oscillate without external modulation and it is through the introduction of a saturable absorber, which "favors" pulses (see below), that the laser emission is shaped into a circulating pulse. A passive mode-locked laser can be synchronized to an external clock by modulating a section of the device, this is called hybrid mode-locking. If the pulse shape does not change much, the pulse-shaping mechanism is still passive mode-locking and the dynamics could be described as the synchronization of a passive mode-locked laser to the external modulation. On the other hand, for the 10 GHz monolithic devices in Sec. 7.2.1 significant pulse narrowing is seen when modulating the passive mode-locked laser and the pulse-shaping mechanism is therefore a combination of active and passive mode-locking.

The basic pulse-forming mechanism in active mode-locking is fairly simple, with the modulation forming a window in time of net gain such that the pulse is actively shaped each time is passes through the modulation section as shown in the top of Fig. 3.1 [97]. A slightly more accurate de-

scription would include the depletion of carriers by the pulse resulting in a shorter gain window [98]. Active mode-locking can also be loss modulation, where the gain is driven with a constant current and the loss is periodically lowered to achieve net gain synchronized with the pulse round-trip time.

Passive mode-locking on the other hand relies on a dynamic interplay between the absorber and gain section which will be outlined in the next section.

The early (usable) theories of mode-locking were mainly formulated for dye laser systems by *New* [99] and *Haus* [100–102]. Shortly thereafter the theory was extended to include semiconductor systems [98, 103–105], initially based on external cavity setups as this was the experimentally available system.

For a general description of the mode-locking process an excellent presentation is found in *Siegman* [106].

3.1 Passive mode-locking dynamics

The lasers studied here are mainly passively mode-locked and we will therefore take a closer look at the pulse-forming dynamics taking place in such lasers. In the middle figure in Fig. 3.1 the dynamics of the loss and gain integrated over a round trip in a time frame relative to the pulse is shown. This corresponds to the lumped element theory of Haus in the slow absorber case. Starting with the loss curve, we see that there is a large loss before the pulse. The leading edge of the pulse is absorbed and the carriers created lower the loss until a certain point, where the number of carriers absorbed is lower than the number of carries removed by e.g. sweep out, and the loss recovers. Similarly for the gain we see a saturation and a recovery, but the saturation is not as strong and the recovery is slower than that for the loss such that a ”window” of net gain is formed, when pulses circulate in the cavity. The stronger saturation and faster recovery of the absorber compared to the gain element is a requirement for passive mode-locking.

One of the important differences between active and passive mode-locking is that the pulse shaping in active mode-locking becomes less efficient for short pulses, while the absorber in passive mode-locking keeps shortening the pulse even for very short pulses. Passive mode-locking is therefore generally producing shorter pulses than active mode-locking. If the transit time through the absorber is shorter than the pulse and it is placed next to a high reflector the pulse returning from the mirror sees an already bleached absorber and this *self colliding pulse mode-locking* (SCPM) is quite often used to help ensure that the absorber saturates more easily

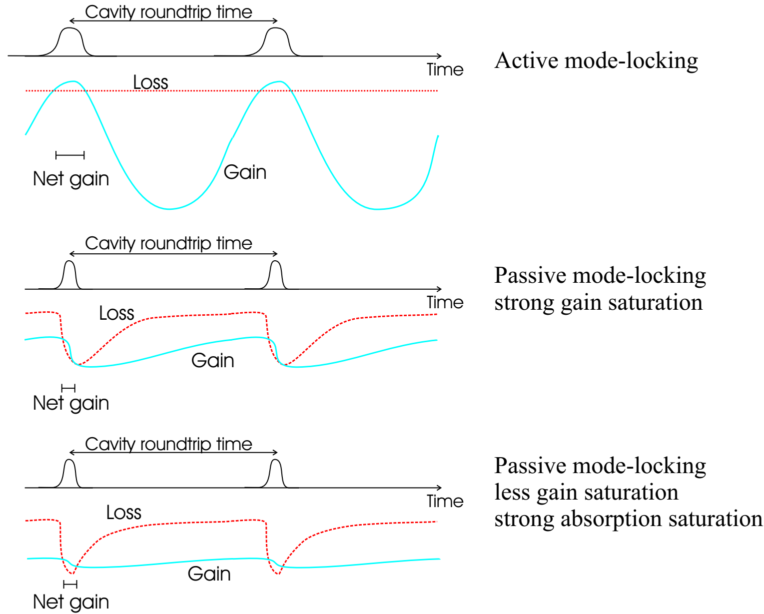

Figure 3.1: Schematic of gain and loss dynamics for active and passive mode-locking

than the gain.

3.2 Pulse shape

The schematics in Fig. 3.1 explain why pulses are formed but not which width and shape they achieve and how the optical spectrum looks.

Several effects are responsible for pulse broadening:

- *Spectral filtering* due to finite gain bandwidth or grating structure.

  For a transform limited pulse the product of the spectral width and pulse width is constant, thus bandwidth limiting elements broaden the pulse.

- *Dispersion* in materials and from gratings.

  Depending on the sign of the dispersion, with respect to the sign of the pulse chirp, it can broaden or narrow the pulse.

- *Gain saturation*

  Due to gain saturation the leading part of the pulse experiences more gain than the peak, thereby effectively increasing the pulse width.

This also gives rise to spectral broadening due to self-phase modulation (SPM) i.e. index changes induced by the pulse[107]. SPM in combination with dispersion and saturable absorption are responsible for the chirp of the pulse (see e.g. [108]).

The mechanisms shortening the pulse are limited to

- *Saturable absorption* that absorbs the leading edge of the pulse and through it's fast recovery closes the gain window.
- *Active modulation*

It is thus the interplay between these effects that determine the output of the lasers. When the pulse widths inside the laser chip are larger than $\sim$1 ps the gain and absorption dynamics is related to total carrier densities. For high powers, finite transport times from the doped layers [109], finite capture times [110, 111] etc. can become important but these can be included as gain suppression factors, increased loss, reduced quantum efficiency etc. and are important, but they do no change the qualitative behavior significantly.

When the pulse width inside the laser becomes less than 1 ps the ultrafast carrier dynamics comes into play. The effects described above can, to a large extent, be related to the movement of carriers in real space. The "ultrafast" effects on the other hand arise from dynamic changes in the energetic distribution of the carrier, i.e. in momentum space as explained in the following.

In the gain section the carriers with the "correct" transition energy are consumed for the gain and a spectral hole is "burned" (SHB) in the carrier distribution. This hole will be filled from the rest of the carrier distribution through carrier-carrier scattering with a time constant on the order of 100 fs. The carriers removed will generally be of less energy than the average energy of the population and the carrier distribution will therefore be of a higher temperature than before the pulse. Thus, the distribution will relax towards the crystal temperature through carrier-phonon scattering with a time constant around a ps [112, 113]. The high temperature carrier distribution will spread over a larger energy range thus the inversion will be reduced until the carrier cooling process is completed. The result of this fast dynamics is increased gain suppression, but sometimes also multiple closely spaced pulses as there is ample gain just after the first pulse has passed. This is not desirable and should be avoided.

For the absorber a similar fast dynamics takes place leading to a reduction of the saturation energy. The dynamics depends on whether bulk or

quantum wells are used since for the former the high externally applied electric field heats the carriers and therefore inhibits their thermalization[114, 115].

In order to avoid the fast effects spectral filtering can be used to ensure that the pulses are always a few ps, but if very short pulses are needed, ways of reducing the problem has to be devised either by stretching the pulse before it enters the amplifier and compress it afterwards or to find ways of controlling especially the gain dynamics.

The pulse widths produced in the present project are typically a few picoseconds, and accordingly ultrafast dynamics effects except for the CW implications, are not of much concern. Making stable subpicosecond mode-locked lasers is however one of the big challenges in the field and it is therefore still interesting to find ways to reduce or take advantage of these effects.

Many papers have been published on the important subject of the dynamics of mode-locked lasers. Simple semi-analytical theories like those of Haus give insight on the stability ranges and basic material requirements for continuous pulse emission. They also explain the basic dependence on gain bandwidth, self-phase modulation, dispersion etc.[116, 117] and provide a good starting point for work with mode-locked lasers. Through perturbation theory the semi-analytical approach have also been applied to describe the noise [79, 80]. More involved numerical simulations with elaborate models of the semiconductor material have been undertaken, including spatial effects [118], ultrafast carrier dynamics [68, 119, 120], noise and realistic gain models [121]. These models can simulate a given laser quite well and give detailed information on pulse shape, both magnitude and phase, and more important the pulse-shaping mechanisms. Unfortunately, the exercise of mapping the results of the simulations, which are often in the form of material saturation energies, escape times etc., onto the layer structure of the laser is seldom attempted, thus the result of the simulations end up mostly as guidelines on how to operate the lasers and not how to design new and better devices in a language easily understandable by crystal growers. Predicting the behavior of a laser from the epitaxial structure is not an easy task but, as will be shown in the experimental part, gross simplification as will be used in the rest of this chapter can still provide new insight and better lasers.

3.3 Design of active material

The goal of the design is to provide short transform limited pulses with a low high-frequency jitter. The jitter on a long timescale ($< 100\ kHz$ offset, see e.g. [122, 123] and measurements in Chap. 7) is almost purely dependent on the driving oscillator and ways of reduce the power required to minimize this part of the jitter have been researched by several groups. Resonant matching of the electrical transmission line to the modulation section is an efficient way of reducing the power required for the synchronization [124]. Here, I shall concentrate on the high-frequency jitter, which is the intrinsic jitter of the device and, when the device is locked to the oscillator, the most important for practical applications as explained in Sec. 2.4. This part of the jitter originates from spontaneous emission and carrier noise and it can be reduced by increasing the inversion of the gain medium, lowering the gain per round trip, increasing the pulse energy or increasing the quantum efficiency [1][80, 125]. Using wider pulses with a more narrow spectrum such that less noise is within the bandwidth is also a way of lowering the jitter but we will aim at achieving low jitter, while keeping short pulses.

The main pulse broadening occurs in the gain section due to gain saturation[68] and this broadening could be counteracted using strong pulse shaping in the absorber section such that the laser still emits short pulses. Besides excess chirping due to self-phase modulation this also introduces excess loss compared to a cavity where less pulse shaping is done and the gain therefore also has to be increased. This leads to an increased spontaneous emission level which in turn results in more jitter. An important design criteria for the mode-locked laser is therefore to achieve a low loss *in the mode-locking situation*.

From the discussion above we can infer that mode-locking should be a gentle process, i.e. ideally the pulse should circulate in the cavity with only little pulse shaping per round trip. Also, the circulating pulse should be strong such that added spontaneous emission photons do not affect the pulse much.

In Fig. 3.1 (middle) the gain saturation was used to ensure that there was no gain after the pulse but, as shown in the bottom figure, it is also possible to produce short pulses with low gain saturation, if the absorbers saturates strongly and recovers fast.

Low-jitter design of mode-locked lasers can be likened to the design of narrow linewidth single wavelength lasers [126]. For the latter we know

[1]Referencing to [79, 80]: The two first terms reduce D_q that is the driving term for all the noise sources. The third term lowers D_θ, D_p and D_t while the last term lowers the carrier shot noise

that a low threshold and high power output make the coherent stimulated emission dominate the noisy spontaneous emission, thereby giving a narrow linewidth. The linewidth narrows with output power until a certain point around 10 mW where it starts to rebroaden due to current noise and/or other effects [127].

In order to discuss the design of active material it is necessary to divide the discussion into devices where either gain modulation or absorption modulation is used to synchronize the device. For the devices studied gain modulation is only used for the external cavity devices, while absorption modulation is used for monolithic devices for reasons that will be described below.

3.3.1 Gain modulated MLL

Gain modulated external cavity devices with implanted absorbers have shown excellent performance [128] but have proven very difficult to fabricate due to stringent requirements to the absorber and antireflection coating. The high performance encourages work on this type of device and for the present work reverse biased saturable absorbers have been used, due to their expected easier manufacturability.

So what are the advantages of using a gain modulated laser? Normally a very strong RF modulation (1 W) is used so there is only a high carrier density during the pulse. Between the pulses the carrier density is lower, which means that the spontaneous emission noise is reduced and the noise is lowered. Also, a passive mode-locked laser normally has upchirp due to gain saturation when the pulse passes through the SOA. A directly modulated laser on the other hand shows downchirp as the carrier density is increased during the pass of the pulse [129]. The combination of the two can therefore be expected to provide pulses that are less chirped.

The laser chip design for a gain-modulated device is similar to a standard high-speed laser structure. A high modulation efficiency requires a high differential gain of the medium, which can be achieved using a (strained) bulk region or a multiquantum well (MQW) structure. We use compressive strained MQW as more strain can be incorporated in the well compared to that of bulk by using strain compensating barriers. High strain and quantum confinement splits the heavy- and light-hole bands such that fewer injected carriers are "wasted" in states, which do not contribute to the gain of interest. This then also lowers the spontaneous emission noise as already shown by the low linewidth of strained DFB lasers [130]. Also, the lower in-plane heavy hole mass reduces the density of states towards that of the conduction band such that a more symmetric inversion is achieved,

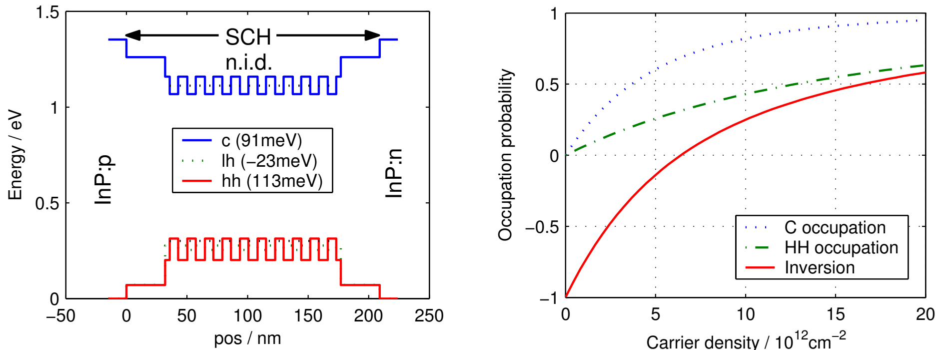

Figure 3.2: *Left*: "As-grown" band diagram for 10 QW laser structure. The number in the parenthesis is the depth of the wells and the horizontal dashed lines show the position of the lowest quantum confined state (calculated for a single quantum well). SCH: Separate confinement heterostructure. n.i.d: not intentionally doped. *Right*: Occupation probabilities (fermifunctions at band edge) and inversion as function of carrier sheet density

which also leads to a lower transparancy current density and a larger differential gain. Quantum wells ideally also provide a more step-like density of states which increases the differential gain when operated with the fermilevels close to the band edge [131]. However, for a fast MQW structure the wells are often placed close together to aid carrier transport by electron tunnelling [109] and this well-to-well coupling smears out the density of states, making the difference between MQW and bulk smaller.

An example of an actual 10 QW structure is shown in Fig. 3.2 (left). The bands are shown with flat bands and no carrier induced band bending and we will refer to this picture as "as-grown" band diagrams. This simple presentation is of course not physically true but it will be sufficient for the discussion to follow. The material system we use in practice is InGaAsP on InP thus all the designs will be made using these alloys. The precise compositions used can be found in Chap. 4 and the material parameters are collected in appendix C.

For the discussions in this chapter I will assume that the device lases at the band edge c-hh transition and a simple relation between the modal TE gain and the inversion of the medium can be used [132]

$$g = \Gamma g_{max} \cdot (f_e + f_h - 1) \tag{3.1}$$

where f_e (f_h) is the Fermi occupation probability for the electrons (holes) at the band edge. The factor $(f_e + f_h - 1)$ represents the inversion of the medium. Γ is the confinement factor, which we will assume is proportional

to the number of quantum wells (N_w) and g_{max} is the maximum gain from one well, taking into account the density of states (in-plane masses), matrix elements (polarization properties) and electron/hole envelope functions overlap integral (selection rules). All the structures investigated in this section have the same quantum well composition and thickness so g_{max} is approximately the same for all of them. Normalizing by g_{max} we can therefore say that the 10 QW structure has a maximum gain of 10 while a 1 QW structure has a maximum gain of 1.

In Fig. 3.2 (right) the occupation probabilities and inversion are shown as function of injected carrier (sheet) density, i.e. the 3D density integrated over the dimension shown in the left figure, with the assumption of an equal number of electrons and holes. We obtain the usual result of higher occupation at the conduction band edge compared to the valence band due to the mass difference. From the inversion curve we find a transparency current density of $n_{tr} = 6.40 \cdot 10^{12} cm^{-2}$ corresponding to zero material gain.

Looking closer to the distribution of carriers an example is shown in Fig. 3.3 for an injected carrier density of $n_{tot} = 8.96 \cdot 10^{12} cm^{-2}$. For the sake of simplicity, parabolic bands are used for the density of states (DOS) and no valence band mixing is included. The quantum confined states are calculated for isolated wells and the single well DOS is simply multiplied with the number of wells, thereby neglecting the coupling between wells. Also, homogeneous broadening due to a finite lifetime of the electronic states which would smear out the strong peaks are not included. For further explanations of the approximations and material parameters, please refer to appendix C. In the top right corner of the figure the values of some interesting parameters are given: The transparency current (n_{tr}) and the carrier density used in the figure (n_{tot}). Next the splitting of the quasifermi levels is calculated to be 24 meV above the bandgap. The proximity of the fermilevel splitting to the bandedge, which is assumed is identical to the transition energy, ensures a large differential gain due to the fact that the slope of the fermifunctions is maximum at the quasi-fermi energies. Next, the gain coefficient is calculated to be 1.9 times the maximum one-well gain and I have assumed that this is the required gain for lasing in this device. The gain (in dB) is proportional to the section length, but in order to be able to make a significant modulation of the gain a short device has to be used (150–350μm) such that the gain coefficient has to be large. The use of many quantum wells then ensures that the high gain can be achieved with the fermilevels close to the band edge.

A comprehensive analysis of the design of the density of states for fast

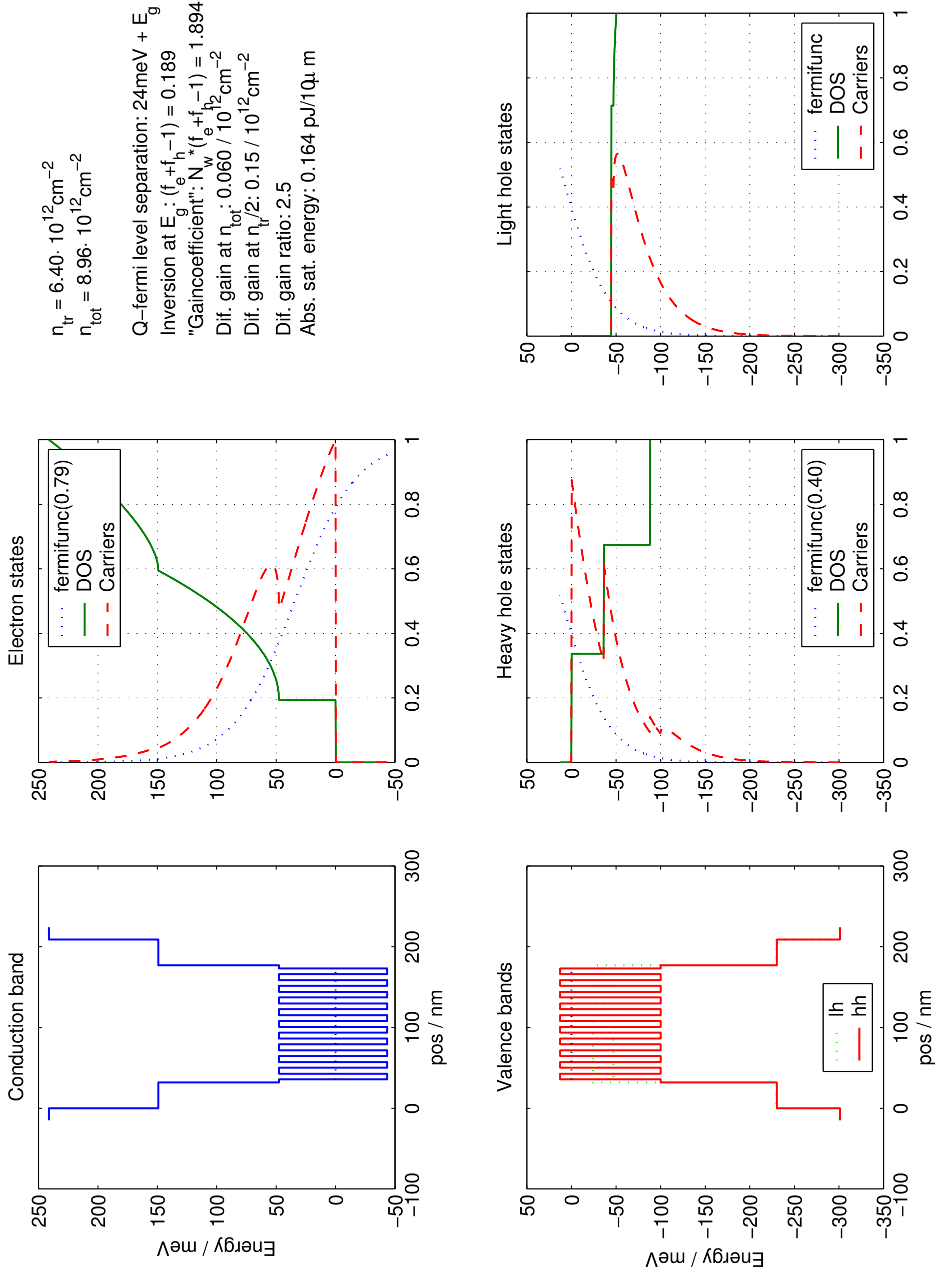

Figure 3.3: 10 QW "fast" laser structure. *Left:* Conduction and valence band schematic. *Center/right:* Density of states (DOS), quasi fermifunctions and carrier density for an injected carrier density n_{tot} as shown in the upper right corner

lasers can be found in [131].

The transport of carriers across the (undoped) separate confinement heterostructure (SCH) can be a critical limiting factor for high-speed lasers [109] and it should be held below approximately 50 nm. This means that the optical mode field penetrates significantly into the surrounding cladding layers with increased free carrier loss as result. In the present work a ridge waveguide structure is used, but for fast lasers a buried heterostructure is often preferred to ensure low parasitics, i.e. leakage currents and capacitances. The large overlap of the mode with the doped regions gives a large waveguide loss in the range of $20 - 30cm^{-1}$. However, the gain section is normally short such that this doesn't matter.

For fast lasers p-doping of the active layers is sometimes used to lower the transparency current [133]. This has not been used for mode-locked lasers, where the same material also is used for the absorber, since it would also lower the field in the absorber and thereby increase the recovery time.

The saturation properties of a semiconductor gain medium is often quantified by the pulse *saturation energy* above which the gain significantly lowered. The saturation energy is defined as [107]

$$E_{sat} = \frac{h\nu A}{\Gamma \frac{dg}{dN}} \tag{3.2}$$

where $h\nu$ is the photon energy, A is the mode area and $\Gamma \frac{dg}{dN}$ is the modal differential gain. The saturation energy is inversely proportional to the differential gain, since carriers are consumed when a pulse is amplified and the gain is therefore lowered proportional to the differential gain. The differential gain is one of the quantities shown in the top-right part of Fig. 3.3, but for the active gain modulated laser this quantity does not provide much information since many carriers are injected while the pulse passes the gain section.

For the absorber a saturation energy can be defined analogous to Eq. (3.2) evaluated for a current density below transparency. I have chosen to calculate the differential gain at half the transparency carrier density, but the gain curve is almost linear in this range, and the exact carrier density does therefore not matter much. In classic mode-locking literature the ratio between the saturation energies in the gain and absorber section is an important parameter and this value is also calculated in Fig. 3.3 (it is equivalent to the ratio of differential gain). This value should be large to ensure that the loss saturates stronger than the gain.

However, for the absorber a different definition might be better, since it is desirable to have a low "on-state" loss in order not to introduce excess

loss in the mode-locking situation as noted earlier. We might therefore consider how many photons that need to be absorbed to saturate the absorber section fully. If we assume that any external field is completely screened at transparency and the carriers are in thermal equilibrium, the energy that should be absorbed is simply proportional to the transparency current density:

$$E_{sat,abs} = n_{tr}^{2D} \cdot h\nu \cdot \text{absorber area} \tag{3.3}$$

This value is calculated in Fig. 3.3 to be 0.16 pJ for a 2 μm ridge and a 10 μm long absorber. This is a quite high value given the fact that an ECMLL normally emit pulses of energy 0.1 pJ or less at 10 GHz and consequently a very large fraction of the pulse is absorbed at each pass. Reverse biased absorbers shorter than 10 μm are extremely difficult to produce as cleaving is used to define the length. In contrast, the implanted absorber is very short ($< 2\mu$m [134]) and it is therefore better in this respect.

The absorber recovers from the saturation during the pulse pass with a recovery time down to below 10 ps [135]. This means that the amount of carriers needed for saturation is higher than estimated above. On the other hand, if the absorption is low and the absorber is short it might not be "possible" to absorb all the carriers corresponding to $E_{sat,abs}$ and the loss is lower than the value quoted.

As will be evident from the discussion in the next section, one way of reducing the problem of too high absorber loss would be to use fewer quantum wells as the transparency current would be less and the gain saturation energy higher. The drawback is a lower modulation efficiency and possibly broader pulses. Another possibility could be to p-dope the wells, if reduced field in the absorber is acceptable, as this would reduce the absorber saturation energy through the reduced transparency current.

3.3.2 Absorption modulated MLL

For the absorption modulated MLL the function of the gain section reduces into amplifying the pulse without broadening it too much. Remembering that a high power will help minimize the jitter this corresponds to a requirement of a large saturation energy of the gain section. From Eq. (3.2) it is seen that this corresponds to a low differential gain, which is exactly the opposite of what was the goal for the gain modulated laser. The design idea for the absorption modulated laser is therefore to a large extent based on reversing the design rules for high-speed lasers. The designs that will be presented are mostly directed at the monolithic lasers which have a long active region, but also external cavity lasers could have an advantage of using a long gain section, see Sec. 6.1.1.

Looking at the inversion curve of Fig. 3.2 we see that the differential gain increases if the gain coefficient is lowered. Given that the gain in a laser to a first approximation is given by the total cavity loss, this means that if the gain section is made longer the saturation energy of the medium will be lower and more pulse broadening and SPM will be the result. One the other hand if the gain section is made very short the required gain coefficient will be large and the quantum wells will be saturated such that the differential gain is lowered. For monolithic lasers the length of the laser is fixed so this means that regrowth or other processing technology must be used to make a short gain section. For 10 GHz monolithic lasers a short gain section has been the approach of all previous work [123, 136–142] except [143], where >6 ps pulses were obtained.

We have chosen a simpler way of achieving a large gain saturation energy by simply using fewer quantum wells. This lowers the differential modal gain by lowering the confinement factor, but equally important the quantum wells become more inverted, since fewer wells have to deliver the same gain, and the differential gain is therefore significantly lowered. A 3 QW example is shown in Fig. 3.4 Since fast gain modulation is not required, fast carrier transport from the doped layer is not an issue and very wide un-doped separate confinement layers can be used. This *large optical cavity* (LOC) design has successfully been used for high-power CW lasers [144–147] as it lowers the loss due to the lower overlap between the optical mode and the doped region, and increases the saturation energy due to the low confinement factor. I use it for the same reasons; low loss is important since the active section is very long and it can therefore contribute significantly to the total cavity loss. As mentioned in the discussion above about jitter the increased loss increases the threshold and therefore also the ASE noise, so the loss is a crucial parameter.

The maximum width of the SCH in the present design is determined by the horizontal mode design. An etch stop layer is used 40 nm above the SCH to create a more gentle transition to the low-index material and thereby a better looking mode, see also Sec. 4.1. If the SCH is made thicker than 500 nm the mode will spread out horizontally and not be confined under the ridge. The optical mode will therefore still penetrate into the lossy p-doped layers and graded p-doping can be used to lower the loss as shown in Fig. 3.5 using layer thicknesses and doping densities from Chap. 4. The shown calculation is scalar 1D and it underestimates the penetration of the mode into the doped layers compared to a full 2D calculation.

Carriers in the SCH layers contribute to the loss and, since they will not available for scattering into the quantum wells due to the fact that

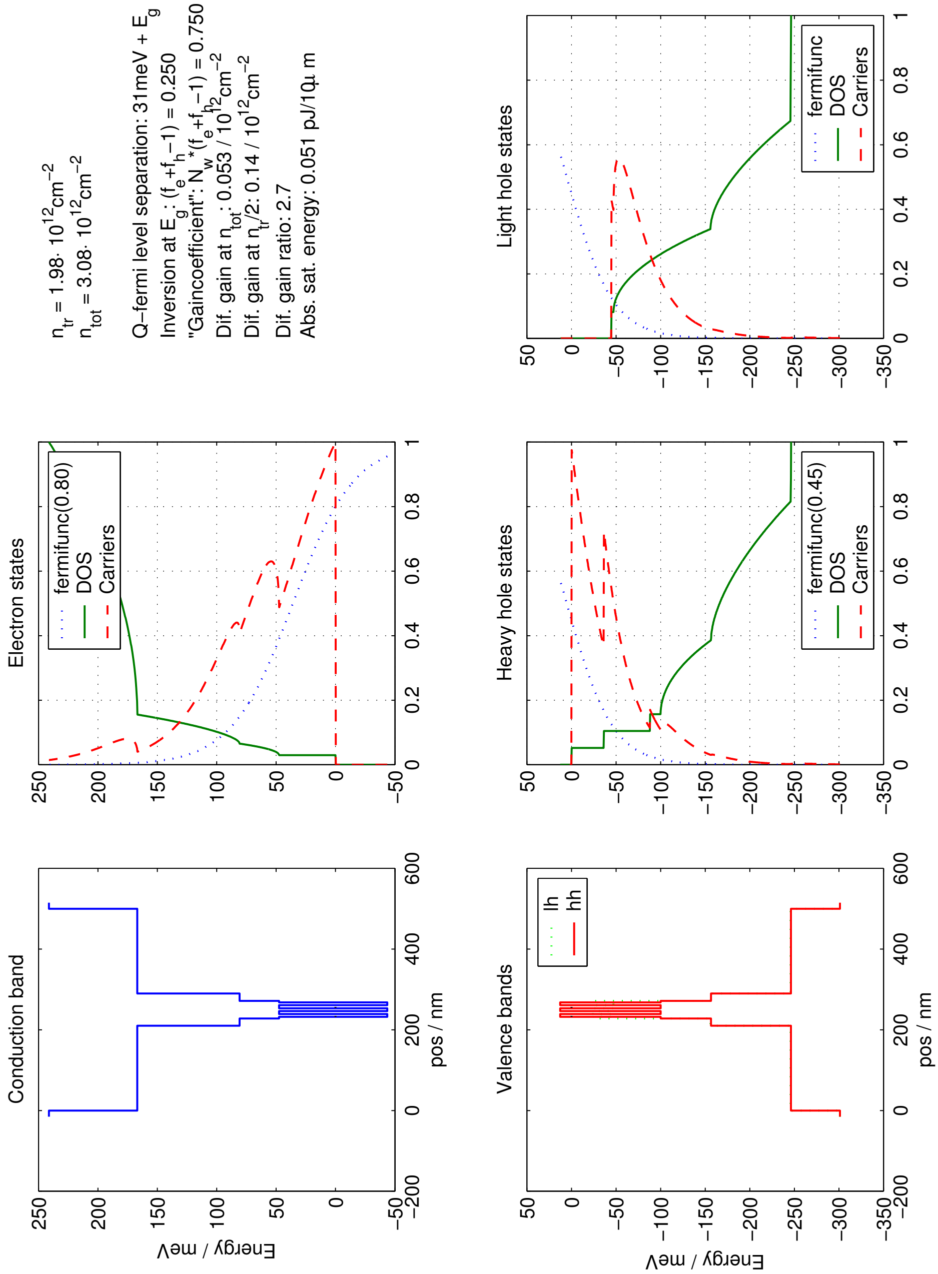

Figure 3.4: 3 QW "LOC" laser structure. See Fig. 3.3 for extended caption.

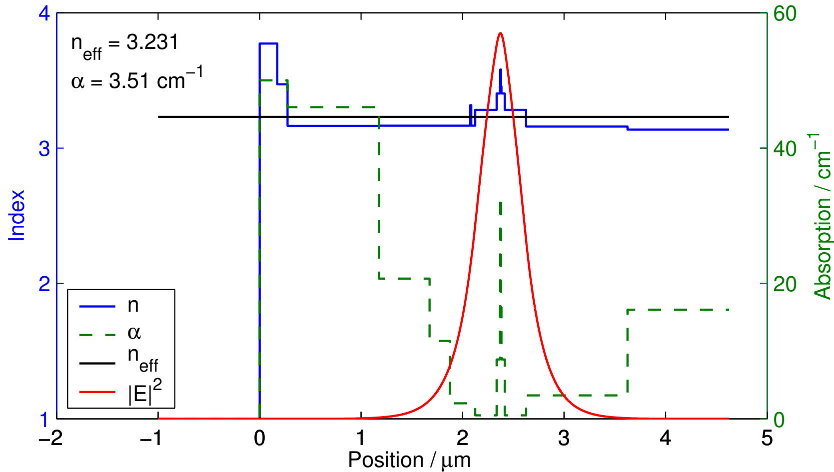

Figure 3.5: 1D mode calculation using the shown index (n) and loss (α) profile, i.e. under the ridge of the structure in Table 4.2.

they are spatially positioned far away from the wells, it is desirable to have a low density in these layers. Given that the density of states in the SCH is very large and the position of the quasifermi levels intentionally is far up into the bands the requirement of low density in the SCH region translates into a requirement of a high bandgap in the SCH layers. Due to difficulties growing low arsenic containing InGaAsP the composition used for the actual devices and also in the shown figures is Q(1.06)[2]. It should also be noted that Coloumb effects, which are neglected, will even out spatially different electron and hole distributions through modification of the band structure, i.e. effectively making the electron barriers larger [148].

Since the transport time across the SCH ($\sim 100\ ps$[109]) is much larger than the pulse width the carriers for amplification of a pulse has to be "in place" since they will not be refilled through injection during the pulse. For the lasers fabricated a "carrier reservoir" of total width (i.e. including the quantum wells) of 80 nm and composition Q(1.29) is used to ensure that enough carriers are present close to the quantum wells. Even for CW lasing the finite capture time from the carrier reservoir has an impact on the high power properties due to an increased carrier density in the reservoir for increased power with increased free-carrier loss as result [110, 111].

One might expect that carriers that are in the same (QW) bands as the emitting state can scatter into the active states very fast, since they do

[2] Q(λ) denotes the quarternary InGaAsP compound that has a bandgap of λ μm and is lattice-matched to InP

not have to move in real space. Also, a very high carrier density will make the scattering rate very high and this should also reduce the spectral hole burning in the gain section.

A potential problem with the high carrier density is non-radiative Auger recombination and free-carrier absorption. The first will reduce the quantum efficiency of the device and heat the carrier distributions, but it can also contribute to a fast recovery of the gain through scattering into the active states. The free-carrier absorption on the other hand has no positive effects and it has to be minimized by not having more carriers than necessary in the reservoir.

Another issue is whether distributed gain or a short gain section is to be preferred. Normally the former would be desired as the changes in pulse power is smaller, but it depends on the noise figure of the amplifier. In the present case the noise figure could be quite good as the amplifier is highly inverted and polarization dependent (as opposed to e.g. EDFAs), and the signal to be amplified is strong. The low gain per length will also reduce the amount of carriers that need to be transported to the gain region and it can therefore contribute to lowering the gain compression and SHB. Also, the fact that only a small fraction of the total carrier population is interacting with the photons, combined with the high inversion, makes the gain less affected by carrier heating.

Using similar design principles, but using tensile strained 50 nm bulk material to achieve polarization independence, Morito et al. have fabricated an SOA with high saturation power (17dBm), low noise figure (6.3dB) and low eye distortion at 10 Gbit/s [149, 150]. Also, dot-based amplifiers, again with the same type of arguments have been predicted to provide both high output power and low noise[151].

It is of course possible to reduce the number of quantum wells (below 3) and in Fig. 3.6 and 3.7 the carrier distribution is shown for 2 and 1 QW assuming the same gain coefficient in all cases. As would be expected the differential gain is lowered with fewer wells as is the transparency carrier density. A comparison of gain vs. carrier density for structures with 1,2 and 3 QWs is shown in Fig. 3.8. It is seen that the differential gain is always lower for the 1 QW structure but a very large carrier density might be necessary to reach the required gain. With fewer wells the inversion needs to be larger, i.e. the quasifermi levels have to be moved further into the bands which means that the population in the higher states become larger. This might ultimately lead to higher states getting net gain and in extreme cases (high loss) that the device lases on a higher transition. In order to achieve gain the quasifermi levels should at least be separated by

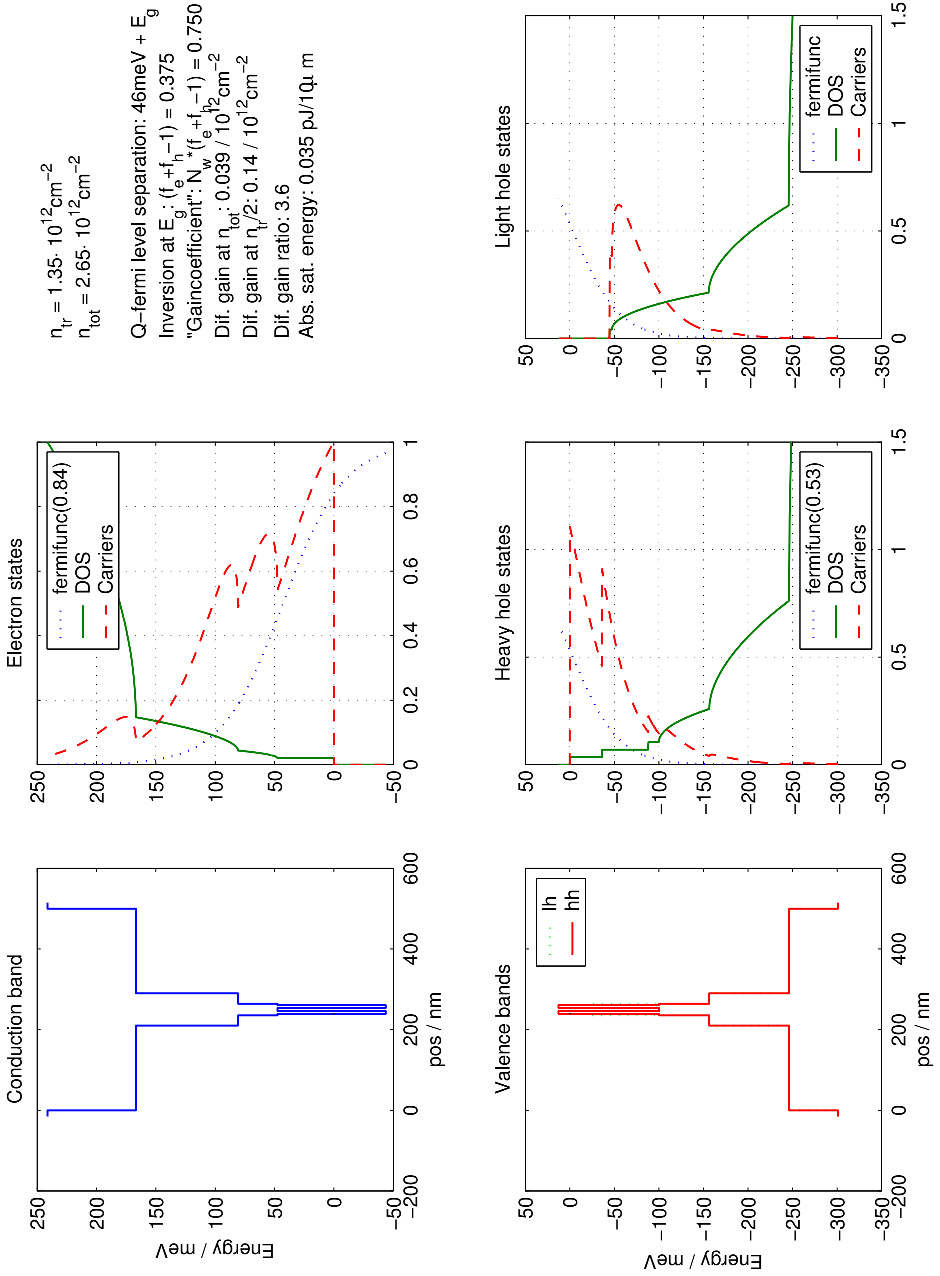

Figure 3.6: 2 QW "LOC" laser structure

the photon energy and from Fig. 3.7 it can be seen that in the case of the 1 QW device, at the chosen required gain, the c-lh1, ”continuum”-hh2 and ”carrier reservoir”-hh1 transitions might be a problem. The magnitude of the gain, however, would have to take the wavefunction overlap into account. Even if the device does not lase on these transitions the increased ASE at these wavelength will add to the noise. The problem is reduced for structures with lower loss, where less gain is required for lasing. At the same time, however, this would also reduce the saturation energy.

The effect of the carrier reservoir of course increases with carrier density due to the approach of the quasifermi functions towards the reservoir states.

The step formed by the Q(1.29) has another important function in the absorber in that it significantly aids the carrier transport away from the well. The carrier escape is mainly through thermionic emission with an exponential dependence on the barrier height, thus dividing the barrier into steps is crucial for a fast absorption recovery [152].

3.4 Ideal monolithic structure

The structures described above are the ones fabricated as part of this project. If regrowth technology is used such that the epitaxial material used for the gain and absorber is different it might be possible to optimize the sections further.

Several types of mode-locked lasers employing regrowth technology has been demonstrated e.g. [124, 153–155], but they all use identical material for gain and absorber and use the regrowth step to make a passive section including a bragg grating. Without increasing the complexity of the processing it would be possible to make a device using the principles of this section and (hopefully) get a better performance.

Other methods than butt-coupling waveguides to achieve active and passive sections for mode-locked lasers have been demonstrated. Selective area epitaxy, where diffusion of growth species across SiO_2 masking gives thickness and composition variations across the wafer, [140], growth on non-planar substrates [137] and quantum well intermixing [141, 142] has been used. Sato et al. [95, 156–159] uses a MQW stack with both gain and absorber wells and etch away the gain wells in the absorber and passive part. The advantage of these methods, besides ease of fabrication, is that very good coupling between the waveguides is automatically achieved with low reflection compared to typical butt-coupling results. The problem, however, is that the different sections cannot be optimized independently.

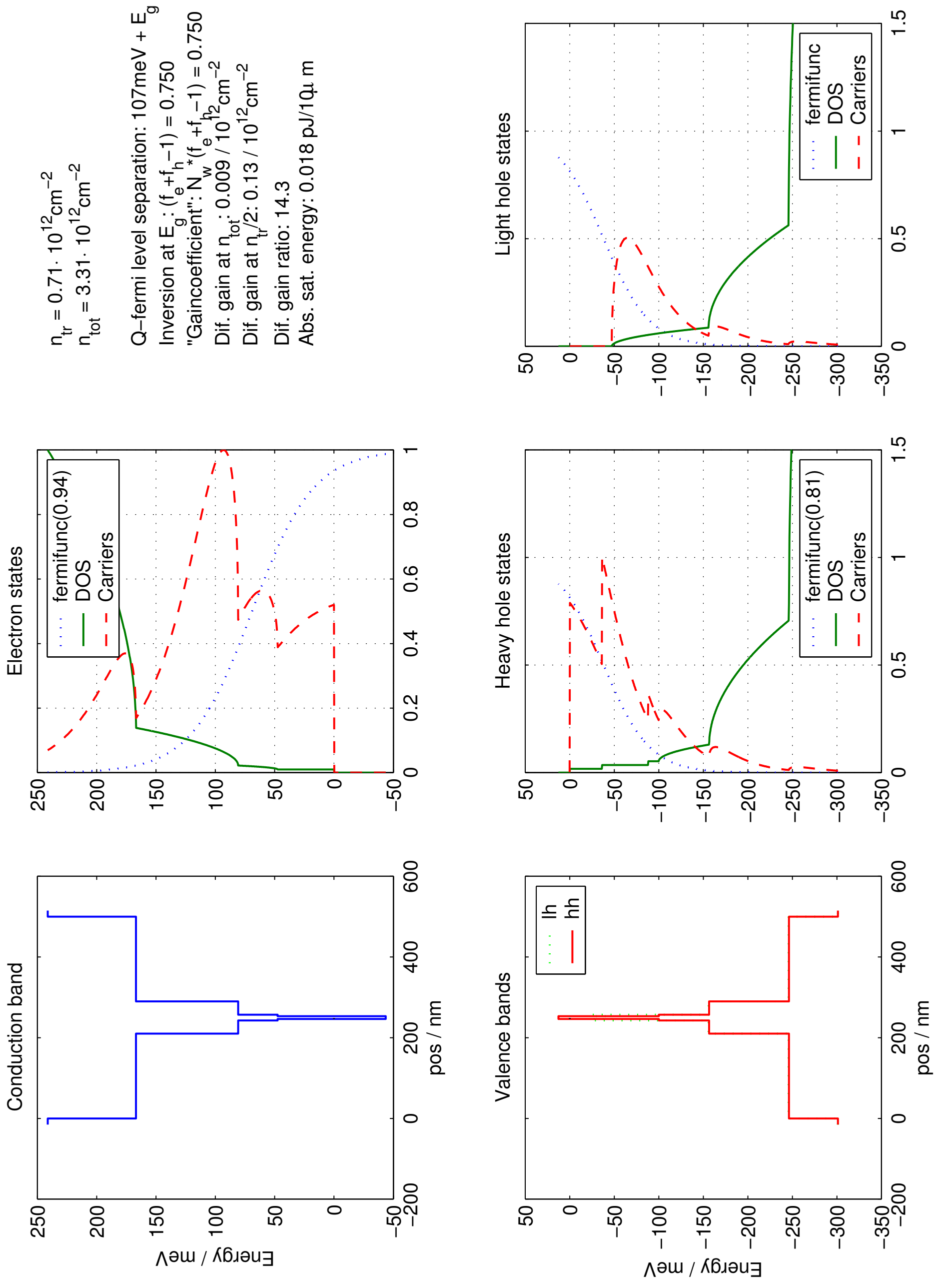

Figure 3.7: 1 QW "LOC" laser structure

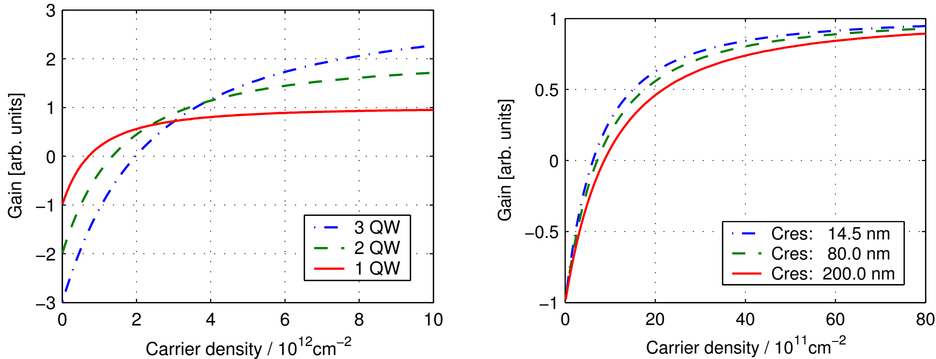

Figure 3.8: *Left*: Gain versus carrier density for structures with 1, 2 and 3 QWs. *Right*: Gain versus carrier density for 1 QW structure with different "carrier reservoir" width (Cres).

3.4.1 Gain section

If the epitaxial structure used for the gain section is not to function as absorber also it would not be necessary for carriers to escape from the wells and a structure that would allow a higher inversion could be made. One could imagine that a deep narrow highly strained well would be advantageous as this will increase the splitting between lowest hh-state and higher hh-states and lh states thereby making possible a higher inversion without lasing on higher transitions. This would be the case until the population of the unstrained SCH layers becomes important. Since the lighter electron is more affected by the quantum confinement than the heavy hole, the lowest electron state is moved closer in energy to the SCH by the more narrow well assuming the same emission wavelength. Incidentally, higher compressive strain will also decrease this separation as can be seen comparing the conduction band deformation potential with the "sum" of the hole deformation potentials (see Table C.1). A possible way around this problem would be to use p-doping in the well to move the fermilevels down. Thus, instead of a fully inverted conduction band, a more symmetric inversion of both conduction and valence band is achieved. Using p-doping introduces excess loss which could be a problem, but even through a very high doping density of $3 \cdot 10^{18} cm^{-3}$ $(1.2 \cdot 10^{12} cm^{-2})$ is used in the well in Fig. 3.10 the 2D density is $1.2 \cdot 10^{12} cm^{-2}$ and the sum is of the same magnitude as for the 1 QW design in Fig. 3.7. Equally importantly, all the carriers in the structure are located "in the wells", and the density is extremely large, so the recovery from SHB should be fast due to the large carrier-carrier scattering rate. The ultrafast gain suppression is therefore reduced and subpicosec-

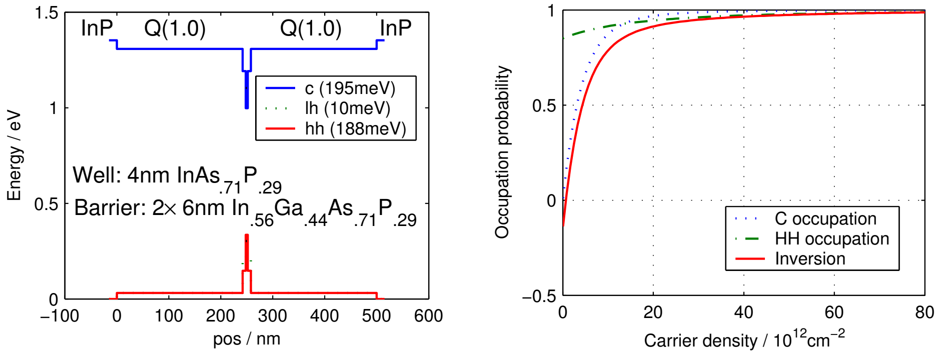

Figure 3.9: *Left*: Band structure for "ideal" gain section. *Right*: Occupation propabilities and inversion as function of carrier density with p-doping of $3 \cdot 10^{18} cm^{-3}$ in the well

ond pulses more feasible. Even though it would have been desirable, the maximum gain would not be changed much with this design[160].

There are a number of potential challenges in fabrication the suggested structure. The thick Q(1.0) layers will be difficult to grow due to the low arsenic content, but Q(1.06) as used above and fabricated in practice will also be feasible. The wells are highly compressive strained (2.2%) which corresponds to a critical thickness of 3 nm for a single layer(using the theory of Matthews and Blakeslee [161, 162]). Strain compensation using tensile strained barriers is used such that the critical thickness for a sandwiched layer should be used and this value is 8 nm, and it should thus be feasible. The composition of the barrier layer is in the middle of the miscibility gap for the InGaAsP system, and there is therefore a risk of growth instabilities [163, 164]. However, the layers are few and thin, so it might be possible. Using InAlGaAs barriers is another solution as this material system has a smaller miscibility gap than the InGaAsP system [164, 165]. The doping density used is quite high and some diffusion would be expected if Zn is used. This might intermix the quantum well and barrier, thus making the fabrication process non-reproducible. The use of the same As/P ratio in the two layers minimizes this problem, but it might be advantageous to use a less diffusive dopant for this layer.

3.4.2 Absorber section

Using the gain epitaxial structure for the absorber makes the absorber very long and it requires a large voltage swing to synchronize the device due to the low confinement factor and thick un-doped layers. This is not ideal.

If cleaving is used to define the absorber length, a minimum length

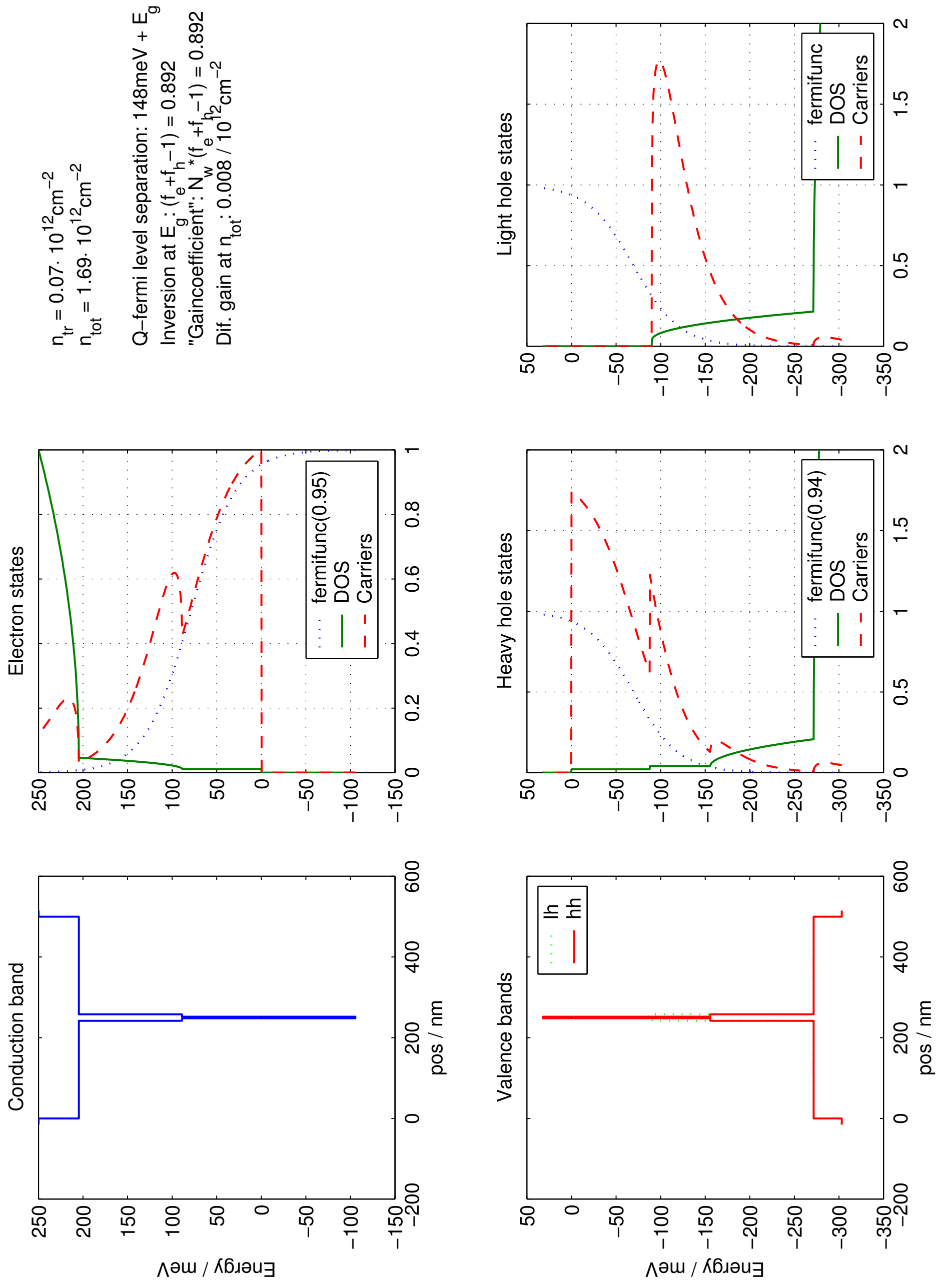

Figure 3.10: Carrier distribution for "ideal" gain section and p-doping of $3 \cdot 10^{18} cm^{-3}$ in the well

of 20μm would be preferred to ensure reproducibility (assuming a cleaving accuracy of 5μm). A short absorber is desirable, such that the self-colliding effect is not reduced, because the absorber has time to recover during the pass. A length of 20μm corresponds to a transit time of approximately 0.5 ps. Having chosen the length of the absorber, the next step is to increase the confinement factor such that the saturation energy is sufficient for stable mode-locking with only a few volts reverse bias on the absorber. The absorber material could be both bulk or quantum well. Quantum wells might be advantageous if modulation is used to synchronize the device due to the higher absorption change possible using the quantum confined stark effect (QCSE) compared to the Franz-Keldysh effect. On the other hand, bulk saturable absorbers have been predicted to have a more ideal ultrafast dynamics but this is still unclear[115]. An important issue limiting the thickness of bulk absorbing material or the number of quantum wells is the need to have a good mode overlap (coupling) between the absorber and gain section. A good choice might be 6 QW with a stepped narrow SCH to aid carrier escape. The capacitance of the modulation section is also a potential problem, but due to the short length the junction capacitance will not be the limiting factor for modulation.

One issue not yet discussed is the need for a phase section to fine-tune the repetition rate, through current injection or reverse bias. The epitaxial material used for the absorber might be good for this as the proximity of the band edge to the wavelength of interest makes the refractive index shift much larger compared to the common choice of e.g. Q(1.3) material for passive sections [71]. The problem is of course excess loss but if quantum wells are used, the ”on-state” loss of the ”passive” section could be made small, in part because it can be made quite short and still provide the necessary refractive index change. The same arguments can be used for using the absorber epitaxial structure for a monolithic Bragg grating.

3.4.3 Waveguide

The thickness of the SCH layers in the gain section is chosen such that the mode is confined under the ridge when the latter is etched to just above the SCH layers. A thicker SCH region would lower the loss but the mode would spread out vertically, unless the ridge etch is continued down through the quaternary layers. If a buried heterostructure is used, the thickness of the SCH layers could be increased until the onset of the third mode of the vertical structure and the loss could be reduced.

For the absorber section an arbitrary number of quantum wells could be used and the mode matching could be done adding high-index doped

SCH layers. This would make the absorber strongly multimode, but due to the short length no significant mode conversion would take place. Doping the SCH to avoid decreasing the electric field across the quantum wells for a given applied voltage will give excess loss, but again the short length reduces the problem.

In the discussions above an index guided structure has been assumed, but it might also be possible to make a gain guided version of the device. In that case a flared structure, with the absorber in the narrow end, should be used to increase the "cross-section" compared to the gain section. Even though such a structure could increase the output power, it will not improve the jitter performance as this still depends on the power density in the cavity.

3.5 Alternative materials

An ultimate limit on the jitter is set by the pulse energy that can be sustained in the laser cavity. For semiconductor lasers this is ultimately set by two-photon absorption, but also electron transport issues might come into play (increased loss due to high carrier densities that result from the finite capture times). Here solid state glass-based lasers will have an advantage due to the high "bandgap" of the glass matrix and low cross-section of the gain material.

A way of avoiding the problem of two-photon absorption could be to use a 1.55 μm quantum dot based gain material on a GaAs substrate and use an AlGaAs separate confinement heterostructure with a bandgap larger than $2 \times 0.8eV$. Dots have been demonstrated for a mode-locked laser at 1.3μm[166] and 1.1μm[167] but the performance has so far been poor, probably due to the absence of a good absorber. The challenge is thus not only to produce dots at 1.55μm but also to make a good high-confinement (QW based) absorber on GaAs working at 1.55 μm.

InAs quantum dashes, i.e. elongated dots on InP have been used for gain material at 1.55μm [168] and they might be a way to lower the confinement factor further for long lasers, e.g. at a repetition rate of 10 GHz.

AlInGaAs/AlGaAsSb materials have a type II lineup for some compositions, meaning that the electrons and holes are not located spatially in the same place. This reduces both the spontaneous emission and gain and might be useful for long lasers [169]. Incidentally an applied electric field will increase the overlap significantly, which will make a short absorber feasible. Thus, these materials with a few quantum wells might be employed as high-confinement factor absorbers as well as a high saturation energy

gain section.

3.6 Summary

Most often the designs of absorption modulated mode-locked lasers have concentrated on the absorber dynamics in order to produce short pulses and not much attention has been put on design of the gain section. It turns out, however, that the gain section is responsible for most of the dynamic pulse changes and if it is made more ”linear” the requirement to the absorber is relaxed significantly as less pulse shaping is needed pr. pass. Design guidelines for low loss and high inversion structures have been presented in this chapter along with some examples of manufacturable structures.

The theory used to design the structures has been quite simple and in order to make quantitative calculations of gain etc., more sophisticated band models, broadening etc. should be used and details can be found in many textbooks e.g. [132, 162, 170]. Using such a material model, new dynamic calculation should be made incorporating the absorber and gain dynamics as well as propagation effects.

Chapter 4

Device fabrication

In this chapter, I shall describe the practical realization of the designs from Chap. 3, and the basic measurements done to verify that good material quality was produced.

The amount of detail in the different sections will reflect the level of contribution from me, so for instance growth issues will be overweighed compared to the rest of the process.

4.1 Wafer growth and processing

A schematic of the desired ridge waveguide structure is shown in Fig. 4.1 together with a blowup of the active layers for a 10 QW structure. The epitaxial structure for a 10 QW laser (growth number G511) is shown in Table 4.1 along with a brief explanation of the function of the different layers. In order to easily remember the main features of the wafer structure, I shall use aliases like SCOOP5_10, where SCOOP5 is a batch identifier and _10 means 10 QW. Similarly SCOOP6_3 is a 3 QW wafer from the SCOOP6 batch.

The detailed design considerations for the wafers were presented in Chap. 3.

4.1.1 Growth

The epitaxial growth is performed using metal-organic chemical vapor deposition (MOCVD) in an Aixtron AIX200 first commissioned in 1988. The precursors used are trimethylindium (TMIn) and trimethylgallium (TMGa) for the group III atoms while arsine (AsH_3) and phosphine (PH_3) were used for the group V atoms. Diethylzinc (DEZn) is used to provide Zn p-doping,

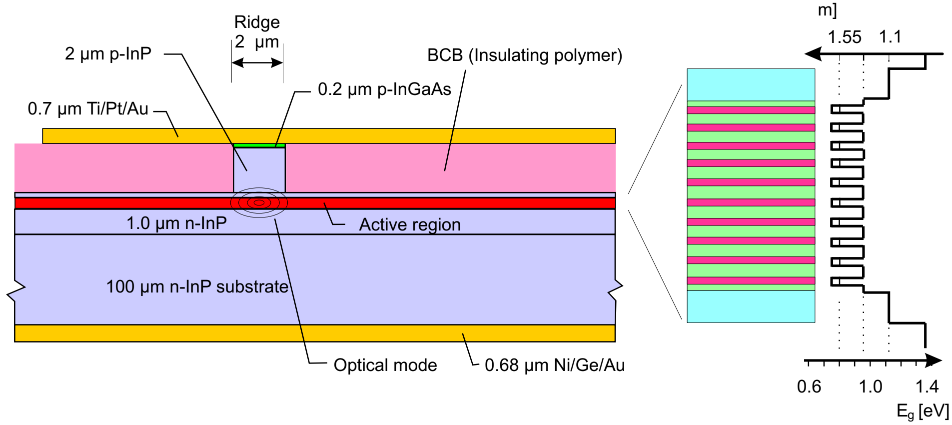

Figure 4.1: Schematic of the final ridge waveguide structure. All numbers are approximate.

Material	Dopant conc.	Thickness	Function
InP:Zn	?	25 nm	Protective layer
Highly doped InGaAsP contact layer			
InP:Zn	$2 \cdot 10^{18}\text{cm}^{-3}$	1000 nm	Upper cladding
InP:Zn	$9 \cdot 10^{17}\text{cm}^{-3}$	700 nm	Upper cladding
Q(1.1):Zn	$9 \cdot 10^{17}\text{cm}^{-3}$	10 nm	Etch stop
InP:Zn	$9 \cdot 10^{17}\text{cm}^{-3}$	80 nm	Upper cladding
InP	Diffused from ↑	60 nm	”Standoff layer”
Q(1.13)		36 nm	SCH
$\text{In}_{1-x}\text{Ga}_x\text{As}_y\text{P}_{1-y}$			Quantum wells
x=0.507, y=0.845		4.5 nm	Barrier
x=0.258, y=0.845		8 nm	Well ×10
x=0.507, y=0.845		9 nm	Barrier ×9
x=0.507, y=0.845		4.5 nm	Barrier
Q(1.13)		36 nm	SCH
InP:Si	$1.5 \cdot 10^{18}\text{cm}^{-3}$	1000 nm	Lower cladding
InP:S	$\sim 7 \cdot 10^{18}\text{cm}^{-3}$	∼350 µm	n-type substrate

Table 4.1: The epitaxial structure of SCOOP5_10. The shorthand notation Q(λ) denotes the $\text{In}_{1-x}\text{Ga}_x\text{As}_y\text{P}_{1-y}$ compound that is lattice matched to InP and has a band-gap corresponding to a wavelength of λ µm. Zn is p-type dopant, while Si and S are n-type dopants.

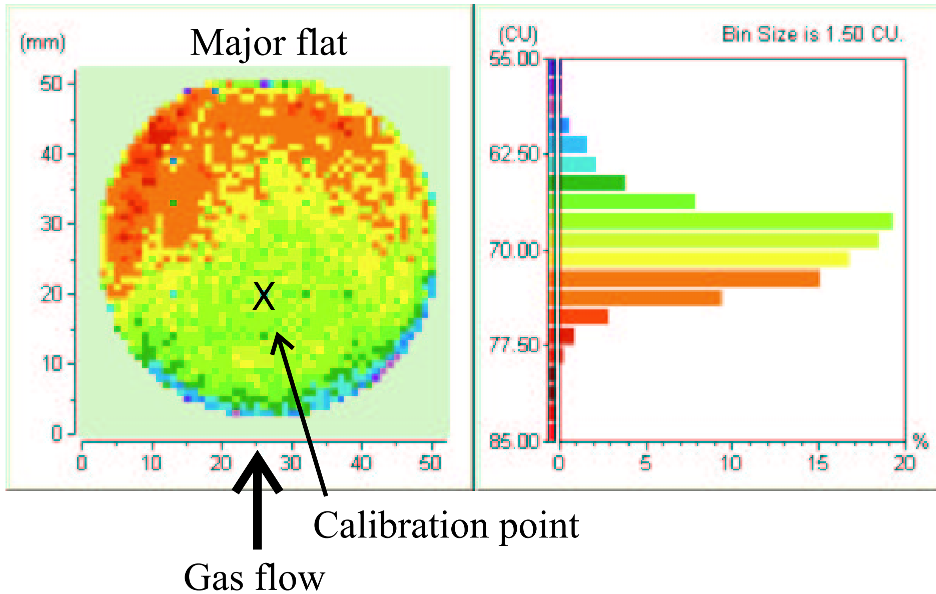

Figure 4.2: Peak intensity of photoluminescence from calibration wafer with the wells and SCH region from the 3 QW design in Table 4.2. See Fig. 4.3 for peak wavelength.

and silane (SiH_4) is used for n-doping. Hydrogen is used as carrier gas and the total gas flow is around 6.7 l/min during growth. An overpressure of phosphine and arsine is used when the wafer is heated to prevent outdiffusion of As and P. Thus, the partial pressure of TMGa and TMIn determines the growth rate (see [164] for details on growth).

The MOCVD apparatus used does not have a rotating susceptor, which means that there are quite large variations across the wafer due to gas depletion and temperature gradients. The composition values quoted in this chapter are all from a calibration point located 7.5 mm away from the center towards the gas entrance (see Figs. 4.2 and 4.3), since most calibration runs were done on quarter wafers.

The quantum well active region for all the wafers is a so-called *constant y, zero net strain* (CY, ZNS) structure [171]. The constant y is referring to the fact that the ratio of the group V precursors are kept constant during growth of the $In_{1-x}Ga_xAs_yP_{1-y}$ wells and barriers. Due to the high partial pressure and strong incorporation of As there is a memory effect in the reactor if the As/P ratio is changed. This is a problem for quantum wells where abrupt interfaces is desired. Also, choosing a CY design results in a typical well width of 7-9 nm for 1550 nm emission. This, combined with a lower interdiffusion of P/As compared to In/Ga, makes

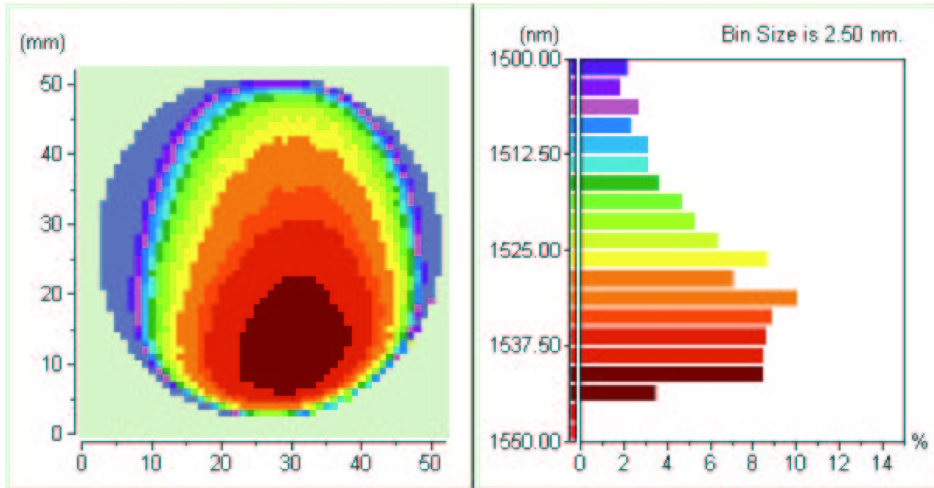

Figure 4.3: Peak wavelength PL-map of the same wafer as Fig.4.2

the emission wavelength less sensitive to thermal treatment, during both the initial growth and subsequent processing/regrowth [172, 173].

The zero net strain design $\varepsilon_w L_w + \varepsilon_b L_b = 0$, where ε_x and L_x are the in-plane strain and thickness of the well (w) and barrier (b), allows the growth of many wells without strain relaxation [161, 174].

A problem with growing many highly strained QWs is the possibility of growth instabilities, where the layers start to grow three-dimensionally, the so-called wavy-layer growth [163]. The growth conditions used initially for the quantum wells were a growth temperature of T_g=640°C, reactor pressure P_g=22 mbar and V/III partial pressure ratios of ∼540 and ∼390 for the well and barrier respectively. Even though these parameters had produced some good wafers, it turned out that they were too close to the unstable region for the alloys. Small process variations suddenly gave reduced PL intensity and poor structural quality as shown in the xray scan in Fig. 4.4 (left), where the satellite peaks from the superlattice are poorly defined.

The wavy-layer problem is related to the miscibility gap of the InGaAsP material system, arising from different atom sizes, making it is energetically favorable to form two phases of different composition. MOCVD is not, however, an equilibrium process so the limited miscibility is not an unsurmountable barrier. A number of authors have reported ways of minimizing the wavy-layer problem by reducing the time and opportunity the group III atoms have to form separate phases, by ensuring a fast surface

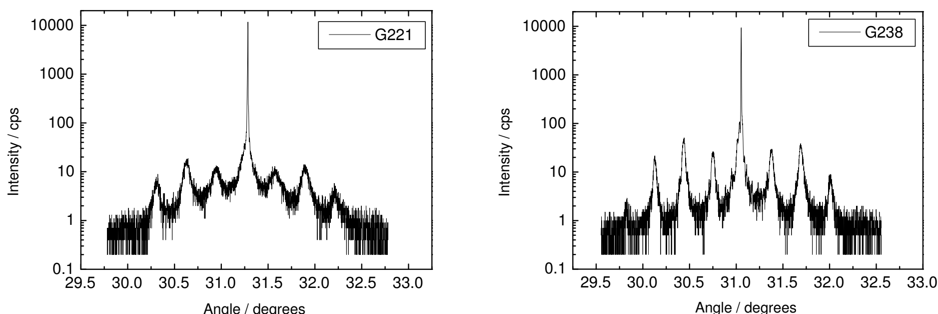

Figure 4.4: High-resolution Xray diffraction measurement ($\lambda = 1.540597$Å) on two wafers with ten 8 nm CY, ZNS QWs *Left*: Wafer suffering from wavy-layer growth (integration time 4.5 s/point) *Right*: Wafer grown using optimized growth conditions (integration time 4.1 s/point).

coverage of As and P [163, 175–177]. This can be done by increasing the partial pressure of the group V elements, either by increasing the precursor flow, the reactor pressure or the growth temperature, the last two through an increase in the cracking efficiency of phosphine.

We chose to increase the reactor pressure to 50 mbar and increase the flow of the hydrides equivalent to a V/III partial pressure ratio of ~770 and ~560 for the well and barrier respectively. Also, 1 s growth interrupts, where the TMIn and TMGa flow was stopped, for each composition change were employed and this also improved the material slightly. Figure 4.4 (right) shows the much improved xray rocking curve for the optimized material.

When the reactor pressure is altered, the cooling of the susceptor changes as well, and this gives rise to temperature excursions of several degrees. The gallium and indium incorporation is mass transport limited and is not affected by this, but the As/P ratio is temperature dependent mostly because of the incomplete pyrolysis of the phosphine. We therefore chose to change the pressure in the lower InP cladding 1 min before switching to quaternary compounds, so the temperature had time to stabilize. Thus, the Q(1.13) layers in Table 4.1 are grown at 50 mbar also.

For the 1, 2 and 3 QW LOC type wafers the nominal epitaxial structure is shown in Tables 4.2 and 4.3. Much effort was put into growing the thick high bandgap layer (Q(1.06)) layer at 50 mbar, but even for a well-matched layer, the xray peak was broadened and the wafer surface was not specular. Part of the problems were due to a malfunctioning mass-flow controller driven beyond it's calibrated range and old electronics, but the final solution was to go back and grow the layer at 22 mbar. The reason

for the poor morphology at 50 mbar is not known, but parasitic gas-phase reactions, combined with the delicate control needed for the low As alloys, is most likely the reason. The QWs were still grown at 50 mbar and a 45 s growth interrupt was employed before and after the wells to stabilize the temperature as indicated in the last column of Table 4.2.

All layer compositions in Table 4.1 and 4.2 have been calibrated by growing test structures. For the lattice-matched material typically two layers (thickness ∼200 nm) with slightly different gallium flows, resulting in a compressive and a tensile layer, have been grown. If the wavelength is sufficiently close to the desired, the gallium flow for lattice-match is calculated from linear interpolation of the measured xray mismatch. A well-matched layer should have a mismatch of less than 1000 ppm measured using xray.

For the quantum wells, the procedure is a bit more complicated, due to the high strain, since it is difficult to grow good materials of sufficient thickness to avoid quantum effects in the PL emission. Layers of approximately 40 nm thickness is therefore grown using the same AsH_3/PH_3 ratio in the two layers. Xray is measured from both layers and PL is measured from the top layer. This layer is then etched away, and the PL is measured from the second layer. From the two mismatch values and two PL values (for strongly tensile layers the c-lh transition is used) one can then calculate the composition of the layers as shown in Fig. 4.5 using the same theory as Chap. 3 and appendix C. The procedure is to calculate all the states in a quantum well, assume that only states with the same quantum number emits light, and then find the peak wavelength assuming a Boltzmann carrier distribution. The calculation is done varying the layer thickness around the approximate thickness calculated from the growth parameters. The exact thickness is not known and the emergence of a new state as peak wavelength might make the result inaccurate. Assuming that the y-value is approximately the same in the two layers we obtain a thickness of 38 nm and composition $In_{0.732}Ga_{0.268}As_{0.86}P_{0.14}$ for the compressive layer and a thickness of 42 nm and composition $In_{0.470}Ga_{0.530}As_{0.86}P_{0.14}$ for the tensile layer.

4.1.2 Processing

After xray characterization of the wafer, the top InP layer is removed in a 1VP HCl : 4VP H_3PO_4 etch[1], which is selective in the sense that it does not etch InGaAs. A thin, typically 100 nm, layer of glass (∼SiO_2)

[1]VP: Volume part. The HCl concentration is 32% while the H_3PO_4 concentration is 85%

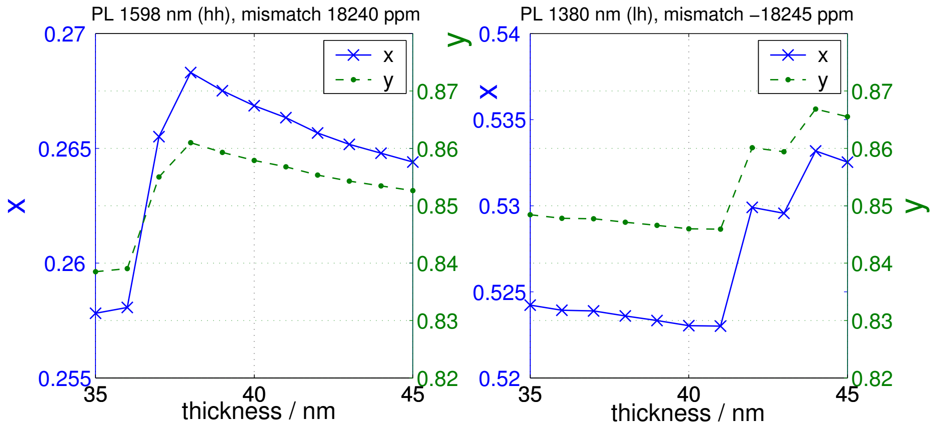

Figure 4.5: Calculation of composition for the highly strained materials used for the quantum wells. The measured layer mismatch (from xray) and emission wavelength (from PL) are written above the figures. *Left*: Compressive layer *Right*: Tensile layer

Material	Dopant conc.	Thickness	Growth notes
InP:Zn	?	25 nm	
Highly doped InGaAsP contact layer			
InP:Zn	$2 \cdot 10^{18}\text{cm}^{-3}$	900 nm	
InP:Zn	$9 \cdot 10^{17}\text{cm}^{-3}$	500 nm	
InP:Zn	$5 \cdot 10^{17}\text{cm}^{-3}$	200 nm	
InP:Zn	$1 \cdot 10^{17}\text{cm}^{-3}$	200 nm	
Q(1.1):Zn	$1 \cdot 10^{17}\text{cm}^{-3}$	10 nm	
InP:Zn	$1 \cdot 10^{17}\text{cm}^{-3}$	40 nm	
Q(1.07)		200 nm	
Q(1.29)		18 nm	P=22mbar
$In_{1-x}Ga_xAs_yP_{1-y}$			
x=0.530, y=0.86		3.7 nm	
x=0.268, y=0.86		7.2 nm	×3
x=0.530, y=0.86		7.3 nm	×2
x=0.530, y=0.86		3.7 nm	P=50mbar
Q(1.29)		18 nm	
Q(1.07)		200 nm	
InP:Si	$1.5 \cdot 10^{18}\text{cm}^{-3}$	1000 nm	$T_g = 640°C$, P=22mbar
InP:S	$\sim 7 \cdot 10^{18}\text{cm}^{-3}$	∼350 μm	epi-ready substrate

Table 4.2: The epitaxial structure of SCOOP6_3. For the growth parameters the table should be read bottom-up as this corresponds to the growth sequence.

Material	Thickness	Material	Thickness
Q(1.29)	26 nm	Q(1.29)	33 nm
$In_{1-x}Ga_xAs_yP_{1-y} \times 2$		$In_{1-x}Ga_xAs_yP_{1-y}$	
x=0.530, y=0.86	3.7 nm	x=0.530, y=0.86	3.7 nm
x=0.268, y=0.86	7.2 nm	x=0.268, y=0.86	7.2 nm
x=0.530, y=0.86	3.7 nm	x=0.530, y=0.86	3.7 nm
Q(1.29)	26 nm	Q(1.29)	33 nm

Table 4.3: Thicknesses of "active layers". *Left*: SCOOP6_2. *Right*: SCOOP6_1. The rest of the structures are identical to SCOOP6_3 in Fig. 4.2.

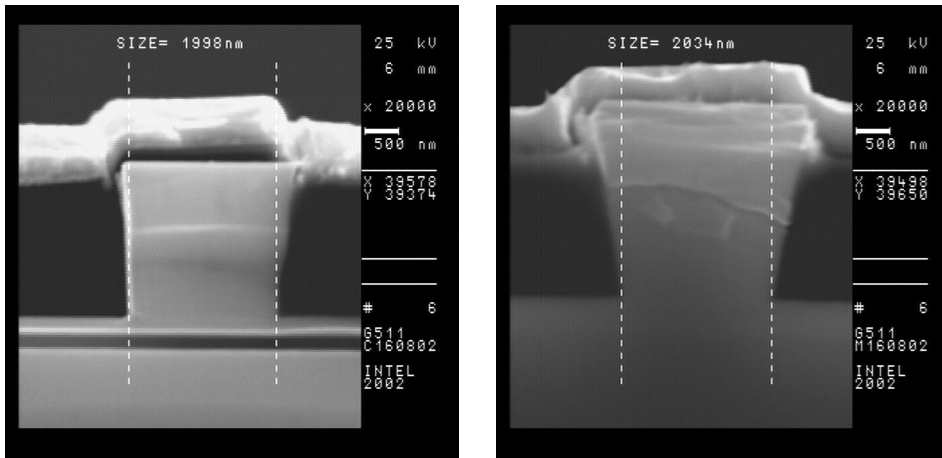

Figure 4.6: Scanning electron microscope images of fully processed samples *Left*: Ridge along $[0\bar{1}\bar{1}]$. This sample was etched 15 s in 1 H_2SO_4 : 8 H_2O_2 : 8 H_2O to reveal the quantum wells and contact layers. *Right*: Ridge 7° off $[0\bar{1}\bar{1}]$ showing an increased angle.

is deposited using plasma enhanced chemical vapor deposition to protect the contact layers and act as etch mask for the ridge etch. Using standard photo-lithography the ridges are defined in a ~1.4 μm layer of photo-resist and subsequently transferred to the glass using a freon-23 (CHF_3) based reactive ion etch (RIE). Another RIE etch, based on cycles of oxygen and methane/hydrogen, is used to etch through the InGaAsP contact layer, which then can act as a perfect etch mask for a new 1VP HCl : 4VP H_3PO_4 etch. The thickness variation across the wafer is more than 10%, due to the lack of rotating susceptor, and the total etch depth is around 2 μm, so a timed dry or wet etch would not give a sufficient accuracy for the waveguide. A 10 nm Q(1.1) etch stop layer is therefore used allowing more than 5 min over etch.

The 1 HCl : 4 H_3PO_4 mixture etches InP anisotropic and for ridges

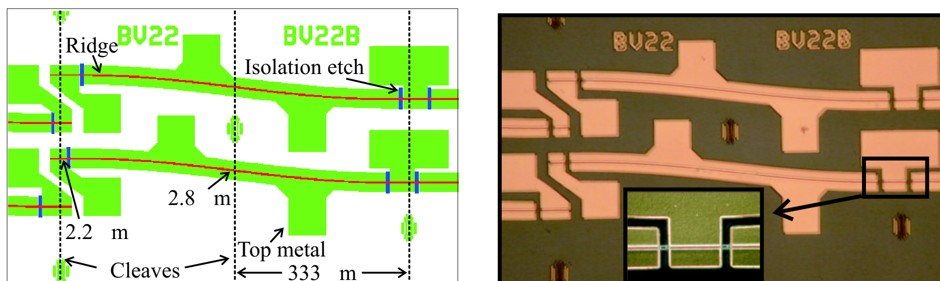

Figure 4.7: *Left*: A small part of the "SCOOP4" mask set showing a number of angled multi-section MLLs. *Right*: Photograph of processed device. Inset: Separation etch between absorber and gain section.

defined with an InGaAs mask along $[0\overline{1}\overline{1}]$ almost square ridges are formed as shown in Fig. 4.6 (left). For ridges at an angle to $[0\overline{1}\overline{1}]$ the sidewall angle decreases as shown for a 7° angle in Fig. 4.6 (right). The sidewall angle (α) as function of waveguide angle (ϑ) is approximately [178]

$$\alpha = 87.8^\circ - 1.4\vartheta \tag{4.1}$$

As explained in Sec. 5.2.2, a 2 μm ridge is used for our design and it is therefore necessary to calculate the mask width using the ridge height, Eq. (4.1) and simple geometry. For the bend in Fig. 4.7, the mask width should be gradually increased from 2.2 μm to 2.8 μm to ensure a constant width of 2 μm in the bottom of the ridge.

In order to have electrical separation between the different sections of the laser, the highly conducting contact layer are removed by a new photolithography step, RIE etching of the SiO_2, and wet etching of the contact layer. The wet etch is an InGaAs(P) selective etch (1VP H_2SO_4 : 8VP H_2O_2 : 8VP H_2O)[2], so the two upper layers are removed. A 5 μm opening in the mask results in a few kΩ isolation between sections.

The wafer is planarized using a benzocyclobutene polymer (BCB[3]), which is spun on the wafer at approximately the same thickness as the ridge. After curing a mask-less RIE etch is used to expose the top of the ridges.

Photolithography is performed again to prepare for a metal lift-off of the top metals. Shortly before putting the wafers in to the vacuum chamber for the metal deposition, the remaining SiO_2 on top of the ridges is removed by BHF. Topmetals are standard Ti/Pt/Au.

[2] 96% H_2SO_4, 31% H_2O_2

[3] DOW chemicals: Cyclotene^{TM} 3022-35.

The wafer is thinned to about 100 μm and the n-metals Ni/Ge/Au are deposited on the backside and annealed. Most of the devices were soldered to a submount, and for this purpose an additional Ti/Pt/Au stack similar to the p-metals were deposited.

More information on the processing and a more detailed explanation the purpose and physics of the different process steps can be found in [179] or textbooks e.g. [180–182].

4.2 Static characterization

The static properties of the fabricated devices such as light-current (LI) and voltage-current (IV) characteristics were evaluated, as well as spectral measurements[4].

Figures 4.8 and 4.9 shown selected results of the power output, measured using a broad-area detector, as function of the drive current for a range of temperatures. The lasers were uncoated one-section devices soldered onto a submount and contacted with needle probes. The performance is good but not record high if compared to other similar single mode lasers, but it shows that a good material quality is achieved.

Optical spectra for a SCOOP6_3 and a SCOOP5_10 component are shown in Fig. 4.10 for a couple of currents. Common to all the few QW devices is that the peak intensity does not increase above approximately 100 mA current (4 mm devices), but the spectrum just get broader, i.e. the extra power emitted from the device originate from additional modes appearing in the spectrum. If heating is used to explain the spectral shift seen in Fig. 4.10, the temperature is increased by 16°C (bandgap shift ~0.6nm/K) going from 100 to 200 mA or 50 to 100 mA for the long SCOOP6_3 or short SCOOP5_10. This also implies that better performance in the light-current characteristics could be obtained improving the heat sinking by mounting the devices p-side down.

A summary of the results from the static laser characterization is shown in Table 4.4.

The IV characteristics and differential resistance is shown in Fig.4.11. Part of the reduced resistance for the SCOOP6 wafers compared to the SCOOP5_10 wafer is due to a higher p-doping in the InGaAs layer that was grown at 580°C for SCOOP6 compared to 610°C for SCOOP5. Also, leakage current that might be present in the LOC structures due to a low barrier height from the Q(1.1) SCH to the doped layers, would also give rise to an apparent reduced resistance.

[4]Some of the measurements were done by Casper Angelo and David Larsson

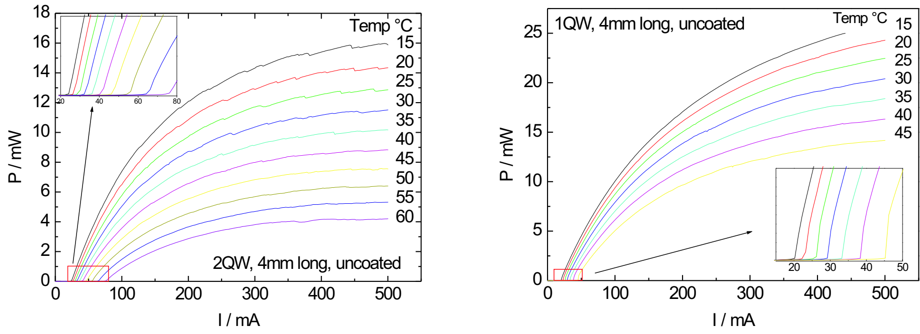

Figure 4.8: Light-current characteristics at different temperatures. *Left*: SCOOP6_2, 4 mm uncoated *Right*: SCOOP6_1, 4 mm uncoated

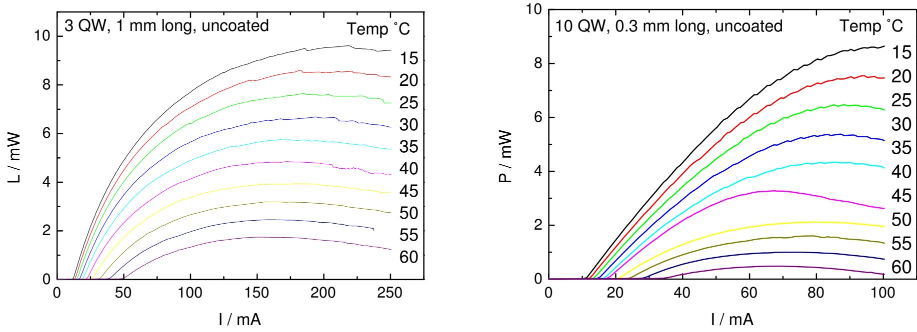

Figure 4.9: Light-current characteristics. *Left*: SCOOP6_3, 1mm. *Right*: SCOOP5_10, 300μm

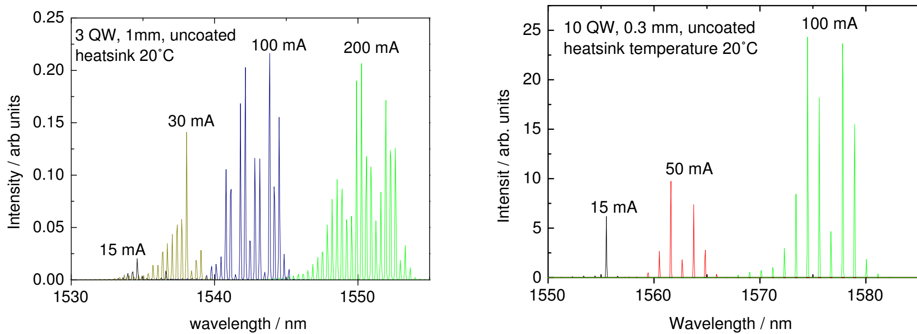

Figure 4.10: Optical spectra for uncoated chips. *Left*: SCOOP6_3, 1 mm. *Right*: SCOOP5_10, 300 μm

wafer, length	I_{th} / mA	P_{max} / mW	@ I_{max} / mA	λ @ I_{th} / nm
SCOOP6_1				
1 mm	17	6	150	1510
4 mm	16	20	500	1537
8 mm	28	22	500	
SCOOP6_2				
1 mm	14	6	200	1550
4 mm	26	5.5	500	1565
SCOOP6_3				
1 mm	16	9	200	1535
4 mm	33	16	500	1552
SCOOP5_10				
0.3 mm	13	8	100	1556
1 mm	29	14	300	1567

Table 4.4: Summery of lasing characteristics (20°C) for uncoated devices from different wafers. The quoted values are typical and shows general trends between the wafers but the exact values depends on the position on the wafer.

Amplified spontaneous emission (ASE) spectra from coated and angled devices were measured as shown in Fig. 4.12 at a current of 100 mA[5]. The ASE spectra becomes broader when the number of quantum wells is reduced, as would be expected from the increased bandfilling. The width of the 1 QW ASE spectrum is approximately 200 nm, but the magnitude of the ASE (∼Gain) is less than for the other devices.

The transparency current for the material was determined by injecting a modulated laser into a straight facet device and adjust the current to te point where no AC voltage (or current) is induced. The internal loss at transparency could then be determined by the Hakki-Paoli method [183]. In Table 4.5 the results are shown for two wavelengths[6].

4.3 RF mounting

In order to allow modulation at high frequencies and to provide heat sinking for the devices, a suitable mounting scheme must be devised. Microwave substrates with co-planar transmission lines and termination resisters were fabricated from AlN substrates prepared with resistance and gold layers. A few photolithography and wet etching steps are used to remove the gold

[5] Measurements by Lotte Jin Christiansen, who also processed the SCOOP6 batch.
[6] Measurements performed by L. J. Christiansen

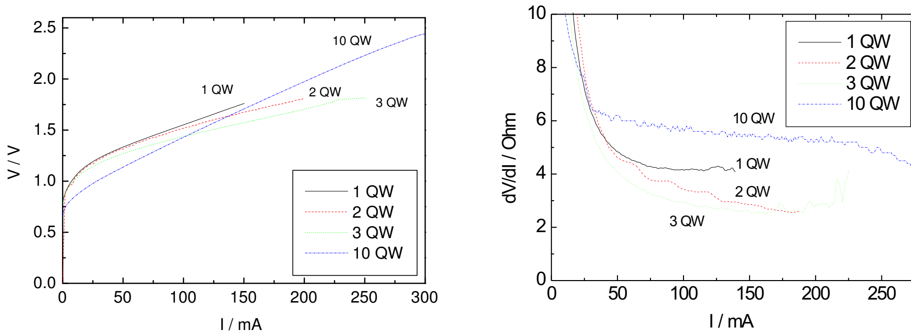

Figure 4.11: Current-voltage characteristics for 1 mm long and 2 μm wide components from the studied wafers. *Left*: Current versus voltage. *Right*: Differential resistance

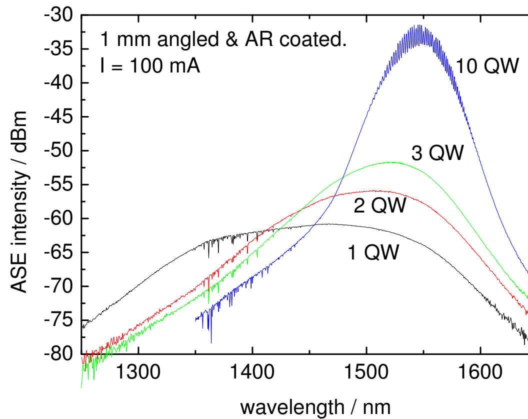

Figure 4.12: ASE spectra for 1 mm SOAs fabricated from the same materials as used for the MLLs

and resistance layers according to the design.

We use Au/Sn eutectic preforms for soldering the devices to the substrates and wedge bonding is used to ensure short bonding wires. The electrical transmission lines are contacted by "ground-signal-ground" probes or custom made "probes".

Microwave substrates for 40 GHz monolithic lasers and external cavity are shown in Fig.4.13. The gain modulation electrical waveguide can be terminated with a 40 Ω resistor in series with the device, while the reverse biased section can be terminated using a 50 Ω resistor in parallel. For most of the devices tested, the absorbers were not terminated, as it makes it more difficult to measure the absorber current. Also, during the development

	1QW		2QW		3QW		10QW	
Length/μm	1000	1000	1000	1000	1000	1000	500	500
1540 nm								
I_{tr}/mA	2.11	2.11	5	4.83	5.49	5.6	14.1	13.86
$J_{tr}/(A/cm^2)$	106	106	250	242	275	280	1410	1386
Loss $/cm^{-1}$	3.1	2.2	4.1	4.5	5.6	6.3	24	24.9
1550 nm								
I_{tr}/mA	1.83	1.79	4.21	4.3	4.47	4.79	12.26	11.98
$J_{tr}/(A/cm^2)$	92	90	211	215	224	240	1226	1198
Loss $/cm^{-1}$	2.7	1.6	3.8	3.8	5.2	5.7	18.7	22.9

Table 4.5: Measurements of transparency current (I_{tr}) and loss at transparency for different wafer designs. The transparency current density (J_{tr}) is simply scaled by the ridge area.

it is also desirable to be able to short all sections and test light-current characteristics for uniform injection into the whole device. On the other hand, terminating the absorber makes it easier to control the magnitude of the AC voltage applied when external modulation is used, since there are no standing wave effects. Also, not terminating the electrical waveguides sets increased demands to the driving circuitry as more power is reflected.

4.4 Dielectric coatings

For the AR coatings, two materials were chosen "TiO_s" with $s \approx 1.7$ and SiO_2, because they can be prepared with loss loss and have suitable refractive indices. Other materials for instance Ta_2O_5 and Al_2O_3 can also be used, but coatings made from these material require more accurate thickness control and give a slightly more narrow reflection bandwidth calculated using the theory of Chap. 5. The higher requirements is of course not a problem, if these materials can be deposited with higher accuracy and some labs prefer them.

The TiO_s is evaporated using an e-beam from pre-outgassed TiO_2 material bought as granulates. The advantage of using TiO_s instead of TiO_2 is that it does not change composition during heating and a homogeneous film can be obtained. The TiO_s is a black substance and it must be oxidized to obtain a low loss coating ($\sim TiO_2$). The refractive index and loss of the evaporated TiO_s is dependent on the substrate temperature, O_2 background pressure and deposition rate. Using 250 °C, 10 mPa O_2 and 1Å/s respectively we obtain reproducible thicknesses and indices and no measurable loss (by ellipsometry).

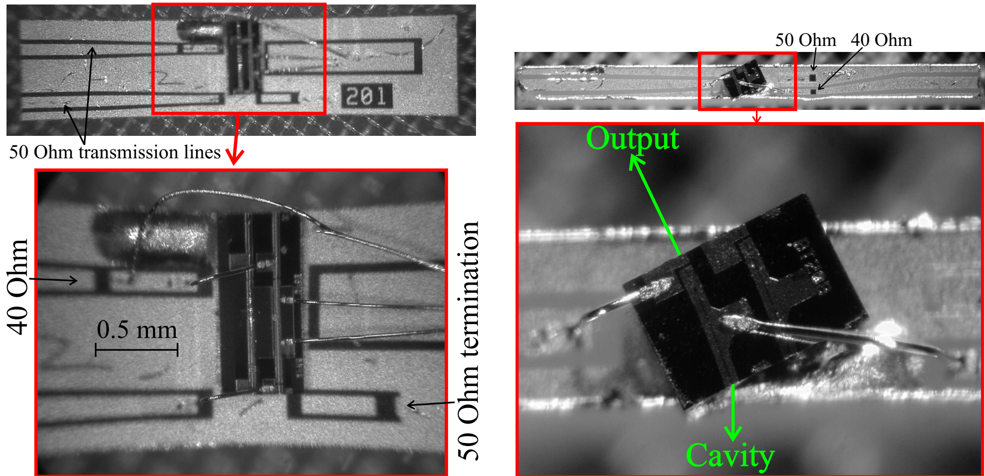

Figure 4.13: *Left*: Microwave substrate for 40 GHz monolithic mode-locked laser *Right*: Mounting for external cavity mode-locked laser (gain modulated).

SiO_2 does not decompose during evaporation and the refractive index is quite constant, regardless of the deposition conditions. It does not melt, but sublimes when heated, and this give problems since the e-beam tends to burn holes in the tablets used as starting material [184]. SiO_2 granulates can also be used, but for long evaporation times similar hole-burning problems occur. For AR coatings, where a single deposition is needed, a reasonable stable evaporation can be achieved by using a fresh tablet each time, but for high reflection (HR) coatings, where multiple SiO_2 layers are deposited, hole burning becomes a significant problem. The deposition rate for SiO_2 fluctuates a lot but, since the index is reasonable constant, the main concern is if hole-burning changes the evaporation cone. This will result in a changed ratio of deposition on the sample and monitoring crystal, i.e. tooling factor, and the thickness will be wrong. A low rate helps avoid excessive rate changes, but even with a rate of 2Å/s variations of many Å/s is seen.

The coating material parameters were calibrated by depositing layers of similar thickness as for the actual coatings on 30 mm×30 mm pieces of silicon wafer and use a variable angle spectroscopic ellipsometer (Wollam VASE) to evaluate the thickness and index. This could only be done from 450 nm–950 nm due to the used illumination and detector, so these data was then fitted to a Sell Meier or Cauchy ($n(\lambda) = A+B/\lambda^2+\cdots$) dispersion relation to get the values at 1.55 μm.[7] The refractive indices for SiO_2 and

[7]Most of these measurements were done by Thomas Jørgensen. See [185] for details.

TiO_s, using a two-term Cauchy disperion relation, are reported in Table 5.1.

The dispersion of SiO_2 is low, so the fitting works well, but it could be a problem for the TiO_s, that we are not able to measure at 1.55 μm.

The high deposition temperature for the TiO_s (which are also used for the SiO_2) makes in-situ monitoring of the modal reflection of the coating difficult. Ta_2O_5 can be deposited at room temperature with low loss, and the use of in-situ monitoring can be a reason for using other materials than TiO_s and SiO_2.

We evaluated the coating after deposition using the method described in appendix B.

4.4.1 Practical implementation

High- and antireflection coatings were deposited using the same vacuum chamber as that used for metal depositions. This is not an ideal solution as dielectrics and metals adhere badly to each other and flaking of the depositions on the chamber walls risk contaminating the coating materials. Crystals for thickness measurement needs to be changed each time a switch is made between metals and dielectrics as the risk of failure is large due to the bad adhesion. Also, no ion assist or optical thickness monitoring was employed as normally used for optical coating systems.

A 100 W heating element was constructed, thermally "isolated" from the rest of the chamber using ceramic materials and with as little dead space possible. This enabled a heating time to 250 °C of 10 min without excessive pressure rise due to outgassing.

Samples were cleaned 2–5 min in 0.9 Torr O_2 plasma at 100 W immediately before being placed in the vacuum chamber to remove organic residue on the facets. The chamber was then pumped down to approximately 200 μPa before starting the heating element.

After the deposition of a coating the heater is turned of and the chamber vented partially with N_2 to aid cooling. A slow cooling $\sim$30 min to 100 °C was used to help ensure that the film sticks to the sample.

Chapter 5

Optical thin film coatings

5.1 Anti-Reflection coatings

The most critical and difficult process step for external cavity mode-locked lasers is the antireflection (AR) coating applied to the facet facing the cavity. A maximum intensity reflection coefficient of 10^{-4} has been estimated for active mode-locking [186] and similar requirements has been found in this work.

The practical aspects are described in Chap. 4, while the coating design will be addressed in this chapter. Currently no commercial programs exist for coating design that goes beyond simple plane wave calculations, which is insufficient for very low reflection coatings on normal facets [187]. The deviation between plane wave theory and methods that take the mode into account of course becomes larger as the optical mode gets smaller. For a typical laser with an elliptical mode profile, this means that at least the direction perpendicular to the active layers have to be included in a calculation, but for accurate design both directions should be included [188]. In addition, angled facets are most often used when very low reflections are to be achieved and the angling is most simply done by slanting the waveguide in the photolithographic process, so also for this reason both directions needs to be included in the calculation.

As part of this thesis work a tool was created for coating design. To my knowledge no exact calculations exist for two-dimensional modes in semiconductor material, so a good benchmark to evaluate various approximations is not available. A number of authors have reported implementations of Fourier methods, where the mode-field is decomposed into its Fourier components and each of these are treated with the Fresnel reflection coefficients for uniform media [189–192]. I have chosen the slightly more accurate

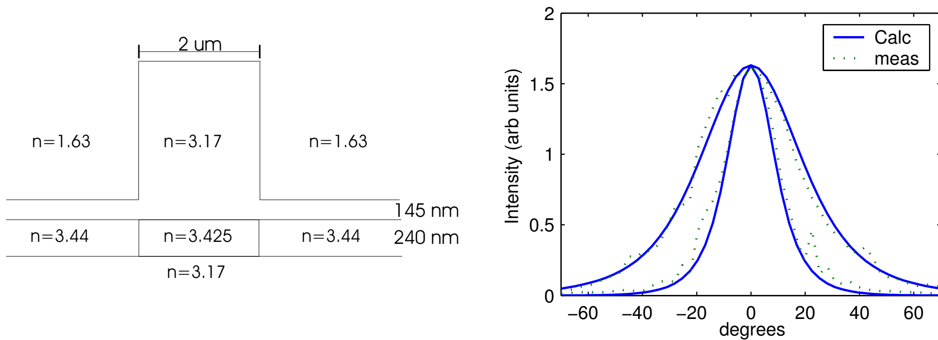

Figure 5.1: *Left*: Schematic of a simplified ridge waveguide structure showing how the carrier induced refractive index reduction is taken into account. Here the separate confinement region has been lumped in with the quantum wells, so the carrier induces index reduction is less than the -0.02 mentioned in the text. *Right*: Example of result of fitting procedure for an actual device (SCOOP5_10)

Free Space Radiation Mode (FSRM) method [193–195], as it only approximates the radiation modes. It should therefore be expected to be a little more correct, while still being fast, analytical and reasonable simple. The chosen implementation uses the full-vectorial two-dimensional mode-field as input and calculates the reflection through a matching of the tangential electric and magnetic field at the facet. The field at the interface is assumed to be composed of the forward and backward propagating modes and forward and backward propagating radiation fields. The assumption made in the calculation is that all the backward radiation modes propagate in "free space", i.e. a medium with a uniform refractive index. This assumption simplifies the calculations significantly and allows a non-iterative procedure to be used. However, it is also apparent that a waveguide with a large index contrast is not as well modelled as a low contrast waveguide. It has been shown that the FSRM assumption is valid for buried waveguides with 10% index difference [196], but for ridge waveguides no "exact" calculation exist, so that it is possible to compare. The theoretical assumptions, formulas and numerical implementation is documented in appendix A, whereas the results will be presented here.

5.1.1 Calculating the mode field

In order to design an optimized coating the mode field must be determined. This is normally done already during the design process, but a fine-tuning of the thicknesses and indices are often necessary to account for process

variations and estimated parameters. I have used a homemade effective index program for the actual design and verify and fine-tune the parameters using a slower, but more accurate commercial 2D finite element program *Selene*[1]. This program can calculate the vectorial field of the waveguide using a number of methods for instance *MultiGrid finite difference* and *Film Mode Matching*.

A discussion of the refractive index of bulk unstrained InGaAsP can be found in appendix C. However, the refractive index of the quantum wells show complicated dispersion and the refractive index of the wells and barriers are therefore used as a fitting parameter in the coating design process. The fitting is done between a measured[2] and calculated farfield for an uncoated lasing component. The FSRM method readily calculates the farfield from a mode exported from *Selene* and with a few iterations a good fit can be found. When laying out the index profile of the device, the carrier induced index reduction has to be taken into account in the quantum well region, where the carrier density is very high. Ideally, the diffusion of carriers sideways should be taken into account, but I have found that, to a good approximation, a square of the quantum wells and barriers with a reduction of -0.02 gives a good fit. The index reduction becomes increasingly important for the wider ridges (e.g. 3 μm) as it will be designed with a smaller index contrast to remain singlemode.

In Fig.5.1(right) a typical result of the fitting process is seen. The device is a 10 QW wafer (SCOOP5_10) and the index of the combined wells and barriers are estimated to be 3.47 (-0.02).

5.2 AR coating theoretical examples

In the following I shall show some examples of calculation, that can be performed, using the mode from SCOOP5_10 (Fig. 5.1 right). I only consider TE polarization, since the devices are emitters and compressive strained quantum wells are used for all the fabricated lasers. However, since the method is full-vectorial it would be simple to do the calculations on TM modes by simply using the corresponding field as input. Also, the implementation only allow a single guided mode, so the waveguides have to be designed single-mode. Extending to multi-mode waveguides is straightforward [194], but increases the complexity of the implementation.

The most important issue is to be able to design good AR coatings. For the calculations in this chapter, the material parameters in Table 5.1 have

[1] Now part of the Alcatel Optronics OlympIOs package

[2] The farfield was measured using a commercial Photon inc. goniometer

Material	refractive index @1.55μm
SiO_2	1.453
TiO_s	2.252
Si	3.18
Au	0.18-j10.21 [198]
Ti	4.04-j3.83 [198]
$Ag(approx)$	0.4-j12 [198]

Table 5.1: Material parameters

been used[3]:

5.2.1 Normal facet

In Fig. 5.2 a calculation of the modal reflection in dB at $\lambda_0 = 1550\ nm$ as function of the thicknesses of the coating layers is shown. The shown thickness ranges are $\frac{\lambda_0}{n_x 8} < d_x < \frac{\lambda_0}{n_x 4}$, where x is TiOs or SiO_2. If thicker layers had been included more optima would have been seen. These, however, have a more narrow reflection minimum, due to the thicker layers (the wavelength is more well defined) and will not be considered.

The asterisk in Fig. 5.2 and the following figures are the optimum coating using a simple plane-wave calculation based on the effective index of the mode (n_{eff}=3.220). The plane wave approximation is clearly not usable for a low reflection coating. In the present case, the reflection at the plane-wave optimum is approximately -26dB. However, the discrepancy will of course be smaller if a bigger mode is used, because it will resemble a plane wave more.

The minimum reflection point from Fig. 5.2 can be used as starting point for a numerical optimization of the coating. The result of such an optimization is shown in Fig. 5.3, where the reflection spectrum is plotted for an ideal coating. No dispersion of coating materials or mode is included, but it would only make a negligible difference.

As already used in the determination of the mode, the farfield and therefore also the transmitted power can easily be calculated with the FSRM code. To estimate the coupling to a tapered fibre, we calculate the overlap with a gaussian mode. In Fig. 5.3 (right) the coupling is plotted as function of the numerical aperture taken at the e^{-2} intensity point of the gaussian. The curve denoted *without reflection* is the overlap integral of

[3] The sign of the imaginary part has been chosen in accordance with [197] and an $\exp(i\omega t)$ time dependence

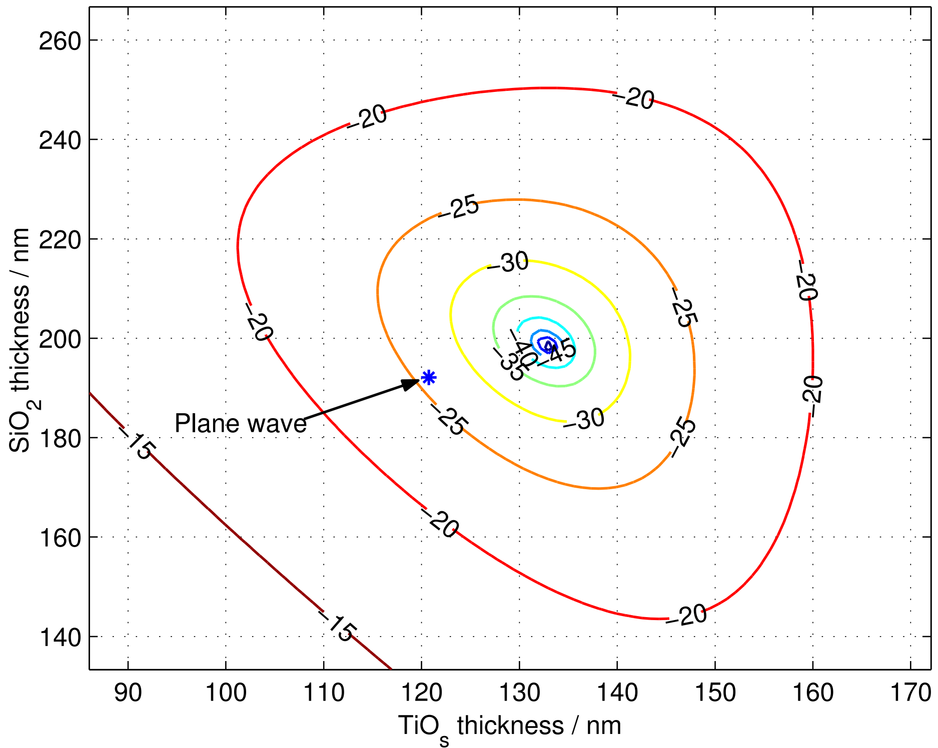

Figure 5.2: Modal reflection in dB as function of coating thicknesses for normal facet device

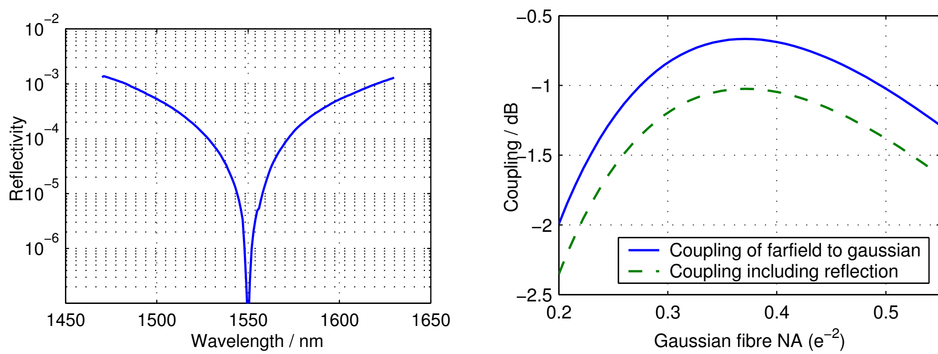

Figure 5.3: *Left*: Modal reflection as function of wavelength for optimal coating thicknesses: d_{TiOs} = 132.9 nm, d_{SiO_2} = 198.7 nm *Right*: Coupling to gaussian mode with and without reflection loss at coated facet

the farfield and the Gaussian, while the curve *with reflection* includes the residual reflection from the facet, which is 0.36dB in the present case. The optimum "external" coupling of -0.67dB (86%) is achieved using a $1/e^2$ NA of 0.371. The finite residual reflection for the perfectly coated facet exemplifies the fact that the simple plane-wave formulae $R + T = 1$ (for non-absorbing materials) does not hold for modes, and the difference is the power reflected into radiation modes. This reflection loss is unavoidable for small modes and bigger modes (possibly through mode-expanders) has to be used, if this loss term is to be reduced. It should be noted that a typical practical coupling loss is much higher, on the order of 3 dB. Another, important reason for using larger modes and therefore lower NA optics, is the increased alignment tolerances.

5.2.2 Angled facet

Angled facets are most often used when a low reflectivity is needed. A plane wave reflected at an angle on a dielectric interface would have zero back reflection in the direction it propagated to the interface (as it is reflected with the same angle on the other side of the interface normal). In contrast, a small mode will be composed of a full spectrum of plane waves and some of these will be reflected back into the mode. It is therefore apparent that the reduction in reflectivity obtained by angling the facet depends both on the mode size in the horizontal direction and the angle. Also, if more modes are present, mode-conversion will occur at the interface as the angle couples the otherwise orthogonal modes, and it is therefore important to use singlemode waveguides, when angled facet are used.

For the external cavity devices the maximum angle we can use is about 7°, which correspond to an external angle of $\sim 22^\circ$. Higher angles do not give room for the high NA and short focal length optics used in the cavity. In Fig. 5.4 the reflections vs. thicknesses are calculated for the same mode as in Fig. 5.2, but at a 7° angle. The reflection is seen to be approximately 15 dB lower a bit away from the optimum compared to the normal facet device. The optimum has moved closer to the plane-wave optimum, which is logical as contribution from the Fourier component normal to the coating becomes more important for the angled facet device.

The spectral dependence of the reflection for the optimum coating is calculated in Fig. 5.5 (left). The region of low reflection is very large and the coating outperforms the normal facet coating in this respect. However, looking at the coupling plot to the right side of Fig. 5.5, we see that the total coupling is reduced, due to a higher residual reflection into the radiation modes. In fact, the external coupling, i.e. mode-match, is slightly better

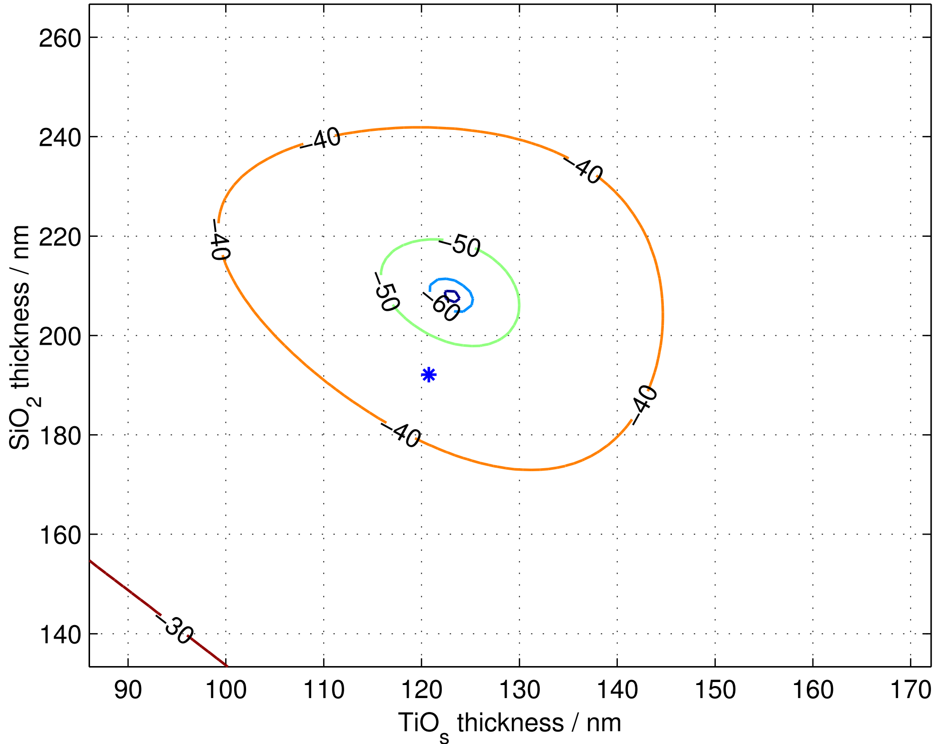

Figure 5.4: Modal reflection in dB as function of coating thicknesses for a 7° angled 2 μm waveguide

with a coupling of −0.58 dB (87%) using a 0.36 NA mode but the reflection loss has increased to 0.68 dB. This could be improved slightly by coating for maximum transmission instead of minimum reflection, but since the main limitation normally is the reflection, the numbers quoted here will be the effective ones.

As noted earlier a wider (single)mode waveguide should have a lower reflection and an example of this is shown in Fig. 5.6 (left). The mode used has been calculated for a 3 μm ridge waveguide with the same epitaxial structure as the previous examples, but with the etch stop layer moved "up" to ensure single mode behavior. The reflection is "sufficiently" low for all coating thicknesses, so optimization for transmission as shown in Fig. 5.6 (right) can be used.

The optimal transmission is found to occur for coating thicknesses of 124.1 nm and 216.3 nm and in Fig. 5.7 (left) the spectral reflectivity is shown for this coating. The spectral variation in both reflection and trans-

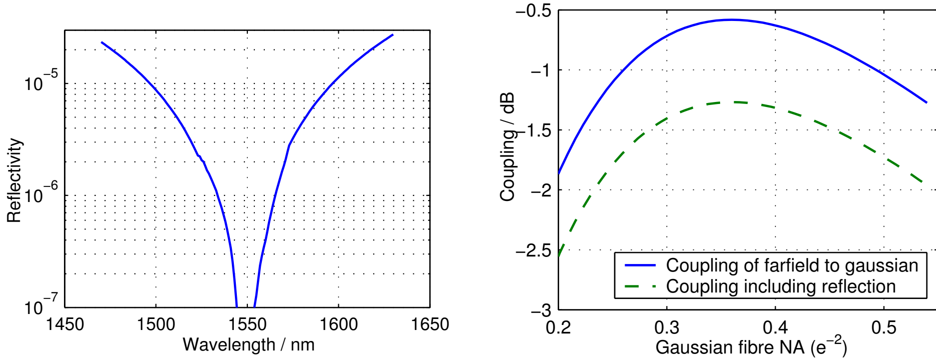

Figure 5.5: *Left*: Modal reflection for a 7° angled facet as function of wavelength for optimal coating thicknesses: $d_{TiOs} = 123.0$ nm, $d_{SiO_2} = 207.9$ nm. *Right*: Coupling to a gaussian mode with and without reflection loss at coated facet

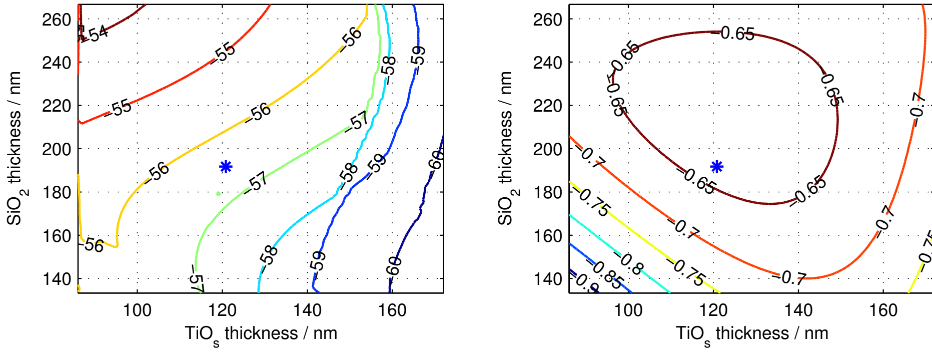

Figure 5.6: *Left*: Modal reflection in dB as function of coating thicknesses for 7° angled 3 μm wide waveguide. *Right*: Transmission for the same device

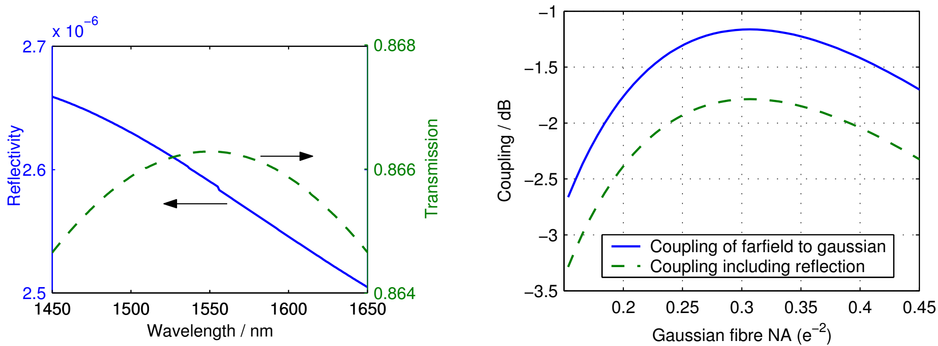

Figure 5.7: *Left*: Modal reflection for a 7° angled and 3 μm wide facet as function of wavelength for optimal coating thicknesses: $d_{TiOs} = 124.1$ nm, $d_{SiO_2} = 216.3$ nm. *Right*: Coupling to a gaussian mode with and without reflection loss at coated facet

mission is negligible small. The residual reflection is nearly the same as for the 2 μm waveguide, but the coupling to the symmetric fibre is worse by more than 0.5 dB, due to the astigmatic beam (cmp. Figs. 5.6 and 5.5). Recently, chiselled wedged fibres has been commercialized enabling good coupling to an elliptic mode. These could be good for high-power lasers and semiconductor optical amplifiers, where a broad waveguide also lowers the photon density. For external cavity lasers multiple cylindrical lenses might be used to shape the beam, but for the current work these options are not used and we aim for a symmetric mode, given that a sufficiently low reflectivity can be obtained.

5.2.3 Process tolerances

One advantage of the fast FSRM algorithm used is the possibility to make statistical estimates of the performance of a coating, if the uncertainties in the deposition parameters are known. This will also make it possible to compare different design approaches. If there were no process variations in the coating materials, a normal facet coating will be as good as an angled facet coating, without the added residual reflection penalty. Also, a 4-layer coating would always outperform a 2-layer coating. Thus, a tool is needed to quantify the performance of a real-life coating. For a two-layer coating, there are five uncertainties: The "mode parameters" and thicknesses and indices of the two coating materials. With this number of parameters, it might be possible to simply calculate the probability density function of the reflection, but a more general approach, that is also very easy to implement, is a monte-carlo calculation where random points in the distributions of the material parameters are chosen, and calculations are performed until the parameters of interest converges.

It should be noted that this kind of analysis is only valid if the parameters for the different layers are uncorrelated. In modern coating systems in-situ monitoring is used, so errors in the first deposited layers can be corrected in later layers, thereby making multi-layer coatings more feasible. Correlations between parameters, for instance less variation in optical thickness compared to variation in physical thickness, which could be expected due to a correspondence between packing density and index can of course be included in the simulations, if reliable parameters exist.

As an example of the calculations that can be done Fig. 5.8 shows the expected distribution of reflectivities for 5000 depositions using a "known mode" and gaussian distributed uncertainties for the coating materials. The uncertainties used in the left figure is estimated from calibration runs, while the higher thickness uncertainty of 4%, used in the right figure, is

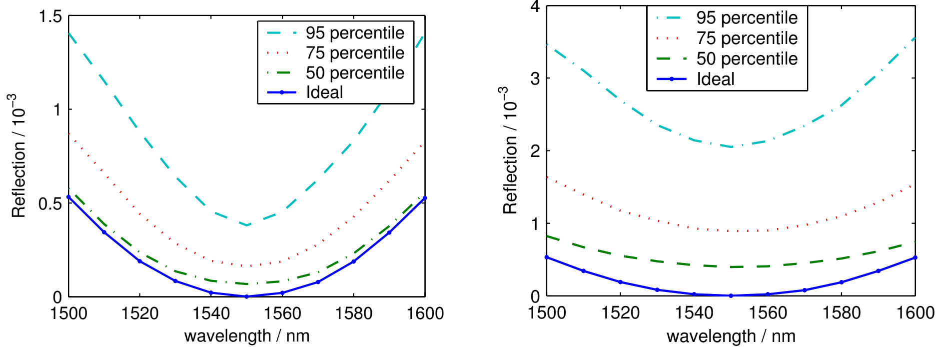

Figure 5.8: *Left*: Expected reflectivity distribution for gaussian distributed uncertainties: TiOs thickness standard deviation: 1.4%, index std. dev. 0.011, SiO2 thickness std. dev. 1.7% index std. dev. 0.004. *Right*: Same index uncertainties but a higher uncertainty of 4% for the thicknesses of the materials

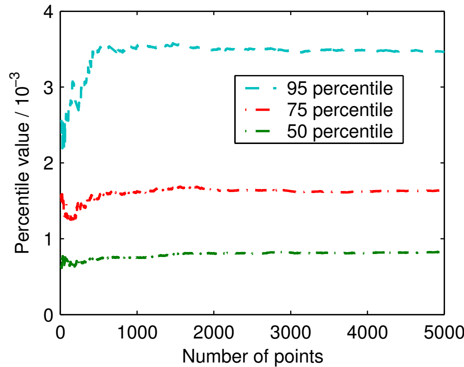

Figure 5.9: Convergence of the percentiles for increasing number of calculated points

quoted as a typical value in [184] and the resulting estimated reflectivities are more in line with the results obtained in practice.

The convergence is reasonable rapid as shown in Fig. 5.9 for the center wavelength of Fig. 5.8 (right). Using monte-carlo calculation we can now make a study of the expected performance of angled facet coatings. In Figs. 5.10 and 5.11 the statistics of 2000 "depositions" of a two-layer coating optimized for 1550 nm with gaussian distributed uncertainties with standard deviations of: TiOs thickness 4%, index 0.011, SiO_2 thickness 4%, index 0.004. The calculation is done for two wavelengths to give an impression of the bandwidth of the coating. We have chosen a waveguide angle of 7° for the fabricated devices corresponding to −51 dB and −44 dB for the 50th and 95th percentile of the depositions. As less than 50 dB

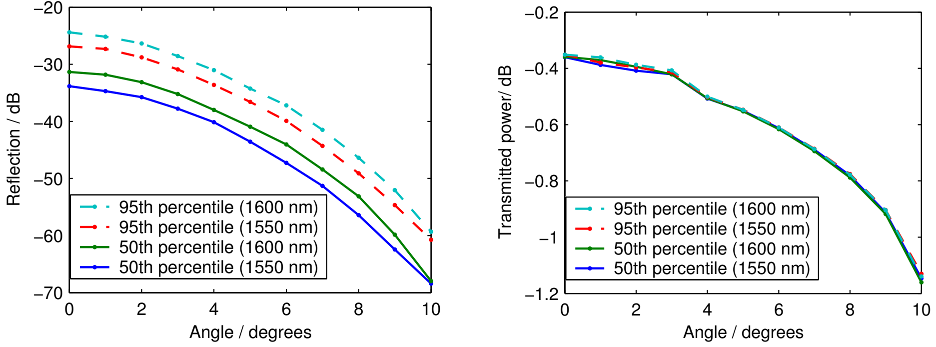

Figure 5.10: *Left*: Reflection as function of waveguide angle *Right*: Transmission

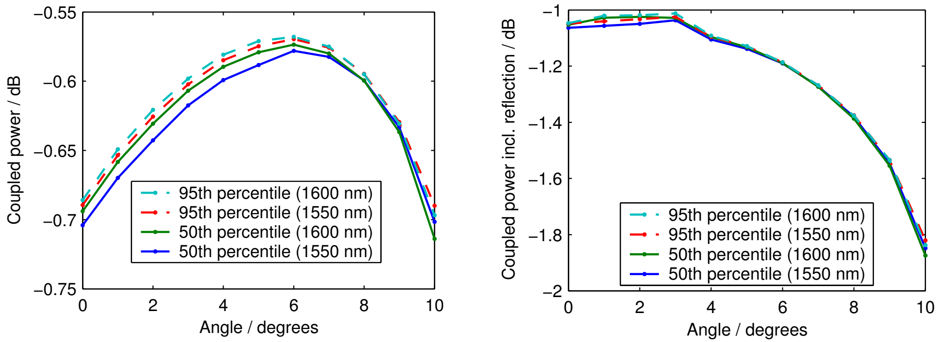

Figure 5.11: *Left*: Coupling of external field to gaussian fibre *Right*: Total coupling including reflection loss.

is desirable a good coating technology is still needed even for the angled devices.

As mentioned in Sec. 5.2.2, a wider waveguide can reduce the reflectivity of the facet. The reason we are not simply using a wide waveguide is, besides the increased astigmatism, that the goal is to make a short device with one end of the waveguide normal to the cleavage plane and the other at an angle (see Fig. 4.7). This means that the waveguide needs to be curved and the bend loss depends on the index contrast. Wider waveguides need a lower index contrast to stay single mode and accordingly, there is a trade-off between the angle at the facet and the width of the mode.

We have used a cosine shaped bend with a length of 293 μm and offset 23 μm corresponding to an angle of 7° at the facet. Assuming an index under the ridge of 3.225, the effective index next to ridge should be minimum 3.215 (3.210, 3.202) for a 3.0 μm (2.5, 2.0 μm) ridge and the excess

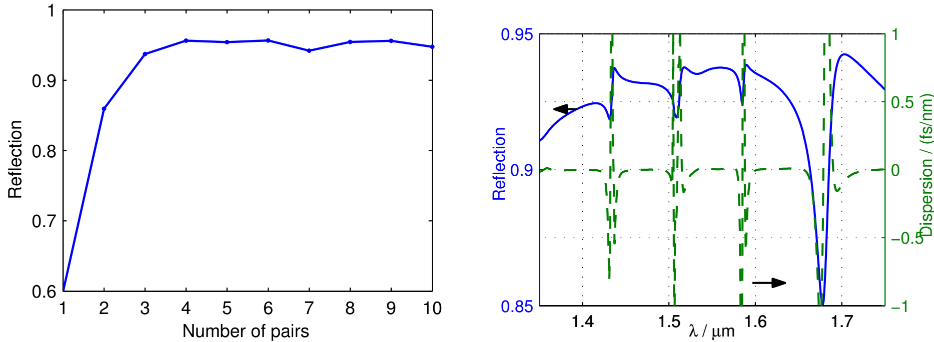

Figure 5.12: *Left*: Modal reflection at 1.55 μm vs. number of quarter–wave pairs (d_{Si} = 266.7 nm, d_{SiO_2} = 121.9 nm) with 121.9 nm SiO_2 on top. *Right*: Modal reflection as function of wavelength for 3 pairs and SiO_2 capping.

loss, calculated using a commercial beam propagation program is therefore 2.5 dB (0.6, 0.0 dB)[4], explaining the choice of a 2 μm wide ridge.

5.3 High-Reflection coatings

5.3.1 Dielectric coatings

Even though the coating theory was developed for the critical AR coatings, it can of cause also be used for high reflection coatings and some small differences are seen compared to plane-wave theory. In Fig. 5.12 (left) the reflections as function of the number of Si/SiO_2 quarter wave layer pairs are shown. Contrary to the corresponding plane wave result the reflection saturates after 4 pairs due to the divergence of the beam in the coating. For practical purposes however the value of 96% is sufficient, and it can be increased to about 98% by numerical optimization of the layer thicknesses. In Fig.5.12 (right) the reflection from a standard 3 pair high reflector is shown. For high reflectors the phase of the reflection might also be of interest and it is shown as the dispersion.

5.3.2 Metal coating

The dielectric HR coating takes many hours of deposition as a low rate of 2-3 Å/s has to be used for the SiO_2 to avoid hole-burning as mentioned in Sec. 4.4. In fact, most often the vacuum chamber has to be vented and new material inserted to complete a 3 pair coating with a SiO_2 capping. As

[4]BPM calculations using *Prometeous* by Svend Bischoff

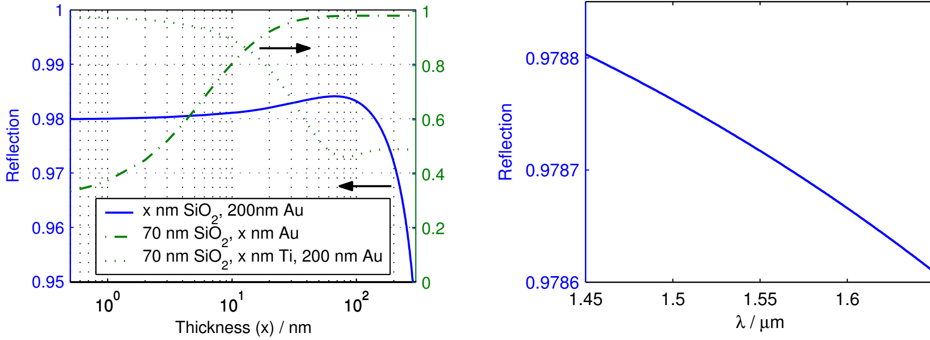

Figure 5.13: *Left*: Calculations of reflection from a metal coating varying the layer thicknesses as shown in the legend *Right*: Reflection spectrum from a 70nm SiO2, 1nm Ti, 100nm Au.

furthermore the devices are heated during the many hours of deposition, something easier would be desired. If it is possible to avoid shorting of the electrical connections through proper angling of the devices an option is to use metal coatings, e.g gold or silver. We have used a thin isolating layer of SiO_2 with 200 nm gold on top with good result. The calculation pertaining to the design of this coating is shown in Fig. 5.13 (left). It is seen that the coating is non-resonant and therefore very tolerant with respect to the thicknesses and hence easy to fabricate.

Gold is known to adhere badly to many surfaces, among those SiO_2. No long term reliability tests of the fabricated coatings have been done, but if reliability problems occurs, a thin (1–2 nm) Ti layer might be inserted for adhesion without seriously reducing the reflection ($\sim$ 97%) as shown in Fig. 5.13. Also, as it is an inner surface reflection, which is protected from oxidation, silver (97.8% reflection) can also be used with both cost and adhesion advantages.

The wavelength dependence for metal coatings is very small as shown in Fig. 5.13 (right) for a 70 nm SiO_2, 1 nm Ti and 100 nm Au coating.

5.4 Summary

In this chapter we have shown calculations on AR coating design using the free space radiation mode method. For the high-performing coatings needed for external cavity lasers simple plane-wave calculations will not be able to make a sufficient accurate design. We have also shown ways to estimate the influence of process variations, so that the an informed decision of for instance waveguide angle can be made.

Chapter 6

External cavity mode-locked laser results

The first reliable measurement of mode-locking was reported in 1978 by Ho et al. using an external cavity laser at 5 GHz (pulse-width ∼20 ps) [199]. Most of the initial mode-locking experiments were done by active mode-locking [104, 199–203] as this can be done using "standard" semiconductor lasers, but starting with the work of Ippen et al. in 1980 passive mode-locking (5 ps) was also achieved [204]. Since then many groups have reported external cavity mode-locking, and the work at UC Santa Barbara stand out, due to the many ideas that were analyzed and tested [205–207].

What the best results are is difficult to say, since many of the shortest reported pulses only have been measured with the autocorrelator and have had sharp peaks indicating complicated pulse shapes (see Sec. 2.2). However, the use in transmission systems or optical signal processing is the ultimate test and especially two groups have excelled here, i.e. HHI with 590 fs–14 ps transform limited pulses from 1–14 GHz at 1.44–1.56 μm using an implanted absorber [128, 208] and NEC with for instance 1.8 ps pulses at 10 GHz in the wavelength range 1530–1570 nm using a reverse biased absorber [135, 209].

For comparison few cycle pulses have been obtained at 100 MHz from Ti:Sapphire mode-locked lasers at ∼800 nm for instance 5.5 fs without pulse compression [210].

6.1 Experimental setup

A schematic of the external cavity mode-locked laser is shown in Fig. 1.1. The semiconductor chip consists of two sections, a short absorber section

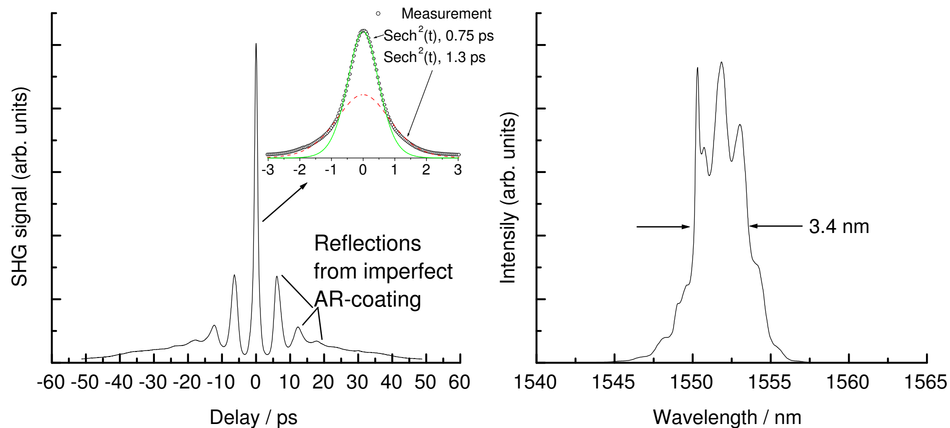

Figure 6.1: *Left*: Autocorrelation of a laser with 220 μm gain and 27 μm absorber section. Gain current 66 mA, absorber reverse bias 1.4 V, 20 m SMF, P_{out} ~0.04 mW. Grating 300 l/mm, 1.4 GHz. Inset: fit to center peak. *Right*: Optical spectrum

and a longer gain section separated by a 5 μm wide etch through the contact layers for electrical isolation. The end facet of the gain section is AR-coated with a two-layer TiO_2/SiO_2 coating and the light is coupled to an external cavity using a plano-convex 0.6 NA GRIN lens to collimate the light. The external cavity length can be varied to achieve repetition rates in the range of less than a GHz to just above 10 GHz. A grating is used for wavelength tuning and bandwidth control.

The lasers studied in this section have a straight 3 μm wide ridge, as was used in the first SCOOP generations. With both sections forward biased and in an external cavity the CW threshold is around 20 mA, which is a few mA above the value for the uncoated chip. With reverse bias applied, the lasers show hysteresis at mode-locking threshold, so all scans made in the following have been initiated in the mode-locking regime.

The output of the laser was analyzed using an optical power meter, autocorrelator (pulse amplified using an erbium doped fiber amplifier (EDFA)) and an optical spectrum analyzer.

For these lasers modulating the absorber section mainly affected the RF spectrum and not the pulse shape and only passive mode-locking results will be presented.

6.1.1 Chip length and AR coating

The key to short single pulse emission from external cavity mode-locked lasers is a very good AR coating [186] and these are quite difficult to fabri-

cate reproducibly. It is therefore interesting to investigate ways to minimize the sensitivity of the MLL to the coating. One way of achieving this, is by increasing the chip length [206, 207]. As an example we compare two lasers of nominally equal epitaxial structure, i.e. 10 compressive strained 8 nm quantum wells and similar AR coatings ($\sim 10^3$). First we show the output for a 250 μm long laser (SCOOP1_10, wafer G118) in Fig. 6.1. Very strong trailing pulses are seen in the autocorrelation trace with a delay corresponding to the roundtrip time in the laser chip, indicating the high residual reflectivity of the AR coating. These strong secondary pulses render this laser unusable for practical purposes, and furthermore increase the effective recovery time of the absorber, thereby making the absorber less efficient at higher repetition rates. The large tail in the autocorrelation trace can be attributed to a weak background and jitter broadening of the trailing pulses. In the optical spectrum the modulation corresponding to the chip-length is again visible, underlining the imperfect coating. Interpreting an autocorrelation as the one shown in Fig. 6.1 could be done numerically calculating an autocorrelation of a pulse with a number of trailing pulses and fit the heights of the latter. Here, we simply fit a sech^2 shape to the primary pulse, with and without a coherence peak and achieve a pulse width between 0.75 ps and 1.3 ps. Since the pulse is not sharp in the top, the actual pulse is probably closest to the 0.75 ps. The spectral width is 3.4 nm, giving a time-bandwidth product equal to the transform limit assuming a 0.75 ps pulse. The laser could therefore be expected to provide good mode-locking with the right coating.

Comparing the performance above with the device in Fig. 6.2, which is 600 μm long (SCOOP3_10, G245), we see that the trailing pulses are much smaller, but also that both the pulse and optical spectrum is broader. The explanation for the smaller trailing pulses can be inferred from Fig. 6.3 A) where the cavity averaged gain and loss dynamics are shown (cmp. Fig. 3.1). The absorber recovers faster than the gain and since the total net gain, at mode-locking threshold, of the main pulse will not change significantly with a longer gain section, the small fraction of the main pulse that is reflected at the coated facet will experience less net gain for a longer gain section. However, for a given epitaxial structure the longer gain section will be driven at a lower current density, which will increase the differential gain and result in an increased pulse broadening in the gain section. Also, jitter resulting from spontaneous emission will be increased with a longer gain section, so there is a tradeoff that will depend on the requirement for secondary pulse suppression and the capability (or yield) in the coating. The tradeoff can be avoided by using a curved waveguide with the absorber

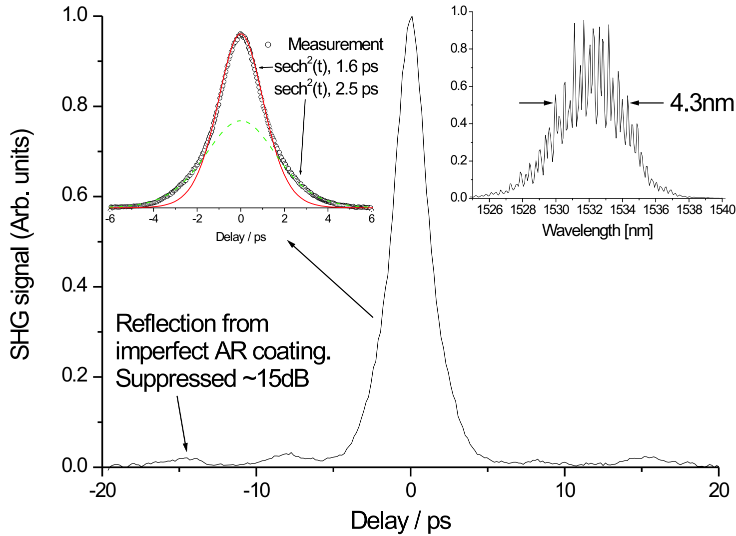

Figure 6.2: Autocorrelation measurement of 600 μm long laser with 570 μm gain, 26 μm absorber Gain current 70 mA, absorber reverse bias 1.8 V, compressed in 40 m SMF, P_{out} ~0.1 mW. Grating 150 l/mm. Passive mode-locking at 10 GHz.

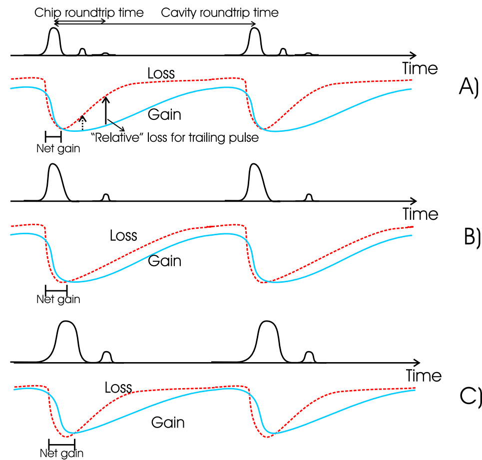

Figure 6.3: Roundtrip gain and loss as seen from the main pulse, see also Sec. 3.1. Trailing pulses will not experience the loss from the external cavity and the term *relative loss* is therefore used in the text. A) Trailing pulses for two chip lengths are shown. Dashed: short chip, solid: long chip. B) Reduced reverse bias compared to A) (longer recovery time). C) Increased gain current compared to A) (faster gain recovery)

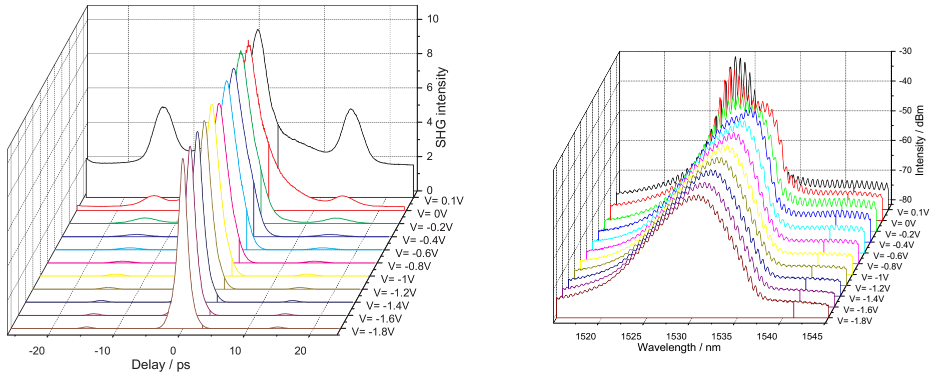

Figure 6.4: Gain current 60 mA, f_{rep} ≈5 GHz, 300 l/mm grating, passive mode-locking. *Left*: Autocorrelation measurements changing the reverse bias from -1.8 V (front) to 0.1 V (back). *Right*: Optical spectrum for the same measurement series series

normal to one facet and the coated gain section at an angle to the cleavage plane [211–213].

6.2 Driving conditions

Since both the current to the gain section as well as the reverse bias voltage on the absorber significantly influence the mode-locking properties, it is important to investigate and understand the optimum driving conditions[1]. In this section we report on systematic measurements of important parameters such as pulse width, time-bandwidth product (TBP) and trailing pulse suppression (TPS) of a particular laser. Key parameters of the laser (fabricated at HHI) include 6 compressively strained QWs, each 7 nm wide, a 550 μm gain section and a 50 μm absorber section. This device emits slightly shorter and less chirped pulses than the 600 μm device from the previous section consistent with the theory of Chap. 3. Due to previously experienced component failure for high absorber bias, the reverse voltage at the absorber section was kept below 1.8 V.

6.2.1 Absorber voltage dependence

In Fig. 6.4 autocorrelations and optical spectra are shown when changing the absorber bias from 0.1 to -1.8 V. A change in both the autocorrelation and optical spectrum is seen when the reverse bias is increased.

[1]These measurements were performed by Marcel Kroh from the Heinrich Hertz Institute (HHI) and I during my *COST267 Short term mission* to HHI in April 2000

In Fig. 6.5 parameters are extracted from the curves of Fig. 6.4 assuming a hyperbolic secant pulseshape, which gave the best fit to the autocorrelations. For a low reverse bias, the device looses mode-locking and the fit is not good, giving rise to the apparent decreasing time-bandwidth product. Both the pulsewidth, time-bandwidth product (TBP) and trailing pulse suppression (TPS) are seen to improve with increasing reverse bias, due to the faster recovery time of the absorber with increased reverse bias. The mechanism for pulse shortening and increased trailing pulse suppression with increased reverse bias is illustrated in Fig. 6.3 A) and B). Shorter absorber recovery time will narrow the window of net gain and also increase the relative loss for the trailing pulse. The TBP is improved due to two effects; a smaller pulse energy will reduce self phase modulation (SPM) in the gain section and the shorter pulse and higher reverse bias will increase SPM in the absorber, thereby counteracting the SPM of the gain section. The emitted pulses are dominated by SPM in the gain section, as is evident from the fact that they can be slightly compressed by transmission through short lengths of SMF [107].

Up to the chosen maximum the mode-locking properties improve with increasing reverse bias, and the laser should therefore be operated with this maximum reverse bias. Experience from other similar lasers show that the optimum lies around 1.8V, so the chosen limit might not change this conclusion. The maximum TPS of 20dB will suffice for some applications, but for high bitrate OTDM (160 Gbit/s) 30 dB is needed and this cannot be accomplished with the present coating.

6.2.2 Gain current dependence

Another important operating parameter is the gain current, and the output characteristics as function of gain current are shown in Fig. 6.6. As expected, the output power increases with increasing current, but so do the pulsewidth, TBP and magnitude of trailing pulses. With higher current the gain saturates more, due to the higher pulse energy and recovers faster. The faster recovery broadens the window of net gain and increases the gain for trailing pulses as depicted in Fig. 6.3 A) and C). The increased gain saturation therefore results in pulse broadening with enlarged SPM, i.e. chirp, as a result. The strongly reduced TPS is the major problem for the actual laser and it should be driven as close to mode-locking threshold as possible. A general problem for edge emitting mode-locked semiconductor lasers is the small pulse energy, but with the present lasers we are limited by the trailing pulses, and external amplification in erbium doped amplifiers should be used. The low pulse energy will increase the jitter, but

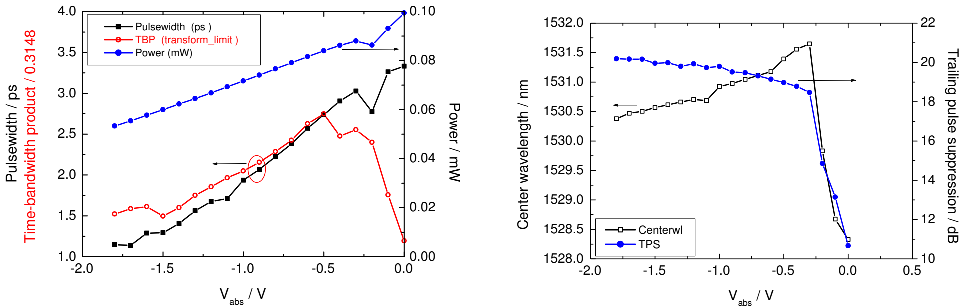

Figure 6.5: Absorber voltage variation for passive mode-locking of device from HHI. I_{gain}=60 mA, f=5 GHz, 300 l/mm grating, 18 m SMF (length not optimized). *Left*: Pulsewidth, time-bandwidth product (shown relative to transform limit for sech^2 shaped pulses: $\Delta t \cdot \Delta\nu = 0.3148$) and optical power. *Right*: Center wavelength and trailing pulse suppression.

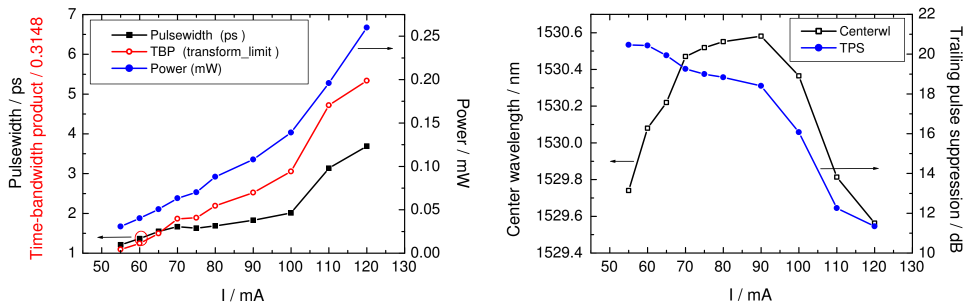

Figure 6.6: Gain current variation for passive mode-locking. V_{abs}=-1.8 V, f=5 GHz, 300 l/mm grating, 18 m SMF. *Left*: Pulsewidth, time-bandwidth product and optical power. *Right*: Center wavelength and trailing pulse suppression.

this has not been measured for the external cavity lasers.

6.2.3 Wavelength tuning

One of the advantages of the external cavity configuration is the wavelength tunability, and this is examined in figure 6.7. For this measurement series the cavity has been realigned between each measurement which can explain the fluctuating output power. Also, the current has been adjusted to the lowest value that gave stable mode-locking.

It is seen that the device has an optimum with respect to pulsewidth at 1530 nm, which also was the approximate lasing wavelength of the uncoated chip. The tuning range is limited by the trailing pulses (i.e. coating). The

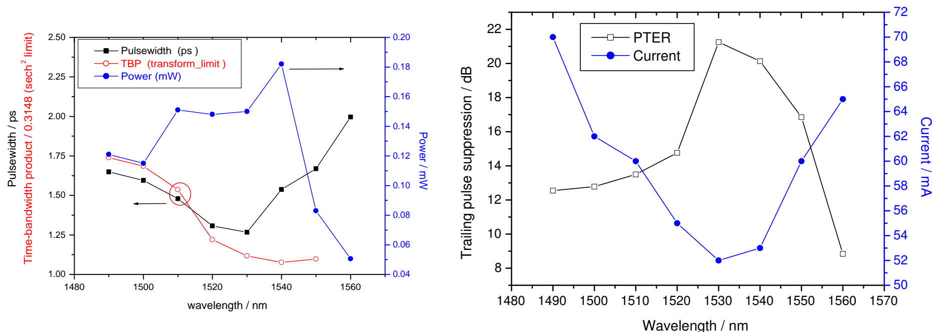

Figure 6.7: Wavelength tuning; V_{abs}=-1.8 V, f≈5 GHz, 300 l/mm grating, passive mode-locking *Left*: Pulsewidth, time-bandwidth product and optical power. *Right*: Operating current and trailing pulse suppression.

low TPS below 1530 nm is due to the noise floor of the autocorrelator which limits the measurement when EDFA amplification is not possible.

6.3 10 QW angled

The 10 QW angled lasers have been tested in the external cavity. A few mA increase in threshold is seen between an uncoated chip and a coated chip in a 150 l/mm grating cavity, and this is similar to the straight lasers indicating that the angle and curved waveguide does not introduce excess loss. The ASE ripple from the angled facet is low (<0.5 dB @ 40mA) indicating a low reflection, but until now no good mode-locking results have been achieved. The pulses narrows when the reverse bias is increased until 4-5 ps non-transform limited pulses are achieved at ∼-1 V. For higher reverse bias the device stops lasing. These problems are related to the high saturation energy of the absorber as discussed in Sec. 3.3.1 and means that it is not possible to increase the absorber bias enough to ensure a fast recovery.

Also, 3 QW long lasers have been tested in the external cavity, but no good results have been achieved yet.

6.4 Summary

External cavity mode-locked semiconductor lasers using a reverse biased section as saturable absorber can be used for short pulse generation. Here, 1.2 ps pulses at 5 GHz with a time-bandwidth product of 1.5 times the transform limit for sech^2 pulses was demonstrated, when the laser is driven

just above mode-locking threshold with a high reverse bias on the absorber section. The mode-locked pulses are, however, very sensitive to the quality of the antireflection coating and in the present case trailing pulses were only suppressed by around 20 dB. Improved coatings will also allow the use of shorter chips resulting in less chirp and thereby smaller time-bandwidth product. Other options, like curved waveguides or a different active area design to increase the saturation energy of the gain section have not yet shown the expected results.

Chapter 7

Monolithic mode-locked laser results

In this chapter monolithic lasers at 40 and 10 GHz are tested and compared to the previous work by other groups.

To quickly review the best work for 40 GHz lasers, Bell labs has done most of the initial work, and pulses around 1 ps were made by colliding pulse mode-locking [155, 214–217]. OKI entered the field early and have presented 12 nm tunable DBR mode-locked lasers [153, 218, 219], 800 MHz repetition rate tuning range [220] and impedance matched modulation circuit [124]. NEC, who has produced some of the best external cavity devices, has also made monolithic lasers, and they has analyzed and shown repetition rate tuning of 1 GHz at 40 GHz by changing the loss in a Bragg grating [143]. NTT has done much work in the field and has produced lasers with different gain and absorber sections and chirped DBRs and has analyzed the design of the different elements [95, 156–159]. Recently, HHI has entered the field with a DBR MML using both thermal and electrical tuning, and phase noise measurements [154, 221].

Since it resembles our design, work from 1991 using a single quantum well laser and four implantation runs to produce 5 ps pulses should also be mentioned [222].

At lower bit-rates, the first hybrid mode-locked laser was a 1.3 μm device at 15 GHz [223] and the same rate has been demonstrated at 1.55 μm [224]. A couple of groups have demonstrated ~10 GHz lasers [123, 136–143, 225], and a 5 GHz laser [226].

Apart from [222, 225], which appear coincidental, none of the authors of the many papers listed above have chosen to go down the design path outlined in Chap. 3. Arahira et al. [218] use 3 InGaAs QW, 4 nm wide and

are thus closest to our design, but the performance is worse and no jitter performance is reported. Morton et al. use an all-active structure for 15 GHz [223], but the active material is 250 nm 1.3 μm bulk material [227] and the threshold is high, so the jitter will most likely also be high.

Besides the hybrid mode-locked lasers presented above a number of very high rate (> 40 GHz) passively mode-locked lasers have been fabricated and tested. These will be needed for high-rate 3R regeneration where they can be injection locked. Most often some kind of colliding pulse mode-locking (CPM), either symmetric or asymmetric (ACPM), with the absorber placed a fraction of the total length away from the facet, is used to facilitate harmonic mode-locking to achieve a manageable device length. Examples include [228] for GaAs and [217, 229–233] for InP and as high as 860 GHz has been achieved. Another recent approach to achieve very high repetition rates is spectral filtering through a compound cavity effect [234, 235], and a repetition rate of up to 2.1 THz has been demonstrated.

A recent review (2000) of theory and experiments on monolithic mode-locked lasers was published in [129]

The monolithic devices were fabricated close to the end of the present Ph.D. project and have not yet been thoroughly characterized. The results should therefore be seen as proof of principle and evidence that the design principles presented in Chap. 3 indeed work. The results presented are, to my knowledge, better than current state of the art when the used criteria of combined high-power, low jitter and short pulse generation is concerned. Only few authors present high-frequency jitter, so a comparison must be based on the phase noise values at 10 MHz offset or similar.

7.1 Results on 40 GHz lasers

Devices from the SCOOP6 batch were cleaved to a length of 1070 μm, mounted on microwave substrates, and HR coated on the absorber facet using 3 periods of SiO_2/Si. The power output as function of injection current was measured using a broad-area detector as shown in Fig. 7.1. No termination resistor on the absorber was employed, so the sections could be connected together and the current injected uniformly into the whole device. The thresholds for the coated devices are 7, 8, and 10 mA for 1, 2, and 3 QWs. The efficiency is increased a lot compared to the results for uncoated lasers as reported in Table 4.4 and more than 20 mW output is achieved.

For mode-locking experiments the laser output was collected using a lensed isolator package (LIFI^{TM}) with ~3 dB coupling loss. A small part of

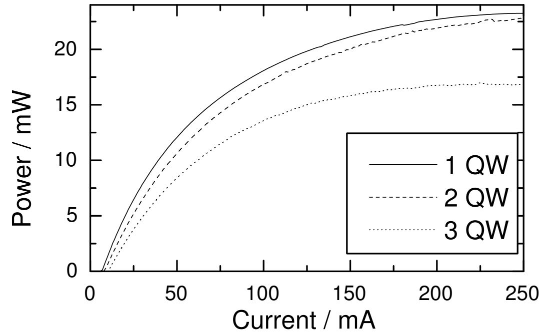

Figure 7.1: Light-current characteristics measured using broad-area detector for HR coated 1070 μm MMLLs.

the light was split off to a power meter while the rest was sent into an EDFA, after which the power was divided to the different measurement apparatuses. An Ando AQ6315E optical spectrum analyzer was used to measure the optical spectrum and a commercial autocorrelator, APE pulsecheck, with a 14 dBm EDFA preamplifier was used to measure the autocorrelation. Approximately 10 m optical fiber (SMF) and 2 fiber amplifiers were between the laser and autocorrelator in the measurement setup. The single sideband (SSB) phase noise on the 40 GHz carrier was measured using a HP8565E 50 GHz electrical spectrum analyzer with a >50 GHz photodiode (u^2t) directly connected to the input. A Labview program was made to collect and analyze the data. In order to speed up the measurement the resolution bandwidth of the spectrum analyzer was increased for large offset from the carrier. This on the other hand mask spurs that might be present in the data.

A HP70004A/70810A 22 GHz lightwave analyzer, i.e. a calibrated photodiode ESA combination, was used to measure the amplitude noise at baseband. Finally, a sampling oscilloscope with a 20 GHz photodiode was used to verify a sinusoidal signal, i.e. that the device was not Q-switching.

The 40 GHz lasers passive mode-lock well with short pulses, e.g. 3-4 ps pulses for a 2 QW device at 200 mA gain current and -4 V on the absorber.

7.1.1 Hybrid mode-locking

For the first hybrid mode-locking experiments a 40 GHz microwave synthesizer Rohde&Scwartz SMR40 was used. The output from the synthesizer was sent into a narrow-band power amplifier with an 1 dB saturation output

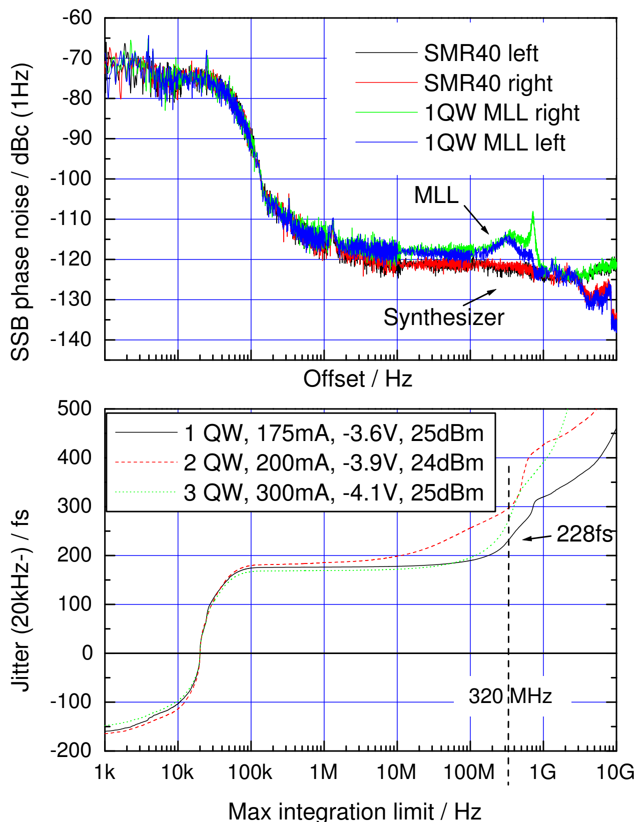

Figure 7.2: *Top*: Single sideband phase noise spectra of 1 QW 39.63 GHz MMLL and SMR40 synthesizer. *Bottom*: Integrated jitter from 20 kHz to the displayed integration limit. Legend: number of QWs, gain current, absorber bias, RF power

power (P1dB) of 27 dBm and an integrated bias tee (Cernex CNM39413027-01, Gain 30 dB, NF 11 dB). 40-GHz cables with approximately 2 dB loss were used to connect to a 50 GHz ground-signal-ground probe (GGB industries Picoprobe) that was contacting the microwave substrates.

The SSB phase noise for the 1 QW device driven at 175 mA gain current, -3.6 V on the absorber and 25 dBm RF power at the microwave probe is shown in the top graph of Fig. 7.2 along with a phase noise measurement of the synthesizer. It is seen that the jitter is dominated by the synthesizer up to 100 kHz, where the curves start to deviate, and that the noise floor is reached at around 1 GHz. In the bottom figure the integrated jitter is plotted assuming a lower integration limit of 20 kHz as discussed in Sec. 2.4.

The "negative" jitter part below 20 kHz is not mathematically correct[1], but has been included to aid readers who wish other integration ranges. It is important to remember that the jitter from different ranges should be added quadratically, i.e. if the jitter from the 1 QW device is desired in a 1 kHz to 320 MHz integration range the value would be approximately $\sqrt{160^2 + 228^2}$fs $\approx$ 280 fs.

The pulse autocorrelation and optical spectrum are shown in Fig.7.3. Both the pulse and spectrum are very smooth and fit well to a secant hyperbolic pulse and spectral shape. 2.8 ps pulses with a time-bandwidth product (TPB) of 0.4 is obtained indicating little chirp. The time bandwidth product is reduced to 1.2 times the transform limit 0.3148 by sending the pulse through additional 40 m SMF thereby compressing it to 2.5 ps which is sufficient for 160 Gbit/s systems. The fiber-coupled output power of 7.2 mW is, to my knowledge, record high for $<$ 3ps pulses from monolithic 40 GHz monolithic lasers, where the typical power level is a few mW. The total power out is around 14 mW and the mode is reasonable circular, so with optimized coupling optics it should be possible to get above 10 mW.

The jitter for the 2 and 3 QW devices is quite similar to the 1 QW device and strongly dominated by the synthesizer. The operating conditions and pulse characteristics are listed in Fig. 7.2 and Table 7.1. The pulses are longer and more chirped when the number of quantum wells are increased, in accordance with the predictions in Chap. 3.

The peak in the 1 QW SSB trace around 300 MHz contributes significantly to the jitter and is believed to originate from material resonances similar to relaxation oscillations. It is a little larger for the 2 and 3 QW components compared to the single quantum well, which is why the jitter is lowest for the latter.

It is evident that the measurement of jitter is complicated by the noisy synthesizer and limited dynamic range in the SSB measurement. However, the low white noise plateau of -118 dBc(1 Hz) from 1 MHz to 100 MHz and the low integrated jitter of 228 fs (20 kHz–320 MHz) is a significant result in itself.

An attempt was made to measure the RIN of the 1 QW device by injecting up to 3 dBm into the lightwave analyzer, but with the operating conditions used the displayed value was -154 dB/Hz which is equivalent to the measurement noise floor originating from thermal noise and shot noise.

The pulse extinction ratio is better than 23 dB, limited by the autocorrelation measurement. Since there is no spurious reflection etc. in the

[1] Calculated as $\sigma_J = -\frac{T}{2\pi}\sqrt{\left|\int_{-f_{high}}^{-f_{low}} L_{lsb}(f)df + \int_{f_{low}}^{f_{high}} L_{usb}(f)df\right|}$ instead of Eq.2.11

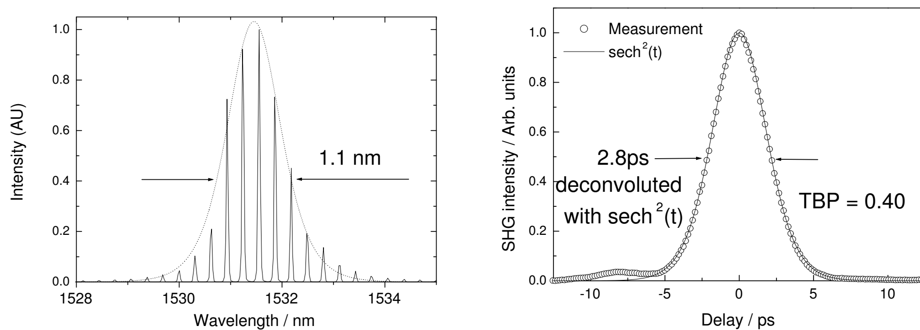

Figure 7.3: Pulse characteristics for 1 QW MMLL. *Left*: Optical spectrum with a $\text{sech}^2(f)$ fit *Right*: Autocorrelation and fit. TBP: Time-bandwidth product.

#QW	L_{abs} μm	V_{gain} V	I_{abs} mA	f_{rep} GHz	Δt ps	$\Delta t \Delta \nu$	λ nm	P_{out} mW
1	60	1.47	5.95	39.63	2.8	0.40	1531	7.2
2	55	1.50	-3.90	39.46	4.5	0.39	1556	9.0
3	50	1.72	11.3	39.49	4.9	0.66	1574	?*

Table 7.1: Summary of the 3 devices investigated, for the operating conditions in Fig. 7.2. *: Value not recorded but the power was similar to the other components. EDFAs were not used for the 3 QW device.

cavity and the power is quite high it would be expected that the extinction ratio is very high. A stronger amplifier before the autocorrelator or an autocorrelator with variable integration time could be used to measure this.

7.1.2 Low-noise synthesizer

The SMR40 synthesizer contributes 170 fs jitter from 20 kHz to 100 kHz and this part can be reduced by using a better synthesizer. In Fig. 7.4 the phase noise curves for the SMR40 used above and an Agilent PSG E8247C with an "ultralow phase noise" option is compared. The SMR40 is much worse than the PSG synthesizer op to ~100 kHz, but it also turns out that it does not reach the noise floor until 1 GHz, while the PSG synthesizer reach the floor at 10 MHz offset. The jitter of the PSG synthesizer is 54 fs (20 kHz–320 MHz) but as seen from the SSB trace this includes a small part of the noise floor.

Driving the 1 QW laser with ~25 dBm from the PSG synthesizer, and operating conditions: Gain current 175 mA (gain voltage 1.46 V), ab-

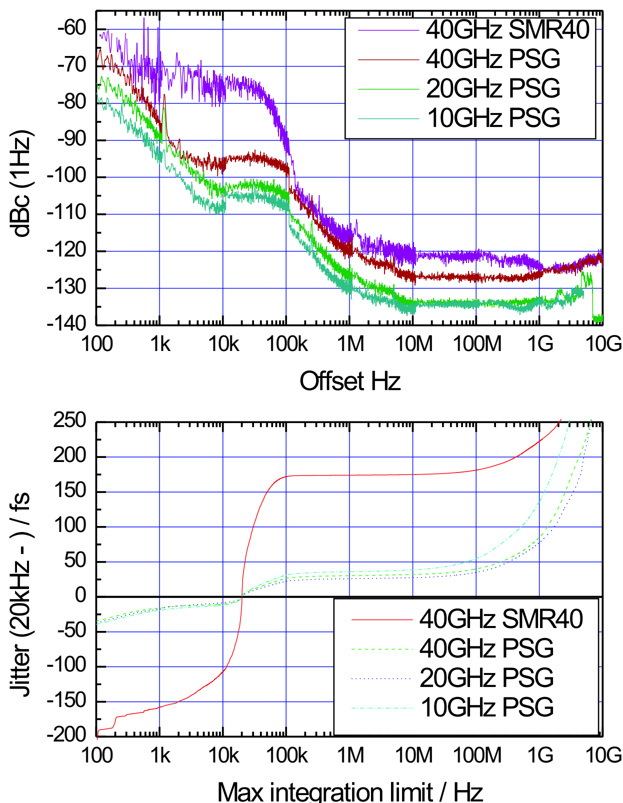

Figure 7.4: Comparison of phase noise (left sideband) and jitter for Rohde Schwartz SMR40 and Agilent PSG E8247C w/unj option

sorber voltage -2.77 V (absorber current 6.70 mA), we obtain the jitter performance shown in Fig.7.5, and the pulse shape and spectrum shown in Fig. 7.6. The fiber coupled power was 9.1 mW. The "ugly" optical spectrum could be filtered, and using a 3 nm FWHM tunable filter an almost transform limited pulse was obtained but the pulse width increased to more than 3 ps.

These measurements with the low-noise synthesizer were done approximately 1 month after the experiments reported with the SMR40 and the optimum jitter performance was not obtained for the same operating conditions. The reason for this is unknown, but for instance reflections from the coupling optics (even though there is an optical isolator) have been seen to have an effect of the performance. As an example, during the previous measurements, it was possible to switch between a nice transform limited

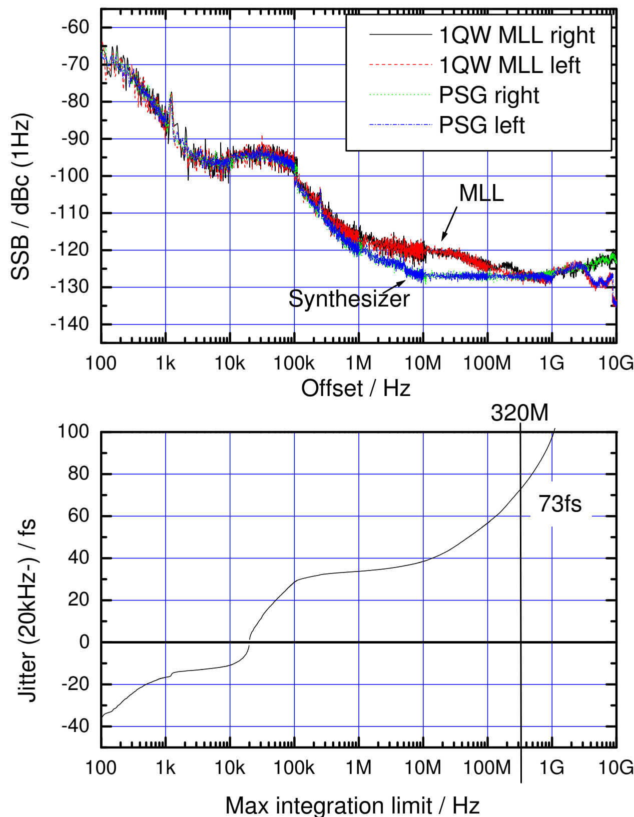

Figure 7.5: Phase noise and jitter from 1 QW device using PSG synthesizer at 39.77 GHz.

pulse as shown in Fig. 7.3 to a less nice pulse spectrum similar to Fig. 7.6 by moving the coupling optics.

The jitter performance is very good with an integrated jitter of 73 fs in the 20 kHz–320 MHz range and 81 fs in the 100 Hz–320 MHz range. These numbers are even upper limits as part of the data (100 MHz→) is so close to the noise floor that corrections should be applied to the data. An external mixer should be used to increase the dynamic range as discussed in section 2.4.

Known results from other groups are ∼300 fs (100 Hz–80 MHz) with ∼220 fs (10 MHz–80 MHz)[154] arising from a phase noise value of around -105 dBc(1 Hz) at 10 MHz offset [221]. Jitter of 0.41 ps (1 kHz–100 MHz) and RIN around -120 dB/Hz is reported in [220]. In [143] a jitter value of 0.2 ps is quoted but the integration range is not stated. The RIN, however,

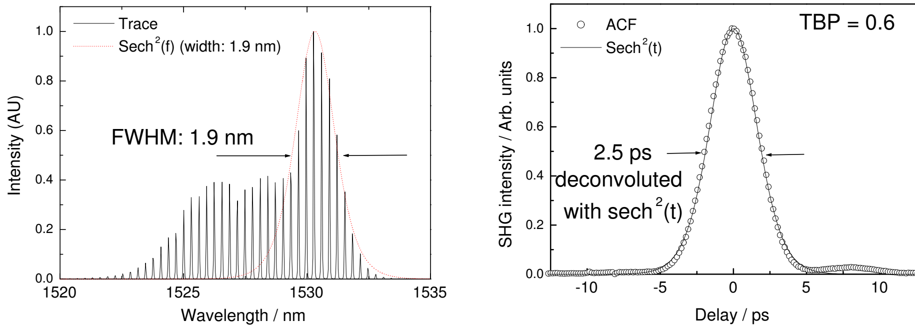

Figure 7.6: 39.77 GHz 1 QW device driven by PSG synthesizer. *Left*: Optical spectrum *Right*: Autocorrelation.

is around -140 dB/Hz which is much higher than our values, indicating that the integration range for the timing jitter is small. Phase noise values of almost -110 dBc (1Hz) at 1 MHz offset is inferred from an RF spectrum in [157], but this is still around 10 dB worse than what is reported here.

In summary the values reported here are significantly better than previously reported results.

7.2 Results on 10 GHz lasers

Devices from SCOOP6_1 and SCOOP6_2 were cleaved to a length of ~4260 μm and a SiO_2/Au HR coating was applied to the absorber facet. Light vs. current characteristic is shown in the dashed curve in Fig. 7.7 when the LIFI was used to collect the light. A threshold of 15 mA and a high fiber-coupled power of 23 mW at 500 mA is achieved.

The lasers were passive mode-locked, but the pulse widths were around 20 ps, which was not encouraging. Also, a couple of lasers died when they were mode-locked at 200-300 mA gain current, probably due to mirror damage. Expecting, both from theory and the 40 GHz experiments, that the gain current should be a few 100 mA to ensure a high inversion of the gain medium, I chose to apply a 5% AR coating composed of a single SiO_2 layer on the gain facet. This will lower the field strength at the output facet, but also increase the cavity loss and thereby the jitter.

7.2.1 Hybrid mode-locking

Only 2-QW lasers were still alive when I got access to an HP8673C RF synthesizer. In passive mode-locking the AR-coated lasers emitted ~20 ps

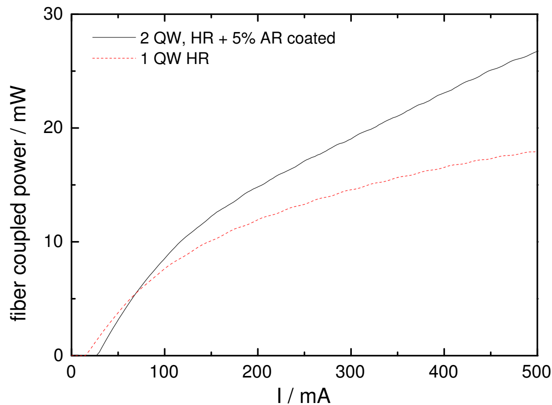

Figure 7.7: Fiber coupled power using LIFI as function of injection current.

pulses. The longest absorber was 55 μm and this component was used for hybrid mode-locking. Longer absorbers might have reduced the pulse width for passive mode-locked but this has not been tested yet.

The 22 GHz lightwave analyzer was used to evaluate the jitter and a 4-10 GHz electrical power amplifier (Cernex CBM04103030, gain: 30 dB, P1dB: 30 dBm, NF 6 dB) was used to boost the output from the synthesizer. A 3 dB attenuator was placed after the amplifier to protect it from reflections from the unterminated component. The hybrid mode-locking had a dramatic effect on the pulse width and in Fig. 7.8 the pulse is shown for operating conditions: RF power ~26 dBm, gain current 50 mA (gain voltage: 1.07 V) and absorber DC voltage -3.00 V (absorber DC current: -0.016 mA).[2] The fiber coupled output power was 1.56 mW. A 2.4 ps short pulse was produced, but the spectrum show much power at high energies giving a large time-bandwidth product. Part of the excess bandwidth is due to linear chirp as shown in the lower graph of Fig. 7.8, where propagation through 40 m SMF compresses the pulse to a low value of 1.4 ps. The absence of sharp features in the autocorrelation (coherence peak), indicates that it is possible to filter the optical spectrum with only limited pulse broadening penalty. A 1.4 ps transform limited sech^2 pulse has a spectral width of about 1.8 nm and this is shown in Fig. 7.8.

At larger currents the spectrum (and pulse) broadened significantly. The strong effect of the modulation tells us that most of the pulse shaping occurs in the modulation section, and the strength of the present design

[2] The low (and negative) absorber current is due to the large voltage swing, where the absorber is sent into forward bias part of the cycle.

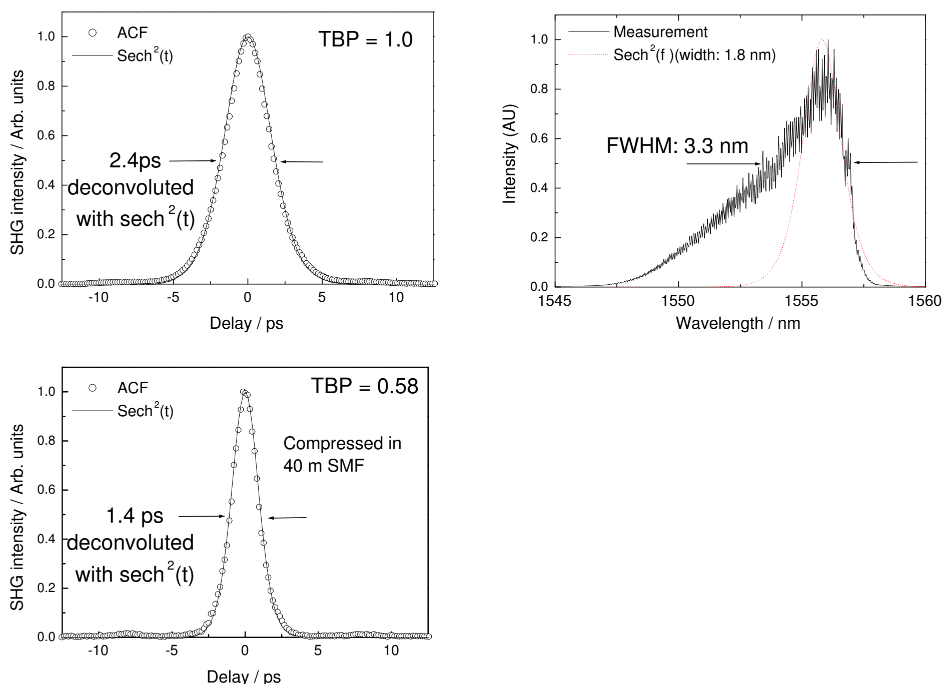

Figure 7.8: *Left*: Top graph shows pulse from a hybrid mode-locked 9.973 GHz laser "directly" (10 m SMF) from the laser. Bottom graph shown pulse compressed by additional 40 m SMF *Right*: Pulse optical spectrum.

related to the pulse shaping is that the long gain section does not broaden the pulse much, so that only a little shaping has to be done during each round trip.

The phase noise for the component is shown in Fig. 7.9. As seen for the 40 GHz lasers, the phase noise from the synthesizer and the component starts to depart around 100 kHz offset. The MLL shows a plateau at around −125 dBc before it falls off and reaches the noise floor around 300 MHz. Even though the lower level of the synthesizer might indicate a noise floor 10 dB lower, this is not the case. The mixer compression is given by the total input power and with a system bandwidth of 22 GHz the second harmonic at 20 GHz from the pulse train lowers the total power that can be injected into the system. A low pass filter after the photodiode could increase the dynamic range, but this would imply altering a calibrated system.

A timing jitter of 110 fs (20 kHz–80 MHz) is calculated from the noise bands. Not many reliable jitter values are quoted for low-repetition rate

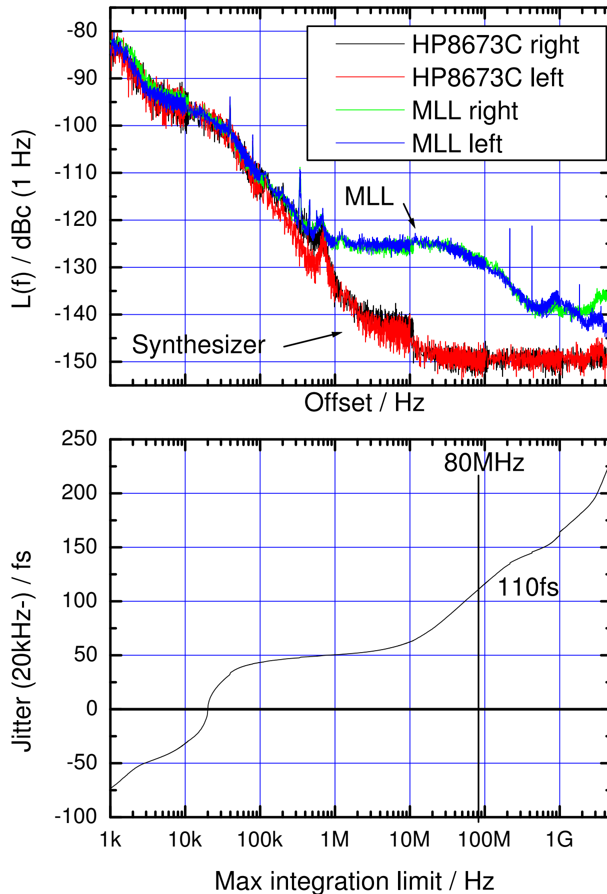

Figure 7.9: Phase noise and jitter performance of a 2 QW MMLL at 9.973GHz

monolithic lasers. An exception is [123], which shows phase noise curves to 1.5 GHz and calculate an absolute timing jitter of 420 fs (1 kHz–1.5 GHz). The corresponding value for our lasers is ∼190 fs resulting from an almost 10 dB lower SSB "plateau". A value of 0.3 ps is quoted in [143]. The integration range is not stated, but the range 100 Hz–10 MHz has previously been used by the same authors. Reference [122] shows residual timing jitter (i.e. using the phase detector method of Sec. 2.4) of 530 fs (150 Hz–50 MHz) for a 5.5 GHz laser.

For external cavity lasers at 10 GHz several absolute jitter values are reported. Less than 0.5 ps (100 Hz–10 MHz) [209], 300 fs (100 Hz–10 MHz) [128] and 250 fs (150 Hz–50 MHz) [206]. Using the phase detector method

(see Sec. 2.4) and an extremely good microwave oscillator, a value of 86 fs (10 Hz–4.5 GHz) has been obtained for 6.7 ps pulses [88], but in fact their "plateau" is just above the -125 dBc of Fig. 7.9 so part of the apparently better result is due to the improved measuring method. Also, using the phase detector method a timing jitter of 43 fs (10 Hz–10 MHz) or 121 fs (10 Hz–4.5 GHz) is reported from a harmonic mode-locked laser [89], but here the low noise is due to the harmonic mode-locking, see discussion below.

Summarizing the 10 GHz results, there are a few external cavity results that have better jitter performance that the 10 GHz laser presented here. Also, one of the regrown structures has shown pulses shorter (1 ps) [139], but does otherwise not show better performance. However, given the relatively easy fabrication process, with a single growth step, the value of the design principles is evident. In fact, the results presented have been for a 2 QW laser and the 1 QW laser should be expected to have less jitter and give less pulse distortion, but might require more electrical power to the absorber section due to the smaller confinement factor.

7.3 Discussion

Ever since the beginning of the 1990s it has long been taken as a fact that the jitter of monolithic lasers should be higher than that for external cavity lasers [122]. This has proven true for most of the results provided in literature to date, but if we apply the design principles outlined in this thesis this might not have to be the case. Looking at the loss only, we might compare two lasers: ECMLL: An external cavity laser of length 250 μm with a waveguide loss of 15 cm^{-1}, uncoated outcoupling facet and a reflection from the external cavity with an effective reflection coefficient of 0.3, i.e. approximately the same threshold for the uncoated chip and external cavity laser. MMLL: 4 mm all-active monolithic laser with a 100% HR coating, waveguide loss α and uncoated other facet. Setting the losses equal for the two lasers, one can show that the waveguide loss should satisfy: α <2.4 cm^{-1}. This is low but not unrealistic, as values as low as 1.3 cm^{-1} have been demonstrated for broad-waveguide lasers [146, 236]. At 40 GHz (length 1 mm) the waveguide loss should satisfy $\alpha < 9.7$ cm^{-1} which is easy to satisfy for the LOC structures used in this thesis. Regrown low-loss waveguides could possibly have lower loss but great care should be taken to avoid excess coupling loss between sections. A value of 90% as sometimes seen is equivalent to an extra distributed loss of 1 cm^{-1} for a 1 mm laser and 0.25 cm^{-1} for a 4 mm long device.

Besides the loss, the high power and high inversion of the gain medium indicate that the monolithic lasers should not be neglected for low-jitter applications.

Besides the design improvements discussed in Chap. 3 an additional route to reduced jitter might be available. A recent paper by Braun et al. [237] discusses the "universality of mode-locked jitter performance". They show that the jitter performance is characterized by a white noise plateau in the SSB trace with a characteristic "knee" after which the phase noise falls off. Their point, based on [238], is that longer cavities show this knee closer to the carrier and the jitter is therefore decreased using longer cavities. Deducing a knee position of approximately 100 MHz from the 10 GHz 2 QW SSB trace in Fig. 7.9, (top) our data actually fits very well with the data in [237]. The integrated jitter, however, of our lasers are much lower than that predicted from the paper due to the fact that the "white noise plateau" of our lasers are 15 dB below that of Braun et al. However, the two design routes might be combined and for high-rate lasers e.g. 160 GHz it might be an advantage to use harmonically mode-locked lasers also for this reason, but great care should be taken to avoid super-mode noise. Also, contrary to the external cavity and fibre-based lasers, the cavity loss and device length are not uncorrelated for monolithic lasers thus some tradeoff can be expected.

Finally, as mentioned previously in this thesis using the device as an optical VCO by introducing a phase section and synchronizing it using a fast phase locked feedback loop it is possible to suppress the jitter above the 100 kHz limit that simple modulation imposes. A version of this has been demonstrated using RF modulation of the absorber, a piezo controlled external cavity mirror and PLL control of the gain current to obtain 22 fs jitter (1 Hz–100 MHz) [239]. Beyond the bandwidth of the PLL the intrinsic jitter of the laser is however still dominating.

Chapter 8

Conclusion and outlook

8.1 Conclusion

In this thesis a new design of the epitaxial structure for mode-locked lasers was presented that have led to high-power short pulses with low jitter. The main point has been to concentrate on the gain material rather than the saturable absorber. By designing the gain material such that only limited pulse broadening occur during each pulse pass, the requirements to the absorber are strongly relaxed. Equally important, the fact that only limited pulse shaping has to be performed by the absorber lowers the loss when the device is mode-locked, so the gain, and therefore also spontaneous emission, can be kept low such that the jitter is reduced. The main design principles are low loss waveguides and a low confinement active material giving a high inversion and high saturation energy of the gain medium. This enables strong pulses, which reduces the effect of the spontaneous noise.

At 40 GHz, 7 mW fiber coupled 2.8-ps near-transform-limited pulses with 228 fs jitter (20 kHz–320 MHz) and 9 mW, 2.5-ps non-transform limited pulses with 73 fs jitter (20 kHz–320 MHz) were demonstrated.

At 10 GHz, 1.56 mW fiber coupled 2.4 ps (1.4 ps compressed in SMF) pulses with 110 fs jitter (20 kHz–80 MHz) were produced.

Measurements on external cavity lasers are also reported, but these lasers have proven very difficult to fabricate with good results. Part of the reason is the difficulty in making good AR coatings. The results from a comprehensive coating design model was presented.

8.2 Outlook

8.2.1 Monolithic lasers

Only few measurements have been performed on the monolithic lasers and much work remains to investigate pulse width, spectrum, jitter and power as function of the driving conditions. The gain section of the fabricated lasers is divided into 2–3 sections and the amount of repetition tuning accessible by varying the current to the different sections should be investigated. Also, the usability as optical VCO and the possibility to lower the jitter by both modulating the absorber and using PLL control of the gain current would be interesting to explore.

It is apparent from the measurements that a grating structure would be desirable in the components to ensure transform limited pulses and to filter the ASE noise, and a path for future component generations is outlined in Chap. 3. A component with different gain and absorption epitaxial structure combined with phase and DBR sections as designed in Sec. 3.4 could be expected to perform better than current state-of-the-art structures and presents a manufacturable structure using only three growth steps. This laser could be commercially interesting by itself and provide an excellent starting point for further integration with optical signal processing components.

A widely tunable version using a grating assisted coupler would be novel and very interesting, if it is possible to design the coupler with low loss. One drawback of this approach is the limited integrability compared to the Bragg mirror based component where the DBR can form the internal facet. However, with state-of-the-art etching technology it would be possible etch all the way through the waveguide to form a DBR with a sufficiently wide stopband for it not to be bandwidth limiting.

Also, a simple component with all-active epitaxial structure and a Bragg grating, might be possible to fabricate without butt-coupling the waveguides since the loss is low even in an un-pumped waveguide. The grating could be formed after growing the SCH or with good etching technology by etching from the top of the wafer. However, one should keep in mind an important design constraint when designing gratings for a mode-locked laser, namely a wide reflection bandwidth in order not to broaden the pulses too much. Thus, a large modal overlap or strong index contrast is needed.

It would also be interesting to perform dynamic modelling of the lasers using the new designs presented. Detailed modelling of the time evolution of the carrier distributions in energy and space would make it possible to estimate how large carrier reservoirs are needed to minimize the loss. Using

the epitaxial structure as amplifiers, 2R SOA/EA regenerator or in clock recovery configurations would also be very interesting.

8.2.2 External cavity lasers

The main problem with the external cavity devices are the limited manufacturability. However, using a slightly lower confinement factor than used in the previous designs for instance 8 QW, it should be possible to make lasers with absorbers >10 μm work. Curved devices with angled facets will be needed to ensure a reproducible low reflection as calculated in Chap. 5.

With a couple of lasers running a powerful application of the tunable mode-locked external cavity lasers is non-degenerate high-frequency pump-probe measurements, where two lasers are synchronized to the same microwave generator.

8.2.3 Coatings

When available it would be interesting to compare the calculations using the FSRM method with finite difference calculations of the reflectivity from a ridge waveguide structure with a large index contrast to determine the validity of the FSRM method.

The possibility of oxide overlayers on the (011) facet could be investigated and included in the calculations. Also, it would of course be nice to have a dedicated coating system with ion assist and in-situ monitoring to reduce the deposition uncertainties and to improve reliability.

Bibliography

[1] D. Breuer and K. Petermann. Comparison of NRZ- and RZ-modulation format for 40-Gb/s TDM standard-fiber systems. *IEEE Photonics Technology Letters*, 9(3):398–400, March 1997.

[2] Sang-Gyu Park, A.H. Gnauck, J.M. Wiesenfeld, and L.D. Garrett. 40-Gb/s transmission over multiple 120-km spans of conventional single-mode fiber using highly dispersed pulses. *IEEE Photonics Technology Letters*, 12(8):1085–1087, August 2000.

[3] Y. K. Chen, M. C. Wu, T. Tanbun-Ek, R. A. Logan, and M. A. Chin. Multicolor single-wavelength sources generated by a monolithic colliding pulse mode-locked quantum well laser. *IEEE Photonics Technology Letters*, 3(11):971–973, 1991.

[4] Wayne H. Knox. Ultrafast technology in telecommunications. *IEEE Journal on Selected Topics in Quantum Electronics*, 6(6):1273–1278, November/December 2000.

[5] Paul W. Juodawlkis, Jonathan C. Twichell, Gary E. Betts, Jeffrey J. Hargreaves, Richard D. Younger, Jeffrey L. Wasserman, Fredrick J. O'Donnell, Kevin G. Ray, and Richard C. Williamson. Optically sampled analog-to-digital converters. *IEEE Transactions on Microwave Theory and Techniques*, 49(10):1840–1853, October 2001.

[6] Rodney S. Tucker, Gadi Eisenstein, and Steven K. Korotky. Optical time-division multiplexing for very high bit-rate transmission. *Journal of Lightwave Technology*, 6(11):1734–1749, November 1988.

[7] Hidehiko Takara. High-speed optical time-division-multiplexed signal generation. *Optical and Quantum Electronics*, 32:795–810, 2001.

[8] M. Schilling, O. Blume, L.-H. Nguyen, M. Schmidt, and F. Lach. OTDM planar lightwave components (plcs) for multiplexing from 40 Gb/s to 80

- 640 Gb/s. *Lasers and Electro-Optics Society, 2002. LEOS 2002. The 15th Annual Meeting of the IEEE*, 2:887–888, 2002. ISSN 10928081.

[9] J. Hansryd, Andrekson P.A., and B. Bakhshi. A simple, low timing jitter sub-multiple clock recovery technique. In *ECOC Technical digest*, pages 471–472, Madrid, Spain, 1998.

[10] F. Zamkotsian, Kenji Sato, Hiroshi Okamoto, Kenji Kishi, Isamu Kotaka, Mitsuo Yamamoto, Yasuhiro Kondo, Hiroshi Yasaka, Yuzo Yoshikuni, and Kunishige Oe. Monolithic integration of MQW modulators on an optical multiplexer on InP for 100 Gb/s transmission. *Journal of Lightwave Technology*, 14(10):2344–2352, October 1996.

[11] R. Ludwig, U. Feiste, S. Diez, C. Schubert, C. Schmidt, H.J. Ehrke, and H.G. Weber. Unrepeatered 160 Gbit/s RZ single-channel transmission over 160km of standard fibre at 1.55 μm with hybrid MZI optical demultiplexer. *Electronics Letters*, 36(16):1405–1406, August 2000.

[12] T. Miyazaki, H. Sotobayashi, and W. Chujo. Synchronous optical demultiplexing and sampling of 80-Gb/s OTDM signals by optically recovered clock using mode-locked laser diode and symmetric Mach-Zehnder switch. *IEEE Photonics Technology Letters*, 14(12):1734–1736, December 2002.

[13] I. Shake, H. Takara, K. Uchiyama, I. Ogawa, T. Kitoh, T. Kitagawa, M. Okamoto, K. Magari, Y. Suzuki, and T. Morioka. 160 Gbit/s full OTDM demultiplexing based on FWM of SOA-array integrated on planar lightwave circuit. *ECOC technical digest*, 2:182–183 vol.2, 2001.

[14] K. Uchiyama, H. Takara, K. Mori, and T. Morioka. 160 Gbit/s all-optical time-division demultiplexing utilizing modified multiple-output OTDM demultiplexer (MOXIC). *Electronics Letters*, 38(20):1190–1191, 2002.

[15] E. Hilliger, J. Berger, H.G. Weber, K. Yvind, P.M.W. Skovgaard, and J. Hanberg. The cascaded amplifier and saturable absorber (CASA) all-optical switch. In *Photonics in Switching*, 2001. PThC.

[16] Ichiro Ogura, Yoichi Hashimoto, Hisakazu Kurita, Takanori Shimizu, and Hiroyuki Yokoyama. Picosecond all-optical gate using a saturable absorber in mode-locked laser diodes. *IEEE Photonics Technology Letters*, 10(4):603–605, April 1998.

[17] C. Knöll, M. Gölles, Z. Bakonyi, G. Onishchukov, and F. Lederer. Optimization of signal transmission by and in-line semiconductor optical amplifier-saturable absorber module. *Optics Communications*, 187: 141–153, 2001.

[18] Olivier Leclerc. Optical vs. eletronic in-line signal processing in optical communication systems: An exciting challenge for optical devices. In *Proceedings of ECIO*, pages 55–67, 2003.

[19] Patrick Bindel, Bruno Dany, Delphine Rouvillain, Bruna Lavigne, Patricia Guerber, Elodie Blamefrezol, and Olivier Leclerc. All-optical signal regenerators for ultra-high bit-rate transmission systems. *IEICE Trans. Electron.*, E85C(1):126–134, 2002.

[20] J. Leuthold. Signal regeneration and all-optical wavelength conversion. *Lasers and Electro-Optics Society, 2002. LEOS 2002. The 15th Annual Meeting of the IEEE*, 1:107–108 vol.1, 2002.

[21] Yuzo Yoshikuni. Semiconductor arrayed waveguide gratings for photonic integrated devices. *IEEE Journal on Selected Topics in Quantum Electronics*, 8(6):1102–1114, 2002.

[22] I.D. Phillips, A.D. Ellis, T Widdowson, D. Nesset, A.E. Kelly, and D. Trommer. 100 Gbit/s optical clock recovery using electrical phase-locked loop consisting of commercially available components. *Electronics Letters*, 36(7):650–652, 2000.

[23] L.K. Oxenløwe, A.I. Siahlo, K.S. Berg, A.T. Clausen, B.M. Sørensen, K. Yvind, P. Jeppesen, K.P. Hansen, K. Hoppe, and J. Hanberg. A novel 160 Gb/s receiver configuration including a glass crystal pulsed laser, photonic crystal fibre and a simple dynamic clock recovery scheme. In *ECOC proceedings*, Italy, 2003. Accepted for publication.

[24] M. Attygalle, H.F. Liu, and A. Nirmalathas. Robust all-optical harmonic clock signal generation through optical injection into passively mode-locked semiconductor lasers. *IEEE Photonics Technology Letters*, 13(9):1017–1019, September 2001.

[25] R. Ludwig, W. Pieper, E. Jahn, N. Agrawal, A. Ehrhardt, L. Küller, and H. G. Weber. 10 GHz all-optical clock recovery using a mode-locked semiconductor lasers in a 40 Gbit/s, 100 km transmission experiment. In *OFC Technical digest*, pages 132–133 / WH2, USA, 1996. OSA.

[26] H. Yokoyama, H. Kurita, T. Shimizu, and I. Ogura. Stabilization of ultrafast mode-locked diode lasers and its application for narrow-linewidth milimeter-wave sources. *Proceedings of SPIE - The International Society for Optical Engineering*, 3038:80–88, 1997.

[27] H. Yokoyama, Y. Hashimoto, H. Kurita, and I. Ogura. All-optical subharmonic clock recovery and demultiplexing. In *OFC Technical digest*, pages 232–234 / ThP5–1, USA, 2000. OSA.

[28] H. Yokoyama, Y. Hashimoto, H. Kurita, and I. Ogura. Two-stage all-optical subharmonic clock recovery using modelocked semiconductor lasers. *Electronics Letters*, 36(18):1577–1578, August 2000.

[29] C. Bornholdt, B. Sartorius, S. Schelhase, M. Möhrle, and S. Bauer. Self-pulsating DFB laser for all-optical clock recovery at 40Gbit/s. *Electronics Letters*, 36(4):327–328, February 2000.

[30] Laurent Chusseau and Christophe Kazmierski. Optimum linear pulse compression of a gain-switched 1.5 μm DFB laser. *IEEE Photonics Technology Letters*, 6(1):24–26, January 1994.

[31] Nobuhide Yamada, Nobukazu Banjo, Hiroshi Ohta, Seiji Nogiwa, and Yoshiki Yanagisawa. 320-Gb/s eye diagram measurement by optical sampling system using a passively mode-locked fiber laser. In *OFC Technical digest*, pages 531–532 / ThU3, USA, 2002. OSA.

[32] Masayuki Shirane, Yoichi Hashimoto, Hirohito Yamada, and Hiroyuki Yokoyama. A compact optical sampling measurement system using mode-locked laser-diode modules. *IEEE Photonics Technology Letters*, 12(11):1537–1539, November 2000.

[33] S. Kawanishi, H. Takara, K. Uchiyama, I. Shake, and K. Mori. 3 Tbit/s (160 Gbit/s*19ch) OTDM/WDM transmission experiment. In *OFC Technical digest*, pages PD1–1, San Diego, USA, 1999. OSA.

[34] M. Nakazawa, T. Yamamoto, and K. R. Tamura. 1.28Tbit/s-70km OTDM transmission using third- and fourth-order simultaneous dispersion compensation with a phase modulator. *Electronics Letters*, 36 (24):2027–2029, 2000.

[35] Masataka Nakazawa. Solitons for breaking barriers to terabit/second WDM and OTDM transmission in the next millennium. *IEEE Journal on Selected Topics in Quantum Electronics*, 6(6):1332–1343, 2000.

[36] L. Krainer, R. Paschotta, G. J. Spühler, I. Klimov, C. Y. Teisset, Weingarten, and U. Keller. Tunable picosecond pulse-generating laser with repetition rate exceeding 10 GHz. *Electronics Letters*, 38(5):225–227, 2002.

[37] G. J. Spühler, M. Dymott, I. Klimov, G. Luntz, L. Baraldi, I. Kilburn, P. Crosby, S. Thomas, O. Zehnder, C. Y. Teisset, M. Brownell, K. J. Weingarten, R. Dangel, B. J. Offrein, G. L. Bona, O. Buccafusca, Y. Kaneko, L. Krainer, R. Paschotta, and U. Keller. 40 GHz pulse generating source with less than 350 fs timing jitter. *Electronics Letters*, 38(18):1031–1032, 2002.

[38] J.B. Schlager, B. E. Callicoatt, R. P. Mirin, and N. A. Sanford. Passively mode-locked waveguide laser with low residual jitter. *IEEE Photonics Technology Letters*, 14(9):1351–1353, September 2002.

[39] S. Hoogland, S. Dhanjal, A.C. Tropper, J.S. Roberts, R. Haring, R. Paschotta, F. Morier-Genoud, and U. Keller. Passively mode-locked diode-pumped surface-emitting semiconductor laser. *IEEE Photonics Technology Letters*, 12(9):1135–1137, 2000. ISSN 10411135.

[40] R. Paschotta, R. Haring, A. Garnache, S. Hoogland, A.C. Tropper, and U. Keller. Soliton-like pulse-shaping mechanism in passively mode-locked surface-emitting semiconductor lasers. *Applied Physics B Lasers and Optics*, 75(4-5):445–451, 2002. ISSN 09462171.

[41] K. Jasim, Qiang Zhang, A.V. Nurmikke, A. Mooradian, G. Carey, Wonill Ha, and E. Ippen. Passively modelocked vertical extended cavity surface emitting diode laser. *Electronics Letters*, 39(4):373–375, 2003.

[42] A. Garnache, S. Hoogland, A.C. Tropper, I. Sagnes, G. Saint-Girons, and J. S. Roberts. Sub-500-fs soliton-like pulse in a passively mode-locked broadband surface-emitting laser with 100mW average output. *Applied Physics Letters*, 80(21):3892–3894, 2002.

[43] J. Yu, M. Schell, M. Schulze, and D. Bimberg. Fourier-limited 1.6-ps pulses with variable repetition rate from 1 to 26 GHz by passive mode-locking of a semiconductor laser in an external cavity. *IEEE Photonics Technology Letters*, 7(5):467–469, 1995.

[44] Y. Hashimoto, H. Yamada, R. Kuribayashi, and H. Yokoyama. 40-GHz tunable optical pulse generation from a highly-stable external-cavity mode-locked semiconductor laser module. In *OFC Proceedings*, pages 342–343, USA, 2002. OSA.

[45] M. Schell, D. Bimberg, and Kamiya. On the locking range of hybridly mode-locked semiconductor lasers. *IEEE Photonics Technology Letters*, 8(8):1004–106, 1996.

[46] B. Sartorius, M. Möhrle, and U. Feiste. 12–64 GHz continuous frequency tuning in self-pulsating 1.55-μm multiquantum-well DFB lasers. *IEEE Journal on Selected Topics in Quantum Electronics*, 1(2):535–538, June 1995.

[47] Martin Möhrle, Bernd Sartorius, Carsten Bornholdt, Stefan Bauer, Olaf Brox, Ariane Sigmund, Ralf Steingrüber, Mindaugas Radziunas, and Hans-Jürgen Wünsche. Detuned grating multisection-RW-DFB lasers for high-speed optical signal processing. *IEEE Journal on Selected Topics in Quantum Electronics*, 7(2):217–223, March/April 2001.

[48] S. Pitois, J. Fatome, and G. Millot. Generation of a 160-GHz transform-limited pedestal-free pulse train through multiwave mixing compression of a dual-frequency beat signal. *Optics Letters*, 27(19): 1729–1731, October 2002.

[49] M. Dulk, ST. Fischer, M. Bitter, M. Caraccia, W. Vogt, E. Gini, H. Melchior, W. Hunziker, A. Buxens, H.N. Poulsen, and A.T. Clausen. Ultrafast all-optical demultiplexer based on monolithic Mach-Zehnder interferometer with integrated semiconductor optical amplifiers. *Optical and Quantum Electronics*, 33(10):899–906, 2001. ISSN 03068919.

[50] Beck Mason, Abdallah Ougazzaden, Charles W. Lentz, Kenneth G. Glogovsky, C. Lewis Reynolds, George J. Przybylek, Ronald E. Leibenguth, Terry L. Kercher, John W. Boardman, Michael T. Rader, J. Michael Geary, Frank S. Walters, Larry J. Peticolas, Joseph M. Freund, S. N. George Chu, Andrei Sirenko, Ronald J. Jurchenko, Mark S. Hybertsen, Leonard J. P. Ketelsen, and Greg Raybon. 40-Gb/s tandem electroabsorption modulator. *IEEE Photonics Technology Letters*, 14 (1):27–29, January 2002.

[51] Hidekazu Kawanishi, Yoshinori Yamauchi, Naoyuki Mineo, Yoshiki Shibuya, Hitoshi Murai, Koji Yamada, and Hiroshi Wada. EAM-integrated DFB laser modules with more than 40-GHz bandwidth. *IEEE Photonics Technology Letters*, 13(9):954–956, september 2001.

[52] Hsu-Feng Chou, Ti-Jen Chio, and John E. Bowers. Standing-wave enhanced electroabsorption modulator for 40-GHz optical pulse generation. *IEEE Photonics Technology Letters*, 15(2):215–217, February 2003.

[53] G.8251 the control of jitter and wander within the optical transport network (otn). Recommendation G.8251, ITU-T, November 2001.

[54] Thorkild Franck (GiGA-Intel). Personal communication.

[55] Hidemi Tsuchida. Pulse timing stabilization of a mode-locked Cr:LiSAF laser. *Optics Letters*, 24(22):1641–1643, 1999.

[56] L.A. Buckman, J.B. Georges, J. Park, D. Vassilovski, J.M. Kahn, and K.Y. Lau. Stabilization of millimeter-wave frequencies from passively mode-locked semiconductor lasers using an optoelectronic phase-locked loop. *IEEE Photonics Technology Letters*, 5(10):1137–1140, 1993. ISSN 10411135.

[57] Y. Katagiri and A. Takada. Synchronised pulse-train generation from passively mode-locked semiconductor lasers by a phase-locked loop using optical modulation sidebands. *Electronics Letters*, 32(20):1892–1894, 1996. ISSN 00135194.

[58] E. Hashimoto, A. Takada, and Y. Katagiri. Synchronization of subterahertz optical pulse train from PLL-controlled colliding pulse mode-locked semiconductor laser. *Electronics Letters*, 34(6):580–582, 1998. ISSN 00135194.

[59] Mark J. W. Rodwell, David M. Bloom, and Kurt J. Weingarten. Subpicosecond laser timing stabilization. *IEEE Journal of Quantum Electronics*, 25(4):817–827, April 1989.

[60] A. T. Clausen, L. K. Oxenløwe, A. Siahlo, K. S. Berg, and P. Jeppesen. Pulsesource requirements for 160 Gbit/s, 640 Gbit/s and 1 Tbit/s transmission systems. Deliverable D3.1 IST-2000-28657, COM, Toprate, 2000.

[61] Peter Vasil'ev. *Ultrafast Diode Lasers: Fundamentals and applications.* Artech House, Massachusetts, USA, 1995.

[62] L.P. Barry, B.C. Thomson, J. M. Dudley, and Harvey J.D. Autocorrelation and ultrafast optical thresholding at 1.5 μm using a commercial InGaAsP 1.3 μm photodiode. *Electronics Letters*, 34(4):358–360, 1998.

[63] Kazuro Kikuchi. Highly sensitive interferometric autocorrelator in the optical communication band using Si avalanche photodiode as two-photon absorber. In *OFC technical digest*, pages 313–314 / ThN4, USA, 1998. OSA.

[64] C. Xu, J.M. Roth, W.H. Knox, and K. Bergman. Ultra-sensitive autocorrelation of 1.5 μm light with single photon counting silicon avalanche photodiode. *Electronics Letters*, 38(2):86–88, 2002.

[65] Mohammad M. Karkanehchi, David A. Barrow, Bryce A. Catrina, Hamilton Craig J., and John H. Marsh. The influence of single-photon absorption on the performance of the two-photon waveguide autocorrelator. *IEEE Journal of Quantum Electronics*, 33(6):933–937, 1997.

[66] Jeffrey M. Roth, Chris Xu, and T.E. Murphy. Ultrasensitive and high-dynamic-range two-photon absorption in a GaAs photomultiplier tube. *Optics Letters*, 27(23):2076–2078, 2002. ISSN 01469592.

[67] Joseph Mulet (COM/DTU). Simulations on external cavity mode-locked lasers. Unpublished.

[68] Svend Bischoff. *Modelling Colliding-Pulse Mode-Locked Semiconductor Lasers*. PhD thesis, Technical University of Denmark, Lyngby, Denmark, February 1997.

[69] E. P. Ippen and C. V. Shank. *Ultrashort Light Pulses, editor: S. L. Shapiro*, chapter Techniques for measurements, pages 83–122. Springer, New York, 1977.

[70] Prof. E. P. Ippen (MIT). Personal communication.

[71] F. Delorme, S. Slempkes, G. Alibert, B. Rose, and J. Brandon. Butt-jointed DBR laser with 15 nm tunability grown in three MOVPE steps. *Electronics Letters*, 31(15):1244–1245, 1995.

[72] Zuon-Min Chuang and Larry A. Coldren. Design of widely tunable semiconductor lasers using grating-assisted codirectional-coupler filters. *IEEE Journal of Quantum Electronics*, 29(4):1071–1080, 1993.

[73] R.C. I. Kim amd Alferness, U. Koren, L.L. Buhl, B. I. Miller, M. G. Young, M. D. Chien, T. L. Koch, H. M. Presby, G. Raybon, and C. A. Burrus. Broadly tunable vertical-coupler filtered tensile-strained InGaAs/InGaAsP multiple quantum well laser. *Applied Physics Letters*, 64(21):2764–2766, 1994.

[74] Jean-Claude Diels and Wolfgang Rudolph. *UltraShort Laser Pulse Phenomena: Fundamentals, techniques and applications on a femtosecond scale*. Academic Press, INC., San Diego, 1996.

[75] Govind P. Agrawal. *Nonlinear Fiber Optics.* Academic Press, Inc, San Diego, USA, 1989.

[76] Rick Trebino, Kenneth W. DeLong, David N. Fittinghoff, John N. Sweetser, Marco A. Krunbügel, and Bruce A. Rickman. Measuring ultrashort laser pulses in the time-frequency domain using frequency-resolved optical gating. *Review of Scientific Instruments*, 68(9):3277–3295, September 1997.

[77] Kenneth W. DeLong, David N. Fittinghoff, and Rick Trebino. Practical issues in ultrashort laser-pulse measurements using frequency-resolved optical gating. *IEEE Journal of Quantum Electronics*, 32(7): 1253–1263, July 1996.

[78] K. Ogawa, D. Kunimatsu, A. Suzuki, S. Arahira, Y. Kato, and Y. Ogawa. Pulse characterisation of a quantum-well mode-locked laser diode by two-photon absorption frequency-resolved optical gating. *Optical and Quantum Electronics*, 33:727–733, 2001.

[79] H.A. Haus and A. Mecozzi. Noise of mode-locked lasers. *Quantum Electronics, IEEE Journal of*, 29(3):983–996, 1993. ISSN 00189197.

[80] Leaf A. Jiang, Matthew E. Grein, Hermann A. Haus, and Erich P. Ippen. Noise of mode-locked semiconductor lasers. *IEEE Journal on Selected Topics in Quantum Electronics*, 7(2):159–167, March/April 2001.

[81] Kohichi R. Tamura and Kenji Sato. 50-GHz repetition-rate, 280-fs pulse generation at 100-mW average power from a mode-locked laser diode externally compressed in a pedestal-free pulse compressor. *Optics Letters*, 27(14):1268–1270, July 2002.

[82] Leaf A. Jiang, Matthew E. Grein, Hermann A. Haus, Erich P. Ippen, and Hiroyuki Yokoyama. Timing jitter eater for optical pulse trains. *Optics Letters*, 28(2):78–80, January 2003.

[83] M. Attygalle, A. Nirmalathas, and H. F. Liu. Novel technique for reduction of amplitude modulation of pulse trains genrated by subharmonics synchronous mode-locked laser. *IEEE Photonics Technology Letters*, 14(4):543–545, April 2002.

[84] Amnon Yariv. *Optical Electronics in Modern Communication.* Oxford University Press, USA, fifth edition, 1997.

[85] D. von der Linde. Characterization of the noise in continuously operating mode-locked lasers. *Applied Physics B*, 39:201–217, 1986.

[86] M. Jinno. Effects of crosstalk and timing jitter on all-optical time-division demultiplexing using a nonlinear fiber Sagnac interferometer switch. *Quantum Electronics, IEEE Journal of*, 30(12):2842–2853, 1994. ISSN 00189197.

[87] Ryan P. Scott, Carsten Langrock, and Brian H. Kolner. High-dynamic-range laser amplitude and phase noise measurement techniques. *IEEE Journal on Selected Topics in Quantum Electronics*, 7(4):641–655, 2001.

[88] Leaf A. Jiang, Matthew E. Grein, Erich P. Ippen, Cameron McNeilage, Jesse Searls, and Hiroyuki Yokoyama. Quantum-limited noise performance of a mode-locked laser diode. *Optics Letters*, 27(1):49–51, 2002.

[89] Christopher M. Depriest, Tolga Yilmaz, Alan Braun, Joe Abeles, and Peter J. Delfyett. High-quality photonic sampling streams from a semiconductor diode ring laser. *IEEE Journal of Quantum Electronics*, 38 (4):380–388, 2002.

[90] B. Peterson. Spectrum analysis. Application note AN-150, Agilent technologies, 1989.

[91] L.A. Jiang, S.T. Wong, M.E. Grein, E.P. Ippen, and H.A. Haus. Measuring timing jitter with optical cross correlations. *Quantum Electronics, IEEE Journal of*, 38(8):1047–1052, 2002. ISSN 00189197.

[92] T. Yilmaz, C. M. DePriest, and P. J. Delfyett. Measurement of residual phase noise in 10 GHz pulsetrain using modified Michelson optical frequency discriminator. *OSA topics*, 49:63–66, 2001.

[93] A. Wonfor, B. Zhu, I.H. White, and R.V. Penty. Low short term timing jitter in an integrated monolithic extended cavity semiconductor mode-locked laser. *Digest of the IEEE/LEOS Summer Topical Meetings*, pages 64–65, 1997.

[94] Anders Clausen (COM/DTU). Personal communication.

[95] Kenji Sato, Isamu Kotaka, Yasuhiro Kondo, and Mitsuo Yamamoto. Actively mode-locked strained-InGaAsP multiquantum-well lasers integrated with electroabsorption modulators and distributed bragg reflectors. *IEEE Journal on Selected Topics in Quantum Electronics*, 2(3): 557–565, September 1996.

[96] Mario Dagenais, Robert F. Leheny, and John Crow, editors. *Integrated Optoelectronics*. Academic Press, Inc, San Diego, USA, 1995.

[97] Herman A. Haus. A theory of forced mode locking. *IEEE Journal of Quantum Electronics*, QE–1(7):323–330, July 1975.

[98] J. P. van der Ziel. *Semiconductors and Semimetals*, volume 22B, chapter 1. Academic Press, Inc, New York, USA, 1985.

[99] New. Pulse evolution in mode-locked quasi-continuous lasers. *IEEE Journal of Quantum Electronics*, QE–10(2):115–124, February 1974.

[100] Herman A. Haus. Theory of mode locking with a fast saturable absorber. *Journal of Applied Physics*, 46(7):3049–3058, July 1975.

[101] Herman A. Haus. Theory of mode locking with a slow saturable absorber. *IEEE Journal of Quantum Electronics*, QE-11(9):736–746, September 1975.

[102] H. A. Haus. Parameter ranges for CW passive mode locking. *IEEE Journal of Quantum Electronics*, QE-12:169–176, March 1976.

[103] Herman A. Haus. Theory of modelocking of a laser diode in an external resonator. *Journal of Applied Physics*, 51(8):4042–4049, August 1980.

[104] Herman A. Haus. Modelocking of semiconductor laser diodes. *Japanese Journal of Applied Physics*, 20(6):1007–1020, June 1981.

[105] H. A. Haus and Y. Silberberg. Theory of mode locking of a laser diode with a multiple-quantum-well structure. *Journal of the Optical Society of America B*, 2(7):1237–1243, July 1985.

[106] Anthony E. Siegman. *Lasers.* University Science Books, California, USA, 1986.

[107] Govind P. Agrawal and N. Anders Olsson. Self-phase modulation and spectral broadening of optical pulses in semiconductor laser amplifiers. *IEEE Journal of Quantum Electronics*, 25(11):2297–2306, 1989.

[108] S. Gee, R. Coffie, P. J Delfyett, G. Alphonse, and J. Connolly. Intracavity gain and absorption dynamics of hybrid modelocked semiconducor lasers using multiple quantum well saturable absorbers. *Applied Physics Letters*, 71(18):2569–2571, November 1997.

[109] Radhakrishnan Nagarajan, Masayuki Ishikawa, Toru Fukushima, Randall S. Geels, and John E. Bowers. High speed quantum-well lasers and carrier transport effects. *IEEE Journal of Quantum Electronics*, 28 (10):1990–2008, October 1992.

[110] Hideki Hirayama, Junji Yoshida, Yasunari Miyake, and Masahiro Asada. Carrier capture time and its effect on the efficiency of quantum-well lasers. *IEEE Journal of Quantum Electronics*, 30(1):54–62, January 1994.

[111] Levon V. Asryan, Serge Luryi, and Robert A. Suris. Internal efficiency of semiconductor lasers with a quantum-confined active region. *IEEE Journal of Quantum Electronics*, 39(3):404–418, 2003.

[112] J. Mark and J. Mørk. Subpicosecond gain dynamics in InGaAsP laser amplifiers: Experiment and theory. *Applied Physics Letters*, 61 (19):2281–2283, November 1992.

[113] Katherine L. Hall, Erik R. Thoen, and Erich P. Ippen Ippen. *Nonlinear Optics in Semiconductors II*, volume 59 of *Semiconductors and Semimetals*, chapter 2. Nonlinearities in Active Media, pages 84–160. Academic Press, 1999.

[114] Alexander V. Uskov, J. R. Karin, Radhakrishnan Nagarajan, and J. E. Bowers. Dynamics of carrier heating and sweepout in waveguide saturable absorbers. *IEEE Journal on Selected Topics in Quantum Electronics*, 1(2):552–561, 1995.

[115] Alexander V. Uskov, J. R. Karin, J. E. Bowers, John G. McInerney, and Jean Le Bihan. Effects of carrier cooling and carrier heating in saturation dnamics and pulse propagation through bulk semiconductor absorbers. *IEEE Journal of Quantum Electronics*, 34(11):2162–2171, 1998.

[116] H. A. Haus. Mode-locking of lasers. *IEEE Journal on Selected Topics in Quantum Electronics*, 6(6):1173–1185, 2000.

[117] Roger G. M. P. Koumans and Raymond van Roijen. Theory for passive mode-locking of semiconductor laser structures including the effects of self-phase modulation, dispersion, and pulse collisions. *IEEE Journal of Quantum Electronics*, 32(3):478–492, March 1996.

[118] D. J. Jones, L. M. Zhang, J. E. Carroll, and D. D. Marcenac. Dynamics of monolithis passicely mode-locked semiconductor lasers. *IEEE Journal of Quantum Electronics*, 31(6):1051–1058, 1995.

[119] S. Bischoff, M. P. Sørensen, J. Mørk, S. D. Brorson, T. Franck, J. M. Nielsen, and A. Møller-Larsen. Pulse-shaping mechanism in colliding-pulse mode-locked laser diodes. *Applied Physics Letters*, 67(26):3877–3879, 1995.

[120] M. Schell, M. Tsuchiya, and T. Kamiya. Chirp and stability of mode-locked semiconductor lasers. *IEEE Journal of Quantum Electronics*, 32 (7):1180–1190, 1996.

[121] B. Zhu, I. H. White, R. V. Penty, A. Wonfor, E. Lach, and H. D. Summers. Theoretical analysis of timing jitter in monolithic multisection mode-locked DBR laser diodes. *IEEE Journal of Quantum Electronics*, 33(7):1216–12220, 1997.

[122] D. J. Dericson, P.A. Morton, and J.E. Bowers. Comparison of timing jitter in external and monolithic cavity mode-locked semiconductor lasers. *Applied Physics Letters*, 59(26):3372–3374, December 1991.

[123] Roland Peter Schreieck. *Ultrafast Dynamics in InGaAsP/InP Optical Amplifiers and Mode Locked Laser Diodes.* PhD thesis, ETHZ, Zurich, Switzerland, 2001. Diss. ETH No. 14337.

[124] S. Arahira, N. Mineo, K. Tachibana, and Y. Ogawa. 40 GHz hybrid modelocked laser diode module operated at ultra-low RF power with impedance-matched circuit. *Electronics Letters*, 39(3):287–289, 2003.

[125] J. L. A. Dubbeldam and D. Lenstra. Noise in slow saturable absorber mode-locked semiconductor lasers. *Applied Physics Letters*, 75(8):1066–1068, 1999.

[126] T. Yilmaz, C. M. Depriest, P. J. Delfyett, Braun A., and J. Abeles. Measurement of residual phase noise and longitudinal-mode linewidth in a hybridly mode-locked external linear cavity semiconductor laser. *Optics Letters*, 27(10):872–874, 2002.

[127] Govind P. Agrawal. *Fiber-Optic Communication Systems.* Wiley Series In Microwave and Optical Engineering. John Wiley & Sons, Inc, New York, USA, second edition, 1997.

[128] R. Ludwig, S. Diez, A. Ehrhart, L. Küller, W. Pieper, and H. G. Weber. A tunable femtosecond modelocked semiconductor laser for applications in OTDM-systems. *IEICE Trans. Electron.*, E81(2):139–144, February 1998.

[129] E. A. Avrutin, Marsh J. H., and E. L. Portnoi. Monolithic and multi-GigaHertz mode-locked semiconductor lasers: Constructions, experiments, models and applications. *IEE Proc.- Optoelectronics*, 147(4): 251–278, 2000.

[130] M. Okai, M. Suzuki, and T. Taniwatari. Strained multiquantum-well currugation-pitch-modulated distributed feedback laser with ultranarrow (3.6 kHz) spectral linewidth. *Electronics Letters*, 29(19):1696–1697, 1993.

[131] Bin Zhao, Amnon Yariv, Alfred R. Adams, Eoin P. O'Reilly, Mark Silver, Radhakrishnan Nagarajan, and John E. Bowers. *Semiconductor Lasers I. Fundamentals*, chapter 1–3. Optics and Photonics. Academic Press, 1999. edited by Eli Kapon.

[132] Shun Lien Chuang. *Physics of Optoelectronic Devices*. John Wiley & Sons, Inc, New York, 1995.

[133] P. A. Morton and et al. 25 GHz bandwidth 1.55 μm GaInAsP p-doped strained multiquantum-well lasers. *Electronics Letters*, 28(23): 2156–2157, 1992.

[134] Marcus Dülk, Max Döbeli, and Hans Melchior. Fabrication of saturable absorbers in InGaAsP-InP bulk semiconductor laser diodes by heavy ion implantation. *IEEE Journal on Selected Topics in Quantum Electronics*, 7(2):124–134, 2001.

[135] Hisakazu Kurita, Ichiro Ogura, and Hiroyuki Yokoyama. Ultrafast all-optical signal processing with mode-locked semiconductor lasers. *IEICE Trans. Electron.*, E81 C(2):129–139, February 1998.

[136] P.B. Hansen, G. Raybon, U. Koren, B.I. Miller, M.G. Young, Chien M., C.A. Burrus, and R.C. Alferness. 5.5-mm long InGaAsP monolithic extended-cavity laser with an integrated Bragg -reflector for active mode-locking. *IEEE Photonics Technology Letters*, 4(3):215–217, 1992.

[137] L. R. Brovelli, R. Germann, J. P. Reithmaier, H. Jäckel, H. P. Meier, and H. Melchior. Transform-limited picosecond optical pulses from a mode-locked InGaAs/AlGaAs QW laser with integrated passive waveguide cavity and QW modulator. *IEEE Photonics Technology Letters*, 5 (8):896–899, 1993.

[138] E. Zielinski, E. Lach, J. Bouayad-Amine, H. Haisch, E. Kühn, M. Schilling, and J. Weber. Monolithic multisegment mode-locked DBR laser for wavelength tunable picosecond pulse generation. *IEEE Photonics Technology Letters*, 3(2):230–232, April 1997.

[139] H. Fan, C. Wu, M. El-Aasser, N.K. Dutta, U. Koren, and A. B. Piccirilli. Colliding pulse mode-locked laser. *IEEE Photonics Technology Letters*, 12(8):972–973, August 2000.

[140] M. Schilling, J. Bouayad-Amine, T. Feeser, H. Haisch, E. Kühn, E. Lach, K. Satzke, J. Weber, and E. Zielinski. Monolithic mode locked DBR laser with multiple-bandgap MQW structure realized by selective area growth. In *IPRM 1996. Eighth International Conference on Indium Phosphide and Related Materials*, USA, 1996. IEEE.

[141] A. Catrina Bryce, Fernando Camancho, Pasquale Cusumano, and John H. Marsh. CW and mode-locked integrated extended cavity lasers fabricated using impurity free vacancy disordering. *IEEE Journal on Selected Topics in Quantum Electronics*, 3(3):885–892, June 1997.

[142] F. Camancho, E. A. Avrutin, P. Cusumano, A. Saher Helmy, A. C. Bryce, and J. H. March. Improvements in mode-locked semiconductor diode lasers using monolithically integrated passive waveguides made by quantum-well intermixing. *IEEE Photonics Technology Letters*, 9 (9):1208–1210, September 1997.

[143] I. Ogura, H. Kurita, T. Sasaki, and H. Yokoyama. Precise operation-frequency control of monolithic mode-locked laser diodes for high-speed optical communication and all-optical signal processing. *Optical and Quantum Electronics*, 33:709–725, 2001.

[144] N. K. Dutta, J Lopata, P. R. Berger, D. L. Sivco, and A.Y Cho. Performance characteristics of GaInAs/GaAs large optical cavity quantum well lasers. *Electronics Letters*, 27(8):680–682, April 1991.

[145] R. H. Li, J. C. Zhong, B.R. Zhu, Y. J. Zhao, and Y Qu. High-power long-wavelength LOC laser diodes. *Proceedings of the SPIE - The International Society for Optical Engineering*, 2382:307–311, 1995.

[146] D.Z. Garbuzov, R.J. Menna, R.U. Martinelli, J.H. Abeles, and J.C. Connolly. High power continuous and quasi-continuous wave InGaAsP/InP broad-waveguide separate confinement heterostructure multiquantum well diode lasers. *Electronics Letters*, 33(19):1635–1636, September 1997.

[147] D. Z. Garbuzov. High-power 800- 2000-nm-wavelength broad-waveguide SCH-QW diode lasers. In *CLEO*, pages 10–11 / CMD2, USA, 1998.

[148] G. Fuchs, J. Hörer, A. Hangleiter, and A. Rudra. Carrier-induced localization in In-Ga-As/In-Ga-As-P separate-confinement quantum-well structure. *Physical Review B.*, 48(20):15175–15181, 1993.

[149] Ken Morito, Mitsuru Ekawa, Takayuki Watanabe, and Yuji Kotani. Low noise figure (6.3dB) polarization insensitive spotsize converter integrated semiconductor optical amplifier. *IEICE Trans. Electron.*, E85C (1):990–994, 2002.

[150] Ken Morito, Mitsuru Ekawa, Takayuki Watanabe, and Yuji Kotani. High-output-power polarization-insensitive semiconductor optical amplifier. *Journal of Lightwave Technology*, 21(1):176–181, 2003.

[151] Tommy W. Berg and Jesper Mørk. Quantum dot amplifiers with high output power and low noise. *Applied Physics Letters*, 82(18):3083–3085, 2003.

[152] S. Hojfeldt and J. Mork. Modeling of carrier dynamics in quantum-well electroabsorption modulators. *IEEE Journal on Selected Topics in Quantum Electronics*, 8(6):1265–1276, 2002. ISSN 1077260x.

[153] H. F. Liu, S. Arahira, T. Kunii, and Y. Ogawa. Generation of wavelength-tunable transform-limited pulses from a monolithic passively mode-locked distributed Bragg reflector semiconductor laser. *IEEE Photonics Technology Letters*, 7(10):1139–1141, October 1995.

[154] R. Kaiser, B. Hüttl, H. Heidrich, S. Fidorra, W. Rehbein, H. Stolpe, R. Stenzel, W. Ebert, and G. Sahin. Tunable monolithic mode-locked lasers on InP with low timing jitter. *IEEE Photonics Technology Letters*, 15(5):634–636, May 2003.

[155] R. S. Tucker, U. Koren, G. Raybon, C. A. Burrus, B. I. Miller, T. L. Koch, and G. Eisenstein. 40 GHz active mode-locking in a 1.5 μm monolithic extended-cavity laser. *Electronics Letters*, 25(10):621–622, 1989.

[156] K. Sato, I. Kotaka, A. Hirano, M. Asobe, Y. Miyamoto, and N. Shimizu. High-repetition frequency pulse generation at 102 GHz using modelocked lasers integrated with electroabsorption modulators. *Electronics Letters*, 34(8):790–792, 1998.

[157] Kenji Sato, Isamu Kotaka, Yasuhiro Kondo, and Mitsuo Yamamoto. High-repetition frequency pulse generation at over 50 GHz using mode-locked lasers integrated with electroabsorption modulators. *IEICE Trans. Electron.*, E81C(2):146–150, February 1998.

[158] Kenji Sato, Akira Hirano, and Hiroyuki Ishii. Chirp-compensated 40-GHz mode-locked lasers integrated with electroabsorption modulators and chirped gratings. *IEEE Journal on Selected Topics in Quantum Electronics*, 5(3):590–595, May/June 1999.

[159] Kenji Sato, Akira Hirano, Naofumi Shimizu, and Isamu Kotaka. High-frequency low-jitter optical pulse generation using semiconductor mode-locked lasers. *IEEE Transactions on Microwave Theory and Techniques*, 47(7):1251–1256, July 1999.

[160] Peter Blood. On the dimensionality of optical absorption, gain and recombination in quantum-confined structures. *IEEE Journal of Quantum Electronics*, 36(3):354–362, 2000.

[161] J. W. Matthews and A. E. Blakeslee. Defects in epitaxial multilayers. I. misfit dislocation. *Journal of Crystal Growth*, 27:118–125, 1974.

[162] Peter S. Zory, editor. *Quantum well lasers.* Academic Press, Inc, San Diego, USA, 1993.

[163] R. W. Glew, K. Scarrott, A. T. R. Briggs, V. A. Smith, A. D. Wilkinson, X. Zhou, and M. Silver. Elimination of wavy layer growth phenomena in strain-compensated GaInAsP/GaInAsP multiple quantum well stacks. *Journal of Crystal Growth*, 145:764–770, 1994.

[164] Gerald B. Stringfellow. *Organometallic Vapor-Phase Epitaxy: Theory and Practice.* Academic Press, 2nd edition, 1999.

[165] H. Hillmer, R. Losch, and W. Schlapp. Strain-balanced AlGaInAs/InP heterostructures with up to 50 QWs by MBE. *Journal of Crystal Growth*, 175-176:1120–1125, 1997. ISSN 00220248.

[166] Xiaodong Huang, A Stintz, Hua Li, L. F. julian Cheng Lester, and K. J. Malloy. Demonstration of passive Q-switching and passive mode-locking in 1.3 μm two-section InAs quantum dot lasers. In *Proceedings of CLEO*, page 359 / CWK7, USA, 2001.

[167] M. G. Thomson, C. Marinelli, K. T. Tan, K. A. Williams, R. V. Penty, I. H. White, I. N. Kaiander, R. L. Sellin, D. Bimberg, D.-J. Kang, M. G. Blamine, F. Visinka, S. Jochum, and S. Hansmann. Hybrid and passive mode-locking of quantum dot lasers at $\sim$10GHz. *Proceedings of ECIO'03*, (FrPD1 (post-deadline session)):1–4, 2003.

[168] A. Bilenca, A. Alizon, V. Mikhelashvili, G. Eisenstein, R. Schwertberger, D. Gold, J.P. Reithmaier, and A. Forchel. InAs/InP 1550 nm quantum dash semiconductor optical amplifiers. *Electronics Letters*, 39 (1):170–171, 2003. ISSN 00135194.

[169] Jacob B. Khurgin, Igor Vurgraftman, Jerry R. Shuangmei Xu Meyer, and Jin U. Kang. Reduced crosstalk semiconductor optical amplifiers based on type-II quantum wells. *IEEE Photonics Technology Letters*, 14(3):278–280, 2002.

[170] L. A. Coldren and Corzine S. W. *Diode Lasers and Photonic Integrated Circuits*. John Wiley & sons, inc, 1995.

[171] C. Kazmierski, A. Ougazzaden, D. Robein, D. Mathoorasing, M. Blez, and A. Mircea. 20 GHz bandwidth 1.5 μm wavelength VUG DFB laser using a zero net strain $In_{1-x}Ga_xAs_yP_{1-y}$ well active structure grown at constant y. *Electronics Letters*, 29(14):1290–1291, July 1993.

[172] A. Mircea, A. Ougazzaden, G. Primot, and C. Kazmierski. Highly thermally stable, high-performance InGaAsP:InGaAsP multi-quantum-well structures for optical devices by atmospheric pressure MOVPE. *Journal of Crystal Growth*, (124):737–740, 1992.

[173] J. Camassel, H. Peyre, and R. W. Glew. Quantitative investigation of interdissusion effects in balanced-strain InGaAs(P)/InGaAsP heterostructures: constant x vs. constant y. *Materials Science and Engineering*, B28:1994, 353–356 1994.

[174] D. C. Houghton, M. Davies, and M. Dion. Design criteria for structurally stable, highly strained multiple quantum well devices. *Applied Physics Letters*, 64(4):505–507, 1994.

[175] K. Streubel, J. Wallin, G. Landgren, U. Öhlander, S. Lourdudoss, and O. Kjebon. Importance of metalorganic vapor phase epitaxy growth conditions for the fabrication of GaInAsP strained quantum well lasers. *Journal of Crystal Growth*, (143):7–14, 1994.

[176] S. Guillon, R. Y.-F. Yip, P. Desjardins, M. Chicoine, Z. Bougrioua, M. Beaudoin, A. Aït-Ouali, and R. A. Masut. Low-pressure organometallic vapor phase epitaxy of coherent InGaAsP/InP and InGaAsP/InAsP multilayers on inp(001). *J. Vac. Sci. Technol. A*, 16(2): 781–785, 1998.

[177] P. A. Crump, H. Lage, W. S. Ring, R. M. Ash, J. Herniman, P.Z.A. Wrathall, S. amd DeSouza, and A. E. Staton-Bevan. Optimising 1550 nm InGaAsP strain compensated MQW lasers close to the miscibility gap. *IEE Proc.-Optoelectron*, 145(1):7–11, 1998.

[178] Thomas Brenner. *Monolithically Integrated Semiconductor Optical Amplifiers and Optical Mode Adaptors*. Ph.d. thesis, Swiss federal institute of technology Zurich, 1994.

[179] Kresten Yvind. Mode-locked semiconductor laser with an external cavity: Fabrication and experiment. M. Sc. thesis, COM, DTU, 1999.

[180] George E. Anner. *Planar Processing Primer*. Van Nostrand Reinhold, New York, USA, 1990.

[181] S. M. Sze. *Semiconductor Devices, Physics and Technology*. John Wiley & Sons, New York, USA, 1985.

[182] Ralph Williams. *Modern GaAs Processing Methods*. Artech House, 2nd edition, 1990.

[183] B. W. Hakki and T. L. Paoli. Gain spectra in GaAs double-heterostructure injection lasers. *Journal of Applied Physics*, 46(3):1299–1306, 1975.

[184] Ronald R. Willey. *Practical Design and Production of Optical Thin Films*. Marcel Dekker, Inc, 2002.

[185] Thomas Jøgensen. Mode-locked semiconductor laser with external cavity. - wavelength tuneable using a Bragg mirror. M. sc. thesis, The Niels Bohr Institute, University of Copenhagen, 2002.

[186] Martin Schell, Andreas G. Weber, Eckehard Schöll, and Dieter Bimberg. Fundamental limits of sub-ps pulse generation by active mode locking of semiconductor lasers: The spectral gain width and the facet reflectivities. *IEEE Journal of Quantum Electronics*, 27(6):1661–1668, June 1991.

[187] R. H. Clarke. Theoretical performance of anti-reflection coating for a diode laser amplifier. *Int. J. Electronics*, 53(5):495–499, 1982.

[188] M. Reed, P. Sewell, T. M. Benson, and P. C. Kendall. Limitations of one-dimensional models of waveguide facets. *Microwave and Optical Technology Letters*, 15(4):196–198, July 1997.

[189] R. H. Clarke. Theory of reflection from antireflection coatings. *The Bell System Technical Journal*, 62(10):2885–2891, December 1983.

[190] J. Wang, B. Mikkelsen, K. E. Stubkjaer, and D. S. Olesen. Single-layer coating for angled facet amplifier. *Electronics Letters*, 25(17): 1139–1141, August 1989.

[191] Pierre-André Besse, Jing-Song Gu, and Hans Melchior. Reflectivity minimization of semiconductor laser amplifiers with coated and angled facets considering two-dimensional beam profiles. *IEEE Journal of Quantum Electronics*, 27(6):1830–1836, June 1991.

[192] Jens Buus, Mark C. Farries, and David J. Robbins. Reflectivity of coated and tilted semiconductor facets. *IEEE Journal of Quantum Electronics*, 27(6):1837–1842, June 1991.

[193] M. Reed, T. M. Benson, P. C. Kendall, and P. Sewell. Antireflection-coated angled facet design. *IEE Proc.-Optoelectron*, 143(4):214–220, August 1996.

[194] P. Sewell, M. Reed, T.M. Benson, and P.C. Kendall. Full vector analysis of two-dimensional angled and coated optical waveguide facets. *IEEE Journal of Quantum Electronics*, 33(12):2311–2318, December 1997.

[195] A. Vukovic, P. Sewell, T. M. Benson, and P. C. Kendall. Advances in facet design for buries lasers and amplifiers. *IEEE Journal on Selected Topics in Quantum Electronics*, 6(1):175–184, 2000.

[196] P. C. Kendall, D. A. Roberts, P. N. Robson, M. J. Adams, and M. J. Robertson. Semiconductor laser facet reflectivities using free-space radiation modes. *IEE proceedings-J*, 140(1):49–55, February 1993.

[197] B. I. Bleaney and B. Bleaney. *Electricity and Magnetism.* Oxford science publications. Oxford University Press, third edition, 1993.

[198] *CRC Handbook of Chemistry and Physics.* The Chemical Rubber Company, Boca Raton, Florida, USA, 67 edition, 1986.

[199] P. T. Ho, L. A. Glasser, E. P. Ippen, and H. A. Haus. Picosecond pulse generation with a cw GaAlAs laser diode. *Applied Physics Letters*, 33(3):241–242, August 1978.

[200] P. T. Ho. Coherent pulse generation with a GaAlAs laser by active modelocking. *Electronics Letters*, 15(17):526–527, August 1979.

[201] M. B. Holbrook, W. E. Sleat, and Bradley D. J. Bandwidth-limited picosecond pulse generation in an actively mode-locked GaAlAs diode laser. *Applied Physics Letters*, 37(1):59–61, July 1980.

[202] K. Y. Lau and A. Yariv. Direct modulation and active mode locking of ultrahigh speed GaAlAs lasers at frequencies up to 18 GHz. *Applied Physics Letters*, 46(4):326–328, February 1985.

[203] R. S. Tucker, S.K. Korotky, G. Eisenstein, U. Koren, L. W. Stultz, and J. J. Veselka. 20 GHz active mode-locking of a 1.55 μm InGaAsP laser. *Electronics Letters*, 21(6):239–240, March 1985.

[204] E. P. Ippen, D. J. Eilenberger, and R. W. Dixon. Picosecond pulse generation by passive mode locking of diode lasers. *Applied Physics Letters*, 33(3):267–269, August 1980.

[205] John E. Bowers, Paul A. Morton, A. Mar, and Scott W. Corzine. Actively mode-locked semiconductor lasers. *IEEE Journal of Quantum Electronics*, 25(6):1426–1439, June 1989.

[206] Dennis J. Derickson, Roger J. Helkey, Alan Mar, Judy R. Karin, John G. Wasserbauer, and John E. Bowers. Short pulse generation using multisegment mode-locked semiconductor lasers. *IEEE Journal of Quantum Electronics*, 28(10):2186–2202, October 1992.

[207] D. J. Derickson, R. J. Helkey, A. Mar, J. R. Karin, J. E. Bowers, and R. L. Thornton. Suppression of multiple pulse formation in external-cavity mode-locked semiconductor lasers using intrawaveguide saturable Absorbers. *IEEE Photonics Technology Letters*, 4(4):333–335, April 1992.

[208] R. Ludwig and A. Ehrhardt. Turn-key-ready wavelength-, repetition rate- and pulsewidth-tunable femtosecond hybrid modelocked semiconductor laser. *Electronics Letters*, 31(14):1165–1167, July 1995.

[209] Hiroyuki Yokoyama. Highly reliable mode-locked semiconductor lasers. *IEICE Trans. Electron.*, E85C(1):27–36, 2002.

[210] F.X. Kärtner, U. Morgner, S. H. Cho, Y. Chen, H. A. Haus, J. G. Fujimoto, E. P. Ippen, V. Scheuer, M. Tilsch, and T. Tschudi. Ultrashort pulse generation with the Ti:Sapphire laser. In *CLEO'99*, page 83, Washington DC., USA, 1999. Optical Society of America.

[211] M. J. Brennan, J. N. Milgram, P. Mascher, and H. K. Haugen. Wavelength tunable ultrashort pulse generation from a passively mode-locked asymmetric-quantum-well semiconductor laser. *Applied Physics Letters*, 81(14):2502–2504, 2002.

[212] C. A. Williamson, M. J. Adams, A. D. Ellis, and A. Borghesani. Mode locking of semiconductor laser with curved waveguide and passive mode expander. *Applied Physics Letters*, 82(3):322–324, 2003.

[213] Roger Jonathan Helkey. *Subpicosecond Pulse Generation Using Modelocked Semiconductor Laser Diodes*. PhD thesis, University of California, Santa Barbara, USA, July 1993.

[214] M. C. Wu, Y. K. Chen, T. Tanbun-Ek, R. A. Logan, M. A. Chin, and G. Raybon. Transform-limited 1.4 ps optical pulses from a monolithic colliding-pulse mode-locked quantum well laser. *Applied Physics Letters*, 57(8):759–761, 1990.

[215] Y. K. Chen, M. C. Wu, R.A. Logan T. Tanbun-Ek, and M. A. Chin. Subpicosecond monolithic colliding-pulse mode-locked multiple quantum well lasers. *Applied Physics Letters*, 58(12):1253–1255, March 1991.

[216] M.C. Wu, Y.K. Chen, T. Tanbun-Ek, R. A. Logan, and M. A. Chin. Tunable monolithic colliding pulse mode-locked quantum-well lasers. *IEEE Photonics Technology Letters*, 3(10):874–876, October 1991.

[217] Young-Kai Chen and Ming C. Wu. Monolithic colliding-pulse mode-locked quantum-well lasers. *IEEE Journal of Quantum Electronics*, 28 (10):2176–2185, October 1992. Invited Paper.

[218] Shin Arahira, Yasuhito Matsui, Tatsuo Kunii, Saeko Oshiba, and Yoh Ogawa. Transform-limited optical short-pulse generation at high repetition rate over 40 GHz from a monolithic passive mode-locked DBR laser diode. *IEEE Photonics Technology Letters*, 5(12):1362–1365, December 1993.

[219] Hai-Feng Liu, Shin Arahira, Tatsuo Kunii, and Yoh Ogawa. Tuning characteristics of monolithic passively mode-locked distributed bragg reflector semiconductor lasers. *IEEE Journal of Quantum Electronics*, 32(11):1965–1975, November 1996.

[220] Y. Katoh, S. Arahira, and Y. Ogawa. 40 GHz actively mode-locked DBR laser diodes with a wide (800 MHz) locking range. *Optical Fiber Communication Conference and Exhibit, 2001. OFC 2001*, 3:WC5–1–3 vol.3, 2001.

[221] B. Huettl, R. Kaiser, F. Boczianowski, S. Fidorra, H. Heidrich, G. Jacumeit, M. Kroh, W. Rehbein, R. Stenzel, and H. Stolpe. Monolithic mode-locked laser on GaInAsP/InP for 160 Gb/s TDM applications. In *OFC Proceedings*, pages 675–676 / FF7, USA, 2003. OSA.

[222] Joseph H. Zarrabi, E. L. Portnoi, and A. V. Chelnokov. Passive mode locking of a multistripe single quantum well GaAs laser diode with an intracavity saturable absorber. *Applied Physics Letters*, 59(13):1526–1528, 1991.

[223] P.A. Morton, J.E. Bowers, L.A. Koszi, M. Soler, J. Lopata, and D. P. Wilt. Monolithic hybrid mode-locked 1.3 μm semiconductor lasers. *Applied Physics Letters*, 56(2):111–113, January 1990.

[224] Kenji Sato, Koichi Wakita, Isamu Kotaka, Yasuhiro Kondo, and Mitsuo Yamamoto. Monolithic strained-InGaAsP multiple-quantum well lasers with integrated electroabsorption modulators for active mode locking. *Applied Physics Letters*, 65(1):1–3, 1994.

[225] P. G. May and M. Bierbaum. Monolithic mode locking of long cavity GaAs-AlGaAs semiconductor lasers. *IEEE Photonics Technology Letters*, 3(4):296–298, 1991.

[226] H. Fan, N.K. Dutta, U. Koren, C. H. Chen, and A. B. Piccirilli. Modelocked distributed Bragg reflector laser. *Electronics Letters*, 35 (1):48–49, January 1999.

[227] D. P. Wilt, B. Schwartz, B. Tell, E. D. Beebe, and R. J. Nielson. Channeled substrate buried heterostructure InGaAsP/InP laser employing a buried Fe ion implant for current confinement. *Applied Physics Letters*, 44(3):290–292, 1984.

[228] Joaquim Martins-Filho, Eugene A. Avrutin, C. N. Ironside, and J. S. Roberts. Monolithic multiple colliding pulse mode-locked quantum-well lasers: Experiment and theory. *IEEE Journal on Selected Topics in Quantum Electronics*, 1(2):539–551, June 1995.

[229] Takanori Shimizu, Xinglong Wang, and Hiroyuki Yokoyama. Asymmetric colliding-pulse mode-locking in InGaAsP semiconductor lasers. *Optical Review*, 2(6):401–403, 1995.

[230] S.D. McDougall, C.N. Ironside, A.C. Bryce, J.H. Marsh, B. Vogele, and C.R. Stanley. Harmonic modelocking at up to 440 GHz repetition rates in InGaAs-InAIGaAs quantum well lasers. *Lasers and Electro-Optics Europe, 1998. 1998 CLEO/Europe. Conference on*, page 209.

[231] T. Shimizu, I. Ogura, and H. Yokoyama. 860 GHz rate asymmetric colliding pulse modelocked diode lasers. *Electronics Letters*, 33(22): 1868–1869, October 1997.

[232] Yoshitada Katagiri and Atsushi Takada. A harmonic colliding-pulse mode-locked semiconductor laser for stable subterahertz pulse generation. *IEEE Photonics Technology Letters*, 9(11):1442–1444, November 1997.

[233] Shin Arahira, Yukio Katoh, Daisuke Kunimatsu, and Yoh Ogawa. Stabilization and timing jitter reduction of 160 GHz colliding-pulse mode-locked laser by subharmonic-frequency optical pulse injection. *IEICE Trans. Electron.*, E83-C(6):966–973, June 2000.

[234] Shin Arahira, Yasuhiro Matsui, and Yoh Ogawa. Mode-locking at very high repetition rates more than terahertz in passively mode-locked distributed-Bragg-reflector laser diodes. *IEEE Journal of Quantum Electronics*, 32(7):1211–1224, July 1996.

[235] Dan. A. Yanson, Michael W. Street, Stewart D. McDougall, Iain G. Thayne, John H. Marsh, and Eugene A. Avrutin. Ultrafast harmonic mode-locking of monolithic compound-cavity laser diodes incorporating photonic-bandgap reflectors. *IEEE Journal of Quantum Electronics*, 38 (1):1–11, January 2002.

[236] D. Garbuzov, L Xu, S. R. Forrest, R. Menna, R. Martinelli, and J. C. Connelly. 1.5μm wavelength, SCH-MQW InGaAsP/InP broadened-waveguide laser diodes with low internal loss and high output power. *Electronics Letters*, 32(18):1717–1719, 1996.

[237] A. M. Braun, V. N. Khalfin, M. H. Kwakernaak, W. F. Reichert, L. A. DiMarco, Z. A. Shellenbarger, C. M. DePriest, T. Yilmaz, P. J. Delfyett, and J. H. Abeles. Universality of mode-locked jitter performance. *IEEE Photonics Technology Letters*, 14(8):1058–1060, 2002.

[238] Dag Roar Hjelme and Alan Rolf Mickelson. Theory of timing jitter in actively mode-locked lasers. *IEEE Journal of Quantum Electronics*, 28(6):1594–1606, 1992.

[239] David J. Jones, Kevin W. Holman, Mark Notcutt, Jun Ye, Juhi Chandalia, Leaf A. Jiang, Erich P. Ippen, and H. Yokoyama. Ultralow-jitter, 1550-nm mode-locked semiconductor laser synchronized to a visible optical frequency standard. *Optics Letters*, 28(10):813–815, 2003.

[240] M. Reed, P. Sewell, T. M. Benson, and P. C. Kendall. Reflectivity of two dimensional waveguide facets using the vector free space radiation mode method. *SPIE*, 2994:819–824, 1997.

[241] Allan W. Snyder and John D. Love. *Optical Waveguide Theory*. Kluwer Academic Publishers, Norwell, MA 02061, USA, 2000.

[242] Hermann A. Haus. *Waves and Fields in Optoelectronics*. Prentice-Hall series in solid state physical electronics. Prentice-Hall, New Jersey, USA, 1984.

[243] W. Gander and W. Gautschi. Adaptive quadrature revisited. http://www.inf.ethz.ch/personal/gander, 1998. Adaptsim; Standard implementation in Matlab as "quad".

[244] A.G. Failla, G.P. Bava, and I.Montrosset. Structural design criteria for polarization insensitive semiconductor optical amplifiers. *Journal of Lightwave Technology*, 8(3):302–308, 1990.

[245] B. Luo, L. Wu, J. Chen, and Y. Lu. Determination of wavelength dependence of the reflectivity of AR coated diode facets. *IEEE Photonics Technology Letters*, 5(11):1279–1281, November 1993.

[246] S. A. Merritt, C. Dauga, S. Fox, I.-F. Wu, and M. Dagenais. Measuremet of the facet modal reflectivity spectrum in high quality semiconductor traveling wave amplifiers. *Journal of Lightwave Technology*, 13(3):430–433, March 1995.

[247] Reinhold Ludwig. *Experimentelle Untersuchungen an Halbleiterlaserverstärkern für die optische Nachrichtentechnik*. PhD thesis, Technischen Universität Berlin, 1993.

[248] Byung-Kwon Kang, Yoon Ho Park, Seok Lee, Sang Sam Choi, Jungkeun Lee, Takeshi Kamiya, and Seung-Han Park. Measurement of facet reflectivity of antireflection-coated electroabsorption modulator using induced photocurrent. *IEEE Photonics Technology Letters*, 13(2): 112–114, 2001.

[249] Lorin F. Stokes. Accurate measurement of reflectivity over wavelength of a lasers diode antireflection coating using an external cavity laser. *Journal of Lightwave Technology*, 11(7):1162–1167, 1993.

[250] Chih-Sheng Chang, Shun Lien Chuang, Jeffrey R. Minch, Wei-chiao Fang, Y. K. Chen, and T. Tanbun-Ek. Amplified spontaneous emission

spectroscopy in strained quantum-well lasers. *IEEE Journal on Selected Topics in Quantum Electronics*, 1(4):1100–1107, December 1995.

[251] Murray R. Spiegel. *Mathematical Handbook of formulars and tables.* Schaum's outline series. McGraw-Hill, Inc, 1992.

[252] Govind P. Agrawal and Niloy K. Dutta. *Semiconductor Lasers.* Van Nostand Reinhold, New York, USA, second edition, 1993.

[253] Akinori Koukitu and Hisashi Seki. Thermodynamic analysis of the MOVPE growth of quarternary III-V alloy semiconductors. *Journal of Crystal Growth*, 76:233–242, 1986.

[254] I. Vurgaftman, J.R. Meyer, and L. R. Ram-Mohan. Band parameters for III-V compound semiconductors and their alloys. *Journal of Applied Physics*, 89(11):5815–5875, November 2001. Applied Physics Review.

[255] Chris G. Van de Walle. Band lineups and deformation potentials in the mode-solid theory. *Physical Review B.*, 39(3):1871–1883, 1989.

[256] Herbert Kroemer. Semiconductor heterojunctions at the conference on the physics and chemistry of semiconductor interfaces: A device physicist's perspective. *J. Vac. Sci. Technol. B*, 11(4):1354–1361, 1993.

[257] Giorgio Margarito. Heterojuntion band discontinuities: A fundamental problem in solid-state science. *J. Vac. Sci. Technol. B*, 11(4):1362–1369, 1993.

[258] J. Tersoff. Theory of semiconductor heterojunctions: The role of quantum dipoles. *Physical Review B.*, 30(8):4874–4877, 1984.

[259] P. Desjardins, M. Beaudoin, R. Leonelli, G. L'Espérance, and R.A. Masut. Structural and optical properties of strain-relaxed InAsP/InP heterostructures grown by metalorganic vapor phase epitaxy in InP(001) using tertiarybutylarsine. *Journal of Applied Physics*, 80(2):846–852, 1996.

[260] Walter A. Harrison. Elementary theory of heterojunctions. *J. Vac. Sci. Technol.*, 14(4):1016–1021, 1977.

[261] Takuya Ishikawa and John E. Bowers. Band lineup an in-plane effective mass of InGaAsP or InGaAlAs on InP strained-layer quantum well. *IEEE Journal of Quantum Electronics*, 30(2):562–570, 1994.

[262] J. Minch, S. H. Park, T. Keating, and S.L. Chuang. Theory and experiment of $\mathrm{In}_{1-x}\mathrm{Ga}_x\mathrm{As}_y\mathrm{P}_{1-y}$ and $In_{1-x-y}Ga_xAl_yAs$ long-wavelength strained quantum-well lasers. *IEEE Journal of Quantum Electronics*, 35(5):771–782, 1999.

[263] Chris G. Van de Walle and Richard M. Martin. Theoretical calculations of semiconductor heterojuntion discontinuities. *J. Vac. Sci. Technol. B*, 4(4):1055–1059, 1986.

[264] Chris G. Van de Walle and Richard M. Martin. Theoretical study of band offsetts at semiconductor interfaces. *Physical Review B.*, 35(15): 8154–8165, 1987.

[265] N. E. Christensen. Semiconductor heterojuntions and superlattices: band offsets and electronic structure. *Philosophical Magazine B*, 70(3): 567–581, 1994.

[266] Hartmut Haug and Stephan W. Koch. Semiconductor laser theory with many-body effects. *Physical Review A.*, 39(4):1887–1898, 1989.

[267] Doyeol Ahn and Shun Lien Chuang. The theory of strained-layer quantum-well lasers with bandgap renormalization. *IEEE Journal of Quantum Electronics*, 30(2):350–364, 1994.

[268] E. D. Palik (editor). *Handbook of Optical Constants of Solids*, volume I & II. Academic press, 1985 & 1991.

[269] Sadao Adachi. Refractive indices of III-V compounds: Key properties of InGaAsP relevant to device design. *Journal of Applied Physics*, 53 (8):5863–5869, 1982.

[270] B. Broberg and S. Lindgren. Refractive index of $\mathrm{In}_{1-x}\mathrm{Ga}_x\mathrm{As}_y\mathrm{P}_{1-y}$ layers and InP in the transparent wavelength region. *Journal of Applied Physics*, 55(9):3376–3381, 1984.

[271] Krister Fröjdh. PhD thesis, KTH, Stockholm, 1996.

[272] Martin A. Afromowitz. Refractive index of $Ga_{1-x}Al_xAs$. *Solid State Communications*, 15:59–63, 1974.

[273] Sadao Adachi. Optical dispersion relations for GaP, GaAs, GaSb, InP, InAs, InSb, $Al_xGa_{1-x}As$ and $\mathrm{In}_{1-x}\mathrm{Ga}_x\mathrm{As}_y\mathrm{P}_{1-y}$. *Journal of Applied Physics*, 66(12):6030–6040, 1989.

[274] Aleksandar D. Rakić and Marian L. Majewski. Modeling the optical dielctric function of GaAs and AlAs: Extension of Adachi's model. *Journal of Applied Physics*, 80(10):5909–5914, 1996.

[275] Aleksandra B. Djurišić, Aleksandar D. Rakić, Paul C. K. Kwok, E. Herbert Li, and Martin L. Majewski. Modeling the optical constants of GaP, InP, and InAs. *Journal of Applied Physics*, 85(7):3638–3642, 1999.

[276] Christian Tanguy. Refractive index of direct bandgap semiconductors near the absorption threshold: Influence of excitonic effects. *IEEE Journal of Quantum Electronics*, 32(10):1746–1750, 1996.

[277] K. B. Kahen and J. P. Leburton. Index of refraction of GaAs-$Al_xGa_{1-x}As$ superlattices and multiple quantum wells. *Superlattices and Microstructures*, 3(3):251–256, 1987.

[278] Dhrupad A. Trivedi and Neal G. Anderson. Modeling the near-gap refractive index properties of semiconductor multiple quantum wells and superlattices. *IEEE Journal on Selected Topics in Quantum Electronics*, 2(2):197–209, 1996.

[279] Laurent Chusseau, Patrick Martin, Céline Brasseur, Claude Alibert, Philippe Hervé, Philippe Arguel, Françoise Lozes-Dupuy, and E.V.K. Rao. Carrier-induced change due to doping in refractive index of InP: Measurements at 1.3 and 1.5 μm . *Applied Physics Letters*, 69(20): 3054–3056, 1996.

[280] Brian R. Bennett, Richard A. Soref, and Jesús A. del Alamo. Carrier-induced change in refractive index of InP, GaAs, and InGaAsP. *IEEE Journal of Quantum Electronics*, 26(1):113–122, 1990.

[281] L. D. Westbrook. Measurementes of dg/dN and dn/dN and their dependence on photon energy in $\lambda = 1.5$ μm InGaAsP laser diodes. *IEE Proceedings*, 133(2):135–142, 1986.

List of publications

[I] Nan Chi, Jianfeng Zhang, P. V. Holm-Nielsen, Lin Xu, I. T. Monroy, C. Peucheret, K. Yvind, L. J. Christiansen, and P. Jeppesen. Experimental demonstration of cascaded transmission and all-optical label swapping of orthogonal IM/FSK labelled signal. *Electronics Letters*, 39 (8):676–677, 2003. ISSN 00135194.

[II] E. Hilliger, J. Berger, H.G. Weber, K. Yvind, P.M.W. Skovgaard, and J. Hanberg. The cascaded amplifier and saturable absorber (CASA) all-optical switch. In *Photonics in Switching*, 2001. PThC.

[III] E. Hilliger, V.Marembert, C. Schubert, H.G. Weber, K. Yvind, and J. Hanberg. Improved electroabsorption demultiplexer by tandem-arrangement with semiconductor optical amplifier. In *OFC proceedings*, 2002. ThGG.

[IV] J. Lasri, A. Bilenca, D. Dahan, V. Sidorov, G. Eisenstein, D. Ritter, and K. Yvind. A self - starting hybrid optoelectronic oscillator generating ultra low jitter 10 GHz optical pulses and low phase noise electrical signals. *IEEE Photonics Technology Letters*, 14(7):1004–1006, 2002.

[V] J. Lasri, A. Bilenca, D. Dahan, V. Sidorov, G. Eisenstein, D. Ritter, and K. Yvind. An ultra low noise self - starting pulse generator. In *ECOC Proceedings*, 2002. 4.3.3.

[VI] Jesper Mørk, Kresten Yvind, Leif Oxenløwe, Peter M.W. Skovgaard, Francis Romstad, Svend Bischoff, Sune Højfeldt, Andrea Tersigni, Lotte Christiansen, Abbas Nik, Filip Öhman, Jørn M. Hvam, Jesper Hanberg, Karsten Hoppe, and Martin Løbel. SCOOP-semiconductor components for optical signal processing. *DOPS-nyt*, 16(2):25–30, 2001.

[VII] L.K Oxenloewe, E. Hilliger, A. Tersigni, A.M. Nik, S. Højfeldt, F. Romstad, K. Yvind, P.M.W. Skovgaard, K. Hoppe, and J. Hanberg.

All-optical demultiplexing and wavelength conversion in an electroabsorption modulator. In *ECOC proceedings*, pages 604–605, Holland, 2001.

[VIII] L.K. Oxenløwe, F. Romstad, A. Tersigni, S. Højfeldt, K. Yvind, P.M.W.Skovgaard, K. Hoppe, and J. Hanberg. Characterization of a MQW electroabsorption modulator as an all-optical demultiplexer. In *LEOS proceedings*, USA, 2001. IEEE. ME2.

[IX] L.K. Oxenløwe, A.I. Siahlo, K.S. Berg, A.T. Clausen, B.M. Srensen, K. Yvind, P. Jeppesen, K.P. Hansen, K. Hoppe, and J. Hanberg. A novel 160 Gb/s receiver configuration including a glass crystal pulsed laser, photonic crystal fibre and a simple dynamic clock recovery scheme. In *ECOC proceedings*, Italy, 2003. Accepted for publication.

[X] F. Romstad, F. Öhman, J. Mørk, K. Yvind, J. M. Hvam, and J. Hanberg. Short pulse absorption dynamics in a p-i-n InGaAsP MQW waveguide saturable absorber. In *ECOC Proceedings*, 2002. P2.25.

[XI] L. Xu, N. Chi, L.K. Oxenløwe, K. Yvind, J. Mørk, P. Jeppesen, and J. Hanberg. Optical label encoding using electroabsorption modulators and investigation of chirp properties. *Journal of Lightwave Technology*, August 2003. Accepted for publication.

[XII] L. Xu, L. K. Oxenløwe, N. Chi, F. P. Romstad, K. Yvind, J. Mørk, P. Jeppesen, K. Hoppe, and J. Hanberg. Bandwith and chirp characterisation of wavelength conversion based on electroabsorption modulators. In *ECOC Proceedings*, 2002. P1.26.

[XIII] K. Yvind, L. J. Christiansen, D. Birkedal, J. Mørk, and J. Hanberg. External cavity mode-locked lasers employing reverse biased saturable absorbers. European Semiconductor Laser Workshop 2002, 2002.

[XIV] K. Yvind, T. Jørgensen, D. Birkedal, P.M.W. Skovgaard, and Jesper Hanberg. Tunable mode-locked semiconductor laser with Bragg mirror external cavity. In *LEOS Proceedings*, pages 789–790, USA, 2002. IEEE. ThS1.

[XV] K. Yvind, D. Larsson, L. J. Christiansen, C. Angelo, L. K. Oxenløwe, J. Mørk, D. Birkedal, J. M. Hvam, and J. Hanberg. Low-jitter and high-power all-active mode-locked lasers. In *ECOC proceedings*, Italy, 2003. Accepted for publication.

[XVI] K. Yvind, P. M. W. Skovgaard, J. Mørk, J. Hanberg, and M. Kroh. Performance of external cavity mode-locked semiconductor lasers employing reverse biased saturable absorbers. *Physica Scripta*, T101:129–132, 2002.

Appendix A

FSRM theory

A.1 Free space radiation mode theory

In this appendix the theory used for the calculations on AR coatings in Chap. 5 is outlined. The method used is the full-vectorial free space radiation mode (FSRM) method as published in [194, 240]. However, these references are flawed and uses an unclear nomenclature so a derivation is justified.

A.1.1 FSRM derivation

The structure under investigation is shown in Fig. A.1 along with some definitions. I shall only consider an angled facet in one direction and single mode waveguides, so this is a simplification compared to Sewell at al. [194].

I will start the derivation assuming that the vectorial mode is known and the materials used are linear and non-magnetic. A good reference in relation to this method is [241] and for the admittances [242] will be a good supplement.

If we assume translationally invariant refractive index ($n(x, y)$) along the z-axis, the mode field must have the same symmetry. It can therefore be written as a superposition of fields of the form (bold font is used for vectors)

$$\mathbf{E}\left(x, y, z\right) = \mathbf{e}\left(x, y\right) \exp\left(-i\beta z\right) \tag{A.1}$$

$$\mathbf{H}\left(x, y, z\right) = \mathbf{h}\left(x, y\right) \exp\left(-i\beta z\right) \tag{A.2}$$

where an implicit $e^{i\omega t}$ time dependence is assumed.

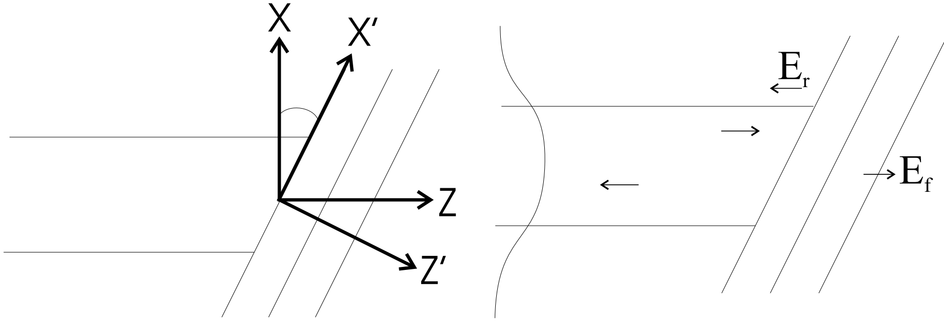

Figure A.1: Geometry of the waveguide facet. *Left*: Definition of axes. The y-axis is directed out of the plane of the paper. The coordinate system along the waveguide uses the unmarked coordinates, while the marked coordinates are for the coordinate system that has the z' axis normal to the facet rotated around y=y'. *Right*: Definition of fields. Guided modes (E, H) forward (+) and backwards (-). Radiation modes forward E_f and reverse E_r

We now decompose the field into components transverse (subscript t) and parallel (z) to waveguide axis and omit the explicit x & y dependence.

$$\mathbf{E} = (\mathbf{e}_t + e_z \hat{z}) \exp(-i\beta z) \tag{A.3}$$

$$\mathbf{H} = (\mathbf{h}_t + h_z \hat{z}) \exp(-i\beta z) \tag{A.4}$$

If the direction of propagation is reversed ($\beta \rightarrow -\beta$) the forward (+) and backward (-) fields are related to each other by [241]:

$$\mathbf{e}^- = \mathbf{e}_t^+ - e_z^+ \hat{z} \tag{A.5}$$

$$\mathbf{h}^- = -\mathbf{h}_t^+ + h_z^+ \hat{z} \tag{A.6}$$

The boundary condition at the facet is continuity of the tangential components of the **e** and **h** fields (see Fig. A.1)

$$\left[\mathbf{e}^+ \exp(-i\beta z) + r\,\mathbf{e}^- \exp(i\beta z) + \mathbf{e}_r(x, y, z)\right] \times \hat{z}' = \left[\mathbf{e}_f(x, y, z)\right] \times \hat{z}' \tag{A.7}$$

$$\left[\mathbf{h}^+ \exp(-i\beta z) + r\,\mathbf{h}^- \exp(i\beta z) + \mathbf{h}_r(x, y, z)\right] \times \hat{z}' = \left[\mathbf{h}_f(x, y, z)\right] \times \hat{z}' \tag{A.8}$$

with r being the field reflection coefficient.

The fourier transform of the fields $\tilde{\mathbf{e}}^{\pm}$ and $\tilde{\mathbf{h}}^{\pm}$ on the x' $y'(=y)$ plane can be written as

$$\tilde{\mathbf{e}}^{\pm}\left(s',t'\right)=\cos\theta\iint \begin{array}{l}\left(\begin{bmatrix}\cos\theta & 0\\ 0 & 1\end{bmatrix}\mathbf{e}_t \mp e_z\sin\theta\hat{x}'\right)\\ \cdot\exp\left(-i\left(\dfrac{s'\pm\beta\sin\theta}{\cos\theta}x+t'y\right)\right)dxdy\end{array} \tag{A.9}$$

$$\tilde{\mathbf{h}}^{\pm}\left(s',t'\right)=\cos\theta\iint \begin{array}{l}\left(\pm\begin{bmatrix}\cos\theta & 0\\ 0 & 1\end{bmatrix}\mathbf{h}_t - h_z\sin\theta\hat{x}'\right)\\ \cdot\exp\left(-i\left(\dfrac{s'\pm\beta\sin\theta}{\cos\theta}x+t'y\right)\right)dxdy\end{array} \tag{A.10}$$

where $s'(t')$ is the Fourier variable in the $x'(y'=y)$ direction and we only consider the $\hat{x}'$ and $\hat{y}'$ components as the $\hat{z}'$ component can be calculated from the two first for instance $\vec{k}\cdot\tilde{\mathbf{e}}=0$ with $\vec{k}=(s',t',\beta_f)$ being the wave vector [241].

Thus, transforming Eqs. (A.7) and (A.8) into fourier space we get

$$\tilde{\mathbf{e}}^{+}\left(s',t'\right)+r\,\tilde{\mathbf{e}}^{-}\left(s',t'\right)+\tilde{\mathbf{e}}_r\left(s',t'\right)=\tilde{\mathbf{e}}_f\left(s',t'\right) \tag{A.11}$$

$$\tilde{\mathbf{h}}^{+}\left(s',t'\right)+r\,\tilde{\mathbf{h}}^{-}\left(s',t'\right)+\tilde{\mathbf{h}}_r\left(s',t'\right)=\tilde{\mathbf{h}}_f\left(s',t'\right) \tag{A.12}$$

The fields $\tilde{\mathbf{e}}_r\left(s',t'\right)$ and $\tilde{\mathbf{e}}_f\left(s',t'\right)$ are assumed to be propagating in "free space", which means that a simple admittance operator relates the components of the electric and magnetic fields ($\omega\mu\mathbf{H}=\vec{k}\times\mathbf{E}$) e.g.

$$\tilde{\mathbf{h}}_r\left(s',t'\right)=\mathbf{Y_r}\left(s',t'\right)\tilde{\mathbf{e}}_r\left(s',t'\right) \tag{A.13}$$

and similar for $\mathbf{Y_f}$. The admittance operators can be derived from the scalar operators as

$$\tilde{\mathbf{h}}_f\left(s',t'\right)=\begin{bmatrix}\cos\varsigma & \sin\varsigma\\ \sin\varsigma & -\cos\varsigma\end{bmatrix}\begin{bmatrix}Y_{TE} & 0\\ 0 & Y_{TM}\end{bmatrix}\begin{bmatrix}\sin\varsigma & -\cos\varsigma\\ -\cos\varsigma & -\sin\varsigma\end{bmatrix}\tilde{\mathbf{e}}_f\left(s',t'\right) \tag{A.14}$$

$$\cos\varsigma=\frac{s'}{\sqrt{s'^2+t'^2}},\ \sin\varsigma=\frac{t'}{\sqrt{s'^2+t'^2}} \tag{A.15}$$

where the scalar admittances are

$$Y_{TE}=\frac{\beta_f}{\eta_0 k_0},Y_{TM}=\frac{n^2k_0}{\beta_f}, \tag{A.16}$$

n is the refractive index of the medium and

$$\beta_f^2 = n_f^2 k_0^2 - s'^2 - t'^2, \ k_0 = \frac{2\pi}{\lambda}, \ \eta_0 = 376.732\Omega \tag{A.17}$$

For multilayer structures a recurrence relation can be used:

$$(Y_f)_{i+1} = y_{oi} \frac{(Y_f)_i + j y_{oi} \tan(\beta_i d_i)}{y_{oi} + j (Y_f)_i \tan(\beta_i d_i)} \tag{A.18}$$

where $\beta_i^2 = n_i^2 k_0^2 - s'^2 - t'^2$ and the characteristic admittance y_{oi} is $\frac{\beta_i}{\eta_0 k_0}$ for TE and $\frac{n_i^2 k_0}{\beta_i}$ for TM for a layer (i) with thickness d_i and index n_i. Equation (A.16) is used for $(Y_f)_0$.

Now, using Eq.(A.13) to eliminate $\tilde{\mathbf{e}}_f$ in Eqs.(A.11) and (A.12) we get an equation for $\tilde{\mathbf{e}}_r$

$$(\mathbf{Y}_f - \mathbf{Y}_r)^{-1} \left[\left(\tilde{\mathbf{h}}^+ - \mathbf{Y}_f \tilde{\mathbf{e}}^+ \right) + r \left(\tilde{\mathbf{h}}^- - \mathbf{Y}_f \tilde{\mathbf{e}}^- \right) \right] = \tilde{\mathbf{e}}_r \equiv \tilde{\mathbf{e}}_r^1 + r \tilde{\mathbf{e}}_r^2 \tag{A.19}$$

where the last equality is used to define $\tilde{\mathbf{e}}_r^1$ and $\tilde{\mathbf{e}}_r^2$.

Finally we require that the radiation field is orthogonal to the guides modes i.e.

$$\iint \left([\mathbf{E}_r \times \mathbf{H}^{-*} + \mathbf{E}^{-*} \times \mathbf{H}_r] \cdot \hat{z}' \right) dx dy = 0 \tag{A.20}$$

This equation can be solved in Fourier space using Parseval's theorem, so by inserting Eq.(A.19) and Eq.(A.13) into Eq.(A.20) and isolating r the final result is

$$r = \frac{\left(\int_{\eta=\pi/2+0i}^{\pi/2+\infty i} + \int_{\eta=0}^{\pi/2} \right) \int_{\varsigma=0}^{2\pi} \left(\tilde{h}_y^- \tilde{e}_{r,x}^1 - \tilde{h}_x^- \tilde{e}_{r,y}^1 - \tilde{e}_y^- \tilde{h}_{r,x}^1 + \tilde{e}_x^- \tilde{h}_{r,y}^1 \right) u \beta_f d\varsigma d\eta}{\left(\int_{\eta=\pi/2+0i}^{\pi/2+\infty i} + \int_{\eta=0}^{\pi/2} \right) \int_{\varsigma=0}^{2\pi} \left(\tilde{h}_y^- \tilde{e}_{r,x}^2 - \tilde{h}_x^- \tilde{e}_{r,y}^2 - \tilde{e}_y^- \tilde{h}_{r,x}^2 + \tilde{e}_x^- \tilde{h}_{r,y}^2 \right) u \beta_f d\varsigma d\eta} \tag{A.21}$$

where a new variable substitution has been done to avoid an integrable singularity $1/\beta_f$ (see also [194])

$$s' = u \cos\varsigma, \ t' = u \sin\varsigma, \ u = n_f k_0 \sin\eta, \ \beta_f = n_f k_0 \cos\eta. \tag{A.22}$$

The double integration path in Eq.(A.21) ensures that β_f is integrated from 0 to ∞. The intensity reflection coefficient (R) is calculated from r as $R = |r|^2$.

The choice of refractive index for the backward radiating modes in Eq.(A.16) is uncritical [194] and I use the effective refractive index of the mode.

When r has been calculated, the farfield can be obtained from Eqs.(A.11), (A.12), and (A.19).

A.1.2 Numerical implementation

The FRSM method was implemented using the *Matlab* programming environment. The integrals in Eq. (A.21) were solved using an adaptive quadrature implementation of simpsons rule [243] adjusted to the present problem. Each partial interval was made to converge within each subinterval to a user defined accuracy. For problems where multiple calculations should be done using the same mode it proved to be very advantageous to map out $\tilde{\mathbf{e}}^{\pm}(\varsigma, \eta)$ and $\tilde{\mathbf{h}}^{\pm}(\varsigma, \eta)$ corresponding to the available RAM. On a pentium III and 256 MB ram each calculation of the reflection coefficient took less than a second, when additional points were not needed to achieve the set accuracy. For coating optimizations or angled coatings, where reflection coefficients of less than 10^{-7} were encountered, the calculation time increased significantly as interpolation of the gridded data had to be employed. For normal facets and symmetric modes, symmetry can be used to reduce the number of calculations.

Besides keeping track of the many vectorial components, the main pitfalls in the implementation are to ensure the proper signs of the imaginary parts of the variables.[1]

The calculations were verified against the original paper of Sewell et al.[194] and "identical" results were found.

The calculations were also compared with "standard" fourier calculations [244] done by Loredana Caruso in the group of Ivo Montrosset at Politecnico di Torino for the structure in Fig. 5.1 (left). Their result, which should be expected to be a little less accurate, for a normal facet at 1550 nm is 0.7 nm thinner TiO_s and 8.7 nm thicker SiO_2. Only the latter will be significant for a good coating system, and both methods are gross improvements to the plane wave method.

No comparison has been made to "exact" calculations on structures with large index contrast as, to my knowledge, no such calculations exist.

[1] As a side note Matlab changed the sign of the imaginary part of arcus sinus when changing from release 12 to 13!

Appendix B

Modal reflection measurement

B.1 Coating evaluation

In this appendix the theory used for evaluating the modal reflection coefficient for coated facets is outlined.

The evaluation method should be able to measure very low reflectivities in a wide wavelength range. A good antireflection coating has an intensity reflection coefficient of $10^{-4} - 10^{-5}$, which makes it difficult to measure accurately. For external cavity lasers the need to evaluate a broad bandwidth is evident. However, more importantly knowing the reflection in a broad bandwidth can be used to fine-tune the coating. If a minimum is seen in the reflectivity curve at a shorter wavelength than desired, the top layer can be make slightly thicker and thereby the reflectivity at the design wavelength can be lowered. For the two-layer coatings used in this work some information of the first layer can also be deduced. If the minimum reflectivity increases when the last layer is made thicker, this is a sign of the first layer being too thin. This can then be corrected in the next run.

A number of methods exist, that could fulfill the above requirements, based on measurement of ASE [245–247], induced photocurrent [248] or threshold in an external cavity laser [249]. The ASE based measurements are the easiest when the device emits ASE in the region, where the reflectivity is to be measured. This is not however not the case for an EAM, where [248] should be used instead.

The chosen method is based work by R. Ludwig [247] and a short derivation will be given below. A schematic of the device under test is shown in Fig. B.1, with definitions of some of the parameters.

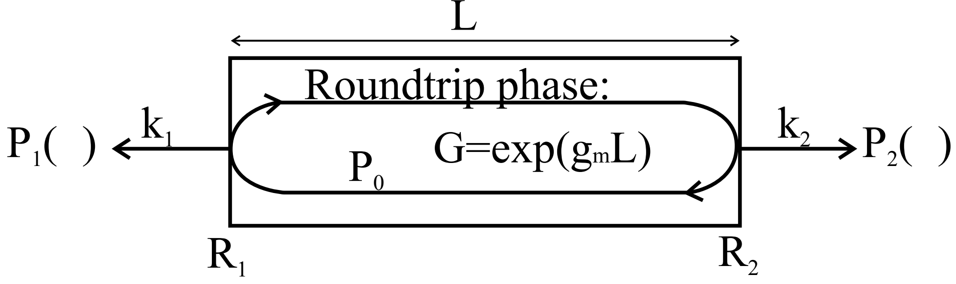

Figure B.1: Schematic of device geometry for coating evaluation. R: Intensity reflection coefficient. k: coupling coefficients. P_0: Spontaneous emission power.

The ASE power (P_1) from facet 1 coupled to a detector can be written as [247, 250]

$$P_1 = k_1 \frac{(1-R_1)(1+R_2G)}{(1-G\sqrt{R_1R_2})^2 + 4G\sqrt{R_1R_2}\sin^2\varphi} \frac{(G-1)P_0}{g_m} \tag{B.1}$$

All variables are a function of wavelength with the net modal gain g_m and single pass gain G related by

$$G = exp(g_m L) \tag{B.2}$$

The round trip loss (D^2) (i.e. internal) is defined as

$$D = G\sqrt{R_1R_2} \tag{B.3}$$

If we isolate the peaks (subscript p) i.e. $sin^2\varphi = 0$ and valleys (subscript v) i.e. $sin^2\varphi = 1$ in Eq.(B.1) and insert D we get

$$P_{1p} = k_1 \frac{(1-R_1)(1+R_2G)}{(1-D)^2} \frac{(G-1)P_0}{g_m} \tag{B.4}$$

$$P_{1v} = k_1 \frac{(1-R_1)(1+R_2G)}{(1+D)^2} \frac{(G-1)P_0}{g_m} \tag{B.5}$$

The modulation depth (M) of the ASE spectrum is defined as

$$M = \frac{P_p - P_v}{P_p + P_v} \tag{B.6}$$

Inserting Eqs. (B.4) and (B.5) into Eq. (B.6) it is easyly shown that

$$D = \frac{1-\sqrt{1-M^2}}{M} \tag{B.7}$$

Thus, D can be directly obtained from a measurement of the spectrum.[1] As seen in Eq. (B.3), D is a function of three parameters. If we assume that one facet is uncoated and measure the spectrum before (unmarked) and after (marked) coating, at the same current well below threshold, so that G is the same for both measurements, the reflectivity of the other facet can be found from

$$R' = \frac{D'^2}{D^2} R \tag{B.8}$$

This is the method of [245]. As the measurement is done below the precoating threshold, the modulation depth is very low and require very sensitive measurement techniques. Also, polarizers are needed as the power in TE and TM polarization will be comparable. The advantage of the method is that the exact magnitude of the coupling coefficient (k) is not important as only the modulation depths are used in the calculation. The sensitivity can be improved by smoothing and fitting the measured curves or by Fourier analysis of the ASE spectrum [246]

A method more suitable when the reflectivity is low ($< 10^{-3}$) is presented in [247] and involves measuring the spectrum of the coated diode from both ends of the device. The coated diode will have a very high threshold and it can therefore be driven at a higher current where more ripple exist without suffering from excessive gain compression. The current should be kept sufficiently low so the ripple is broad enough to be resolved by the spectrum analyzer and that gain compression is not too large. This will also ensure that the spontaneous emission power is constant throughout the device. If we assume that we somehow know the ratio of coupling coefficients $\frac{k_1}{k_2}$ (see Sec. B.1.1) we have for the ratio of peak powers:

$$\frac{P_{1p}}{P_{2p}} = \frac{k_1}{k_2} \frac{(1-R_1)(1+R_2G)}{(1-R_2)(1+R_1G)} \tag{B.9}$$

Eliminating the reflectivity of the unknown facet (now R_1) using

$$R_1 = \frac{D^2}{R_2 G^2} \tag{B.10}$$

where D is known from Eq. (B.7), we arrive at a third order equation in G which can be solved analytically [251]

$$G^3 + G^2 \left(\frac{1}{R_2} - \frac{(1-R_2)}{R_2} \frac{P_{1p}k_2}{P_{2p}k_1} \right) - GD^2 \left(\frac{1}{R_2} + \frac{(1-R_2)}{R_2^2} \frac{P_{1p}k_2}{P_{2p}k_1} \right) - \frac{D^2}{R_2^2} = 0 \tag{B.11}$$

[1]Below threshold and for uncoated facets Eqs. (B.7) and (B.3) can be used to determine the gain. This is the Hakki Paoli method [183]

Having equated G the unknown reflectivity (R_1) can be obtained from Eq. (B.10). This can then be done at all the wavelengths where the ripple can be measured accurately. If the photon density is so high that the carrier density is not reasonable constant throughout the device, P_0 will not be constant and the values at especially short wavelength will be inaccurate. However, it will still give some information, that can be used to adjust the outmost layer of the coating.

B.1.1 Coupling coefficients

One drawback of the procedure outlined above is the need to know the ratio of coupling coefficients. These will not be constant between measurements and a method of estimating $\frac{k_1}{k_2}$ is needed. However, we may assume that the ratio of coupling coefficients is approximately independent of wavelength so if we know the ratio in part of the spectrum we can use this value for the whole curve.

Now, looking at the spontaneous emission well below the bandgap we may note the following:

1. The number of emission states are limited and the population will not change much, if the total carrier density is changed a little due to stimulated emission.

2. The device has net loss at these wavelengths, thus reflected photons from one facet will not show up strongly at the other facet.

Because the amount of spontaneous emission is the same in the two sides at long wavelengths, we can therefore adjust the curves from the coated and uncoated facet so they overlap here.

The first item from above is important as the total power emitted from the two facets will be different and so will the carrier density through the stimulated emission process. This will have a much larger impact on the short wavelength side. Concerning the second item, it is possible to include the contribution from the first facet by inserting approximate values of $G(<1)$ and R_1 into Eq. (B.9). For good coatings and typical loss this simply corresponds to adjusting for the different transmission in the two sides.

B.2 Measurement example

Shown in Fig. B.2 (left) is an example of a measurement on a 330 μm long and 3 μm wide component (SCOOP3_10) at 60 mA current. The shown

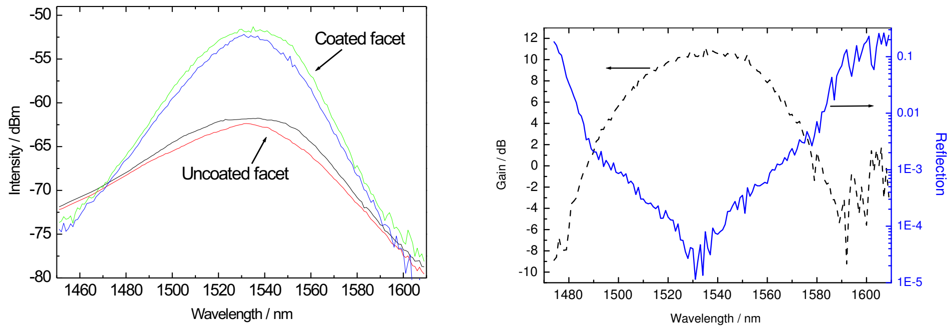

Figure B.2: *Left*: Envelope of optical spectrum from the coated and uncoated side of the component. The curve from the coated facet have been corrected such that they align in the long wavelength side. *Right*: Gain and reflection calculated from the curves in the left graph.

curves are the envelope of the emission and the curves from the coated facet have been corrected to align at the long wavelength side taking the larger transmission on the coated facet into account. The narrowing of the ASE at 1530 nm is a clear signature of a very good coating and the result of the calculation Eqs. (B.11) and (B.10) is shown in Fig. B.2 (right). This coating was extremely good and a minimum around 10^{-5} is seen. Unfortunately, coatings of this quality could not be fabricated reproducibly.

For the measurement it is important to use an isolator when measuring the coated facet as even the reflection from a unterminated fiber connector can make significant changes to the ASE spectrum. A good test to see if the measurement, is valid is to ensure that D from Eq. (B.7) is the same for measurements from both facets.

Appendix C

Material parameters

In this thesis various calculations on the optical and electronic properties of the devices were performed. I shall not go through all the basic quantum mechanic and electromagnetic theory as many excellent textbooks exist on the topics [131, 132, 162, 170, 252]. However, the choice of material parameters is extremely important when an attempt is done to match theory and practice and the books are not so strong here.

C.1 Band structure

Surprisingly, very different parameters are used in literature for important quantities like the bandgap and band lineup of $In_{1-x}Ga_xAs_yP_{1-y}$, which is used for calculating the emission wavelength from quantum wells. Part of the reason is that a reasonable correspondence can be found if just the same parameters are used for calibration of layer compositions and quantum wells. Initially the parameters of the otherwise excellent book by Chuang [132] was used, but some problems appeared during calibration runs on the MOCVD where layers with the same AsH_3/PH_3 ratio was grown. When each of the layers were evaluated independently, it turned out that there was a very large difference between the solid composition (y) in the two layers *opposite* to the (small) change that could be expected from thermodynamics [164, 253]. Also, the lowest QW transition energies did not fit well to the measured PL. The reason turned out to be the used material parameters.

I therefore highly recommend to use the parameters from a recent review (2001) by Vurgaftman et al. [254]. They have taken a critical look at the many parameters reported and compiled a set of parameters that are self consistent in the sense that for instance observations that include more than one parameter is included in the choosing of the right parameters.

This is very important as for instance changing the electron mass or band lineup might have the same effect on an observed QW emission energy. The paper also gives directions on how to interpolate the different parameters and provide a self-contained reference. I have included a compilation of the band parameters used in the thesis in Table C.1 without further explanation and refer to the paper.

Using [254] good correspondence between theory and practice is found as shown in Chap. 4 for a quantum well calculation. The transition energy that might be calculated using the parameters in Table 4.2 is 1533 nm which fit the measured PL within 5 nm. On the other hand using the formulas in [132] and the van de Walle lineup theory [255] as often seen in papers the transition energy would be 1.568 nm. A quite large difference.

C.1.1 Band lineup

The band lineup of semiconductor is complicated due to contribution from both the bulk and surface and the values are not finally resolved [256, 257].

A number of different lineup theories are used in literature, where they are backed up by experimental verification. Examples include the theories of Tersoff [258, 259], Harrison [260–262] and van de Walle [255, 263, 264][1]. Even though they all have some kind of experimental verification, there is 25 nm difference in the emission wavelength for a typical quantum well from e.g. the SCOOP6_3 wafer (Table 4.2) between the mentioned theories. It is not so much the physical reasoning, but more the actual values for the binaries that gives the different values. In practice, interpolation of binary values with some adjustment for strain is used and by using the experimental values in [254], this seems to works well.

C.1.2 Density of states

In Chap. 3 simple calculations of the carrier distributions in the devices are made. One of the problems in making these calculations is how to connect the density of states between the quantum confined states and the "bulk" material in the barriers and SCH as shown in Fig. C.1.

The DOS for a quantum well is taken as a constant for each state (proportional to the mass in the transverse plane) equivalent to assuming parabolic bands. This gives the usual staircase form

$$\rho_{QW}^{2D}(E) = N_w \frac{m_t^*}{\pi\hbar^2} \sum_n H(E - E^n) \tag{C.1}$$

[1]Other theories exist that combine the bulk and interface properties, but they have, to my knowledge, not yet been used in for device design. See e.g. [265]

	GaAs	InP	InAs	GaP	CGaInAs	CGaInP	CGaAsP	CInAsP	
a_{lc}	5.65325	5.8697	6.0583	5.4505	-	-	-	-	Å
Δa_{lc}	$3.88 \cdot 10^{-5}$	$2.79 \cdot 10^{-5}$	$2.74 \cdot 10^{-5}$	$2.92 \cdot 10^{-5}$	-	-	-	-	(T/K-300)Å
$E_g^{\Gamma}(0\text{K})$	1.519	1.4236	0.417	$2.886 + 0.1081(1 - \coth(164/T))$	0.477	0.65	0.19	0.10	eV
α	0.5405	0.363	0.276	-	-	-	-	-	meV/K
β	204	162	93	-	-	-	-	-	K
Δ_{so}	0.341	0.108	0.39	0.08	0.15	-	-	0.16	eV
γ_1	6.98	5.08	20.0	4.05	-	-	-	-	
γ_2	2.06	1.60	8.5	0.49	-	-	-	-	
E_p	28.8	20.7	21.5	31.4	-1.48	-	-	-	eV
F	-1.94	-1.31	-2.90	-2.04	1.77	0.78	-	-	
VBO	-0.80	-0.94	-0.59	-1.27	-0.38	-	-	-	eV
a_c	-7.17	-6.0	-5.08	-8.2	2.61	-	-	-	eV
a_v	-1.16	-0.6	-1.00	-1.7	-	-	-	-	eV
b	-2.0	-2.0	-1.8	-1.6	-	-	-	-	eV
c_{11}	1221	1011	832.9	1405	-	-	-	-	GPa
c_{12}	566	561	452.6	620.3	-	-	-	-	GPa
m^*_{hh}	-	-	-	-	-0.145	-	-	-	
m^*_{lh}	-	-	-	-	0.0202	-	-	-	

Table C.1: Compilation of the material parameters from [254]. See the original paper for explanation of the different parameters and interpolation methods. All growths was done on the (001) surface of the wafer.

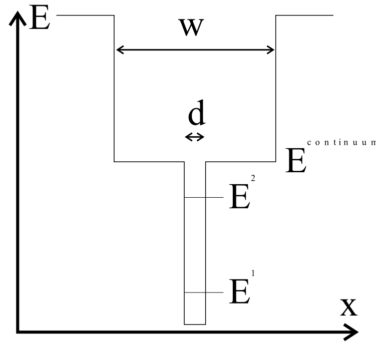

Figure C.1: Energy band schematic for DOS calculation

where H(E) is the Heavy-side step function and N_w is the number of wells.

For the bulk material, we still assume parabolic bands, but remove the quantum well width from the calculation such that the DOS is taken for a bulk material starting at $E^{continuum}$ with width $L_b = (w - d)$ referencing to Fig. C.1. Thus, for $E > E^{continuum}$

$$\rho^{2D}_{Bulk}(E) = \frac{L_b}{2\pi^2}\left(\frac{2m^*}{\hbar^2}\right)^{3/2}\sqrt{E - E^{continuum}} \tag{C.2}$$

and the total DOS is then $\rho^{2D}(E) = \rho^{2D}_{QW}(E) + \rho^{2D}_{Bulk}(E)$.

These simplification makes the calculations extremely easy but also of limited validity. The coupling between wells will smear out the density of states as will the neglected valence band mixing. The neglected Coulomb effects will change the shape of the bands due to different spatial carrier distributions between electrons and holes [148].

For gain calculations the finite lifetime of the states should be included which further smears out the gain spectrum. The different gain of TE and TM polarization should be calculated including the effect of the valence band mixing and matrix elements in order to ensure that lasing only occur on the ground state TE polarization. The procedure for such calculations are described well in [132].

The neglected many-body (Coulomb) interaction between the electrons will lower their total energy. This so-called bandgap re-normalization [266, 267] combined with heating lowers the lasing wavelength compared to the PL peak emission. Experimentally the PL wavelength is predicted well by the above theory, but the lasing wavelength for Fabry-Perot lasers are normally approximately 20 nm longer.

For the mode-locked lasers the emission is further red-shifted due to the spectral shape of the absorption. Also, as clearly seen in the measurements

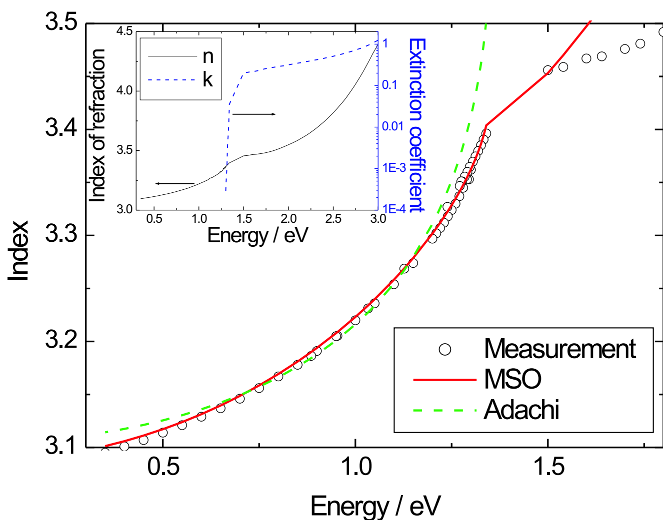

Figure C.2: Index of refraction of InP from [268], and results of the Adachi [269] and Modified Single oscillator (MSO) model [270] with finite broadening [271].

of Table 4.4 band-filling for the low confinement factor lasers have a strong influence on the lasing wavelength. The latter also exemplifies the fact that the density of states are not square as used in the simple calculations.

C.2 Refractive index

The refractive index of $In_{1-x}Ga_xAs_yP_{1-y}$ is needed for mode and coating calculations. The values in literature for bulk material are measured values that are fitted to a model. The predominant models are those by Adachi [269], and the modified single oscillator model by Afromowitz [270, 272]. In Fig. C.2 the two models are compared to experimental data from [268] in the case of InP. Even though the Adachi model is based on sound physics, it is inferior to the MSO especially close to the band gap. For the Adachi model more critical points than in the original paper can be included in the calculation [273–275], but these additions mainly improve the results in the region much above the bandgap and not in the near gap region which is interesting for device applications. I have therefore chosen to use [270]. Unfortunately this reference uses an other formula for the bandgap than used in [254] and my solution have been to simply use the correct formula for the bandgap, but still use the parameterizations in x&y of the reference. This could and should be improved by making a new fit to the original data.

Also, for values around and above the bandgap a finite broadening should be used to avoid a divergence [271, 276].

As mentioned in Sec. 5.1.1 the refractive index of the quantum wells and barriers is used as fitting parameter for the mode. However, for the initial design an estimate is needed. Calculating the index is quite complicated as the electronic structure is affected by the quantum confinement and consequently so is the refractive index [277, 278]. It is also evident that the high strain must have an impact on the refractive index and that the anisotropy in the electronic states must result is different refractive index for TE and TM polarization. I have chosen the simplest possible approximation, i.e. to use [270] but with the proper bandgap, including strain, and for the quantum well including quantum confinement. This has proven good enough for the design but present room for improvement.

Refractive index changes due to doping has been measured in [279] and calculated in [280] with good correspondence. For the index changes due to carrier injection [281] was used in the present work.

Free carrier absorption coefficients were taken from [178], i.e.

$$\alpha \cong \left(10^{-17} cm^3 \cdot N_D + 10^{-16} cm^3 \cdot N_A\right) dB/cm \tag{C.3}$$

which seem to fit reasonable well with measurements, but many other values exist in literature.

Appendix D

Abbreviations

3R regeneration	Reamplification, reshaping and retiming
ACPM	Asymmetric colliding pulse mode-locked
AR coating	Anti-reflection coating
ASE	Amplified spontaneous emission
BCB	Benzocyclobutene polymer
BER	Bit error rate
BHF	Buffered HF
CPM	Colliding pulse mode-locked
CR	Clock recovery
CW	Continuous wave
CY	Constant y (As/P ratio)
DBR	Distributed Bragg reflector
DCF	Dispersion compensating fiber
DFB	Distributed feedback laser
DOS	Density of state
DPSS	Diode-pumped solid state
EAM	Electroabsorption modulator
ECMLL	External cavity mode-locked laser
EDFA	Erbium doped fiber amplifier
ETDM	Electrical time division multiplexing
FROG	Frequency resolved optical gating
FSRM	Free space radiation mode method
FWHM	Full width at half maximum
HR coating	High-reflection coating
IV	Current vs. voltage characteristics
LI	Light (power) vs. current characteristics
LIFI	Lensed isolator fiber coupling package

LOC	Large optical cavity
MLL	Mode-locked laser
MMLL	Monolithic mode-locked laser
MOCVD	Metal-organic chemical vapor deposition
MOVPE	Metal-organic vapor phase epitaxy
NF	Noise figure
NRZ	Non-return to zero
OTDM	Optical time division multiplexing
P1dB	Power for 1 dB gain suppression
PL	Photoluminescence
PLL	Phase locked loop
PMT	Photomultiplier tube
PRBS	Pseudorandom bit sequence
Q(λ)	InGaAsP lattice-matched to InP with bandgap λ μm
QW, MQW	(Multiple) quantum well
RF	Radio frequency
RIE	Reactive ion etching
RIN	Relative intensity noise
RMS	Root mean square
RZ	Return to zero
SCH	Separate confinement heterostructure
SCOOP	Semiconductor components for optical signal processing
SCOOPx_y	Devices from batch "SCOOPx" with y QWs
SCPM	Self-colliding mode-locked lasers
SDH	Synchronous digital hierarchy
SHB	Spectral hole-burning
SHG	Second harmonic generation
SMF	Standard single mode fiber
SOA	Semiconductor optical amplifier
SPM	Self-phase modulation
SSB	Single side band
TBP	Time-bandwidth product
TE/TM	Transverse electric/magnetic (field)
TLA	Three letter abbreviation
TPA	Two photon absorption
TPS	Trailing pulse suppression
VCO	Voltage controlled oscillator
WDM	Wavelength division multiplexing
ZNS	Zero net strain